ENGINEERING HETERARCHY AND HIERARCHY IN METAL-ORGANIC FRAMEWORKS

A Dissertation

by

LIANG FENG

Submitted to the Office of Graduate and Professional Studies of
Texas A&M University
in partial fulfillment of the requirements for the degree of

DOCTOR OF PHILOSOPHY

Chair of Committee,	Hong-Cai (Joe) Zhou
Committee Members,	Sarbajit Banerjee
	David Powers
	Xiao-Feng Qian
Head of Department,	Simon North

August 2020

Major Subject: Chemistry

ABSTRACT

Complex natural systems usually have a hierarchical organization of multiple components at various scales. The well-defined hierarchical modules and their sequences in natural systems, such as brain networks, enable complicated functions and behaviors. These features have inspired me to engineer heterarchy and hierarchy in metal-organic frameworks (MOFs) for complicated applications involving cooperative behaviors.

Chapter I of this dissertation discusses the general concepts and motivations to design tailored MOF architectures with controllable hierarchy and heterogeneity. MOFs are a well-developed class of porous crystalline materials that are constructed from metal-ligand coordination bonds. The modular features of building blocks enable us to organize these units into well-organized porous framework materials.

Strategies to engineer heterarchy and hierarchy of MOFs are firstly introduced from a molecular level in Chapter II to IV. Chapter II of the dissertation describes the methods to introduce compositional heterogeneity into multicomponent MOFs through imprinted synthesis. In this chapter, controllable apportionment of functional groups inside MOFs can be obtained by utilizing flexible linker templates with tunable lengths. Chapter III of this dissertation further explores the effects of functional group apportionment on the formation of hierarchical pores inside MOFs *via* post-synthetic selective linker thermolysis. It was found that mixed-linker MOFs with a domain-based apportionment could be transformed into hierarchically porous MOFs upon selective thermolysis. To study dynamic behaviors inside hierarchically porous MOFs, Chapter IV

discusses strategies such as linker reinstallation to induce lattice expansion and contraction of a whole framework.

This is followed by Chapter V and VI, where chemistry at a mesoscopic level is explored in a series of multicomponent and hierarchical composites. Chapter V of the dissertation introduces the concept of retrosynthesis into the preparation of MOF-on-MOF structures with internal sequences. Chapter VI of the dissertation further extends the scope of modular synthesis, and emphasizes the power of modular programming in preparing MOF@polymer composites. In the last Chapter VII, a summary of current work and a trend description of future direction are provided, while my humble thoughts and outlooks on future smart MOF system are also presented.

DEDICATION

To my family and friends

For their love and support

ACKNOWLEDGEMENTS

I felt so fortunate to have opportunities to work with my research advisor and committee chair, Professor Hong-Cai (Joe) Zhou, on building multi-component frameworks with hierarchical structures. He allowed me to explore the porous materials world freely and inspired me to be an enthusiastic and humble scholar. I would like to express my sincere gratitude and deep appreciation to him for his guidance, support, encouragement, and enthusiasm in my four-year research. His research vision, attitude and view of science have equipped me with strong motivations and skills, which will benefit me perpetually. I also wish to express my appreciation to my committee members, Prof. Sarbajit Banerjee, Prof. David Powers and Prof. Xiao-Feng Qian for guiding and supporting me throughout my Ph.D. study.

I would like to thank all my colleagues who offer generous supports and helps that lead to the success of this dissertation. I feel so grateful to work with all Zhou group members, especially Kunyu Wang, Dr. Shuai Yuan, Gregory S. Day, Dr. Ying Wang, Tianhao Yan, Dr. Xiuliang Lv, Dr. Liangliang Zhang, Joshua Powell, Angelo Kirchon, Wenmiao Chen, Jeremy Willman and Elizabeth Joseph. In particular, I'd like to thank Kunyu for the productive collaboration and continuous discussions, who was always willing to offer his experimental helps and insights into project design. I'd like to thank Shuai to help me out in the first two years in the group, who shared his knowledge and experiences of MOF synthesis to me without reservation. Gregory also kindly read through my most papers and proposals, and provided many valuable suggestions and revisions.

I would also like to share my acknowledgment to my wonderful collaborators: Dr. Sheng-Han Lo, Prof. Chia-Her Lin, Dr. Kui Tan, Prof. Yves J. Chabal, Yutong Wang, Prof. Daofeng Sun, Dr. Zhehao Huang, Prof. Xiaodong Zou, Prof. Zhiyuan Gu, Prof. Tongbu Lu, Prof. Ya-Qian Lan, Prof. Linbing Sun, Prof. Sherzod T. Madrahimov, and Prof. Yu Han. I have learnt a lot from these experts with diverse backgrounds, and it was a wonderful experience to work with these collaborators.

I would like to acknowledge my mentors and collaborators during my undergraduate studies, including Prof. Hexiang Deng, Dr. Zhijie Chen, Prof. Mohamed Eddaoudi and Prof. Louis Bouchard. The systematic training from these experts benefits a lot and also helps me survive during graduate studies.

Finally, I want to thank my family and friends for their support, understanding, and love. It is their support that makes the journey of this dissertation colorful and unforgettable.

CONTRIBUTORS AND FUNDING SOURCES

Contributors

This work was supported by a dissertation committee consisting of Professor Hong-Cai Zhou, Professor Sarbajit Banerjee and Professor David Powers of the Department of Chemistry and Professor Xiao-Feng Qian of the Department of Materials Science and Engineering. The computational calculation of linker apportionment in Chapter II was conducted in part by Kunyu Wang and the crystallography in Chapter IV was conducted in part by Dr. Shuai Yuan from Zhou Research Group, Texas A&M University. All other work conducted for the dissertation was completed by the student independently.

Funding Sources

This work was made possible in part by Center for Gas Separations, an Energy Frontier Research Center (EFRC) funded by U.S. Department of Energy (DOE), Office of Science, Office of Basic Energy Sciences under award Number DE-SC0001015, by a Robert A. Welch Chair in Chemistry under award Number A-0030, and by the Qatar National Research Fund under Award Number NPRP9-377-1-080.

Its contents are solely the responsibility of the authors and do not necessarily represent the official views of the funding offices.

LIST OF ABBREVIATIONS

°C	Degrees Celsius
Å	Angstrom
BDC	Benzene-1,4-Dicarboxylic Acid
BET	Brunauer, Emmett and Teller
BPDC	Biphenyl dicarboxylic Acid
CCDC	Cambridge Crystallographic Data Centre
DEF	*N*,*N*-Diethylformamide
DFT	Density functional theory
DMF	*N*,*N*-Dimethylformamide
DMSO	Dimethyl Sulfoxide
DRIFTS	Diffuse Reflectance Infrared Fourier Transform Spectroscopy
EDX	Energy-Dispersive X-ray Spectroscopy
EtOH	Ethanol
FT-IR	Fourier Transform-Infrared Spectroscopy
GC	Gas Chromatography
HP	Hierarchically Porous
HRTEM	High Resolution Transmission Electron Microscopy
ICP-MS	Inductively Coupled Plasma-Mass Spectrometry
Im-CHO	2-Imidazolecarboxaldehyde
MeIm	Methylimidazole
MeOH	Methanol

MIL	Materials from Institut Lavoisier
MTV	Multivariate
MOF	Metal-Organic Framework
NMR	Nuclear Magnetic Resonance
PCN	Porous Coordination Network
PXRD	Powder X-Ray Diffraction
SCXRD	Single Crystal X-Ray Diffraction
TEM	Transmission Electron Microscopy
TFA	Trifluoroacetic Acid
TGA	Thermogravimetric Analysis
TPDC	p,p’-Terphenyldicarboxylic Acid
UiO	University of Oslo
UV-vis	Ultraviolet and Visible
XPS	X-ray Photoelectron Spectroscopy
ZIF	Zeolitic Imidazolate Framework

TABLE OF CONTENTS

LIST OF FIGURES

FIGURE Page

FIGURE Page

FIGURE Page

LIST OF TABLES

LIST OF SCHEMES

CHAPTER I

INTRODUCTION*

Materials science has witnessed the development and commercialization of several important classes of materials, including metal oxides, polymers, zeolites, silicons, carbons, and their composites.[1-5] These materials, mainly constructed from irreversible metallic, ionic, or covalent bonds, have been a tremendous boon, not only for the development of fundamental science, but also for the generation of new commercial and industrial products and processes. However, new and upcoming applications that focus on energy efficiency and low environmental impact require a shift in material design principles that focus on advanced tunability, precise functionality control, and synergism between structures and functionality. In particular, there is a growing interest in taking inspiration from biological systems for their ability to perform self-directed organization, replication, sorting, and correcting of both themselves and their substrates.

As a well-established class of porous materials, metal-organic frameworks (MOFs) have attracted great attention in the last two decades.[6-11] Their permanent pores, often in the nanometer scale, provide ideal spaces for molecular recognition, chemical storage, and the directed conversion of substrates. Additionally, their modular nature imparts designable topologies, adjustable porosities, tunable functionalities, and variable

---

* Reproduced with permission from: Feng, L.; Wang, K.-Y.; Gregory, D.; Zhou, H.-C. The Chemistry of Multi-component and Hierarchical Framework Compounds, *Chem. Soc. Rev.* **2019,** 48, 4823-4853. Copyright 2019 by The Royal Society of Chemistry.

surface moieties within a single material, which allows for a variety of potential applications in many areas, including gas storage, separation, and catalysis.[12-13] The quest for sophisticated functionalities in framework materials and their related composites typically requires hierarchical structures and specific sequences of multiple building units within the crystal.[14-15] In particular, MOFs have been targeted due to the

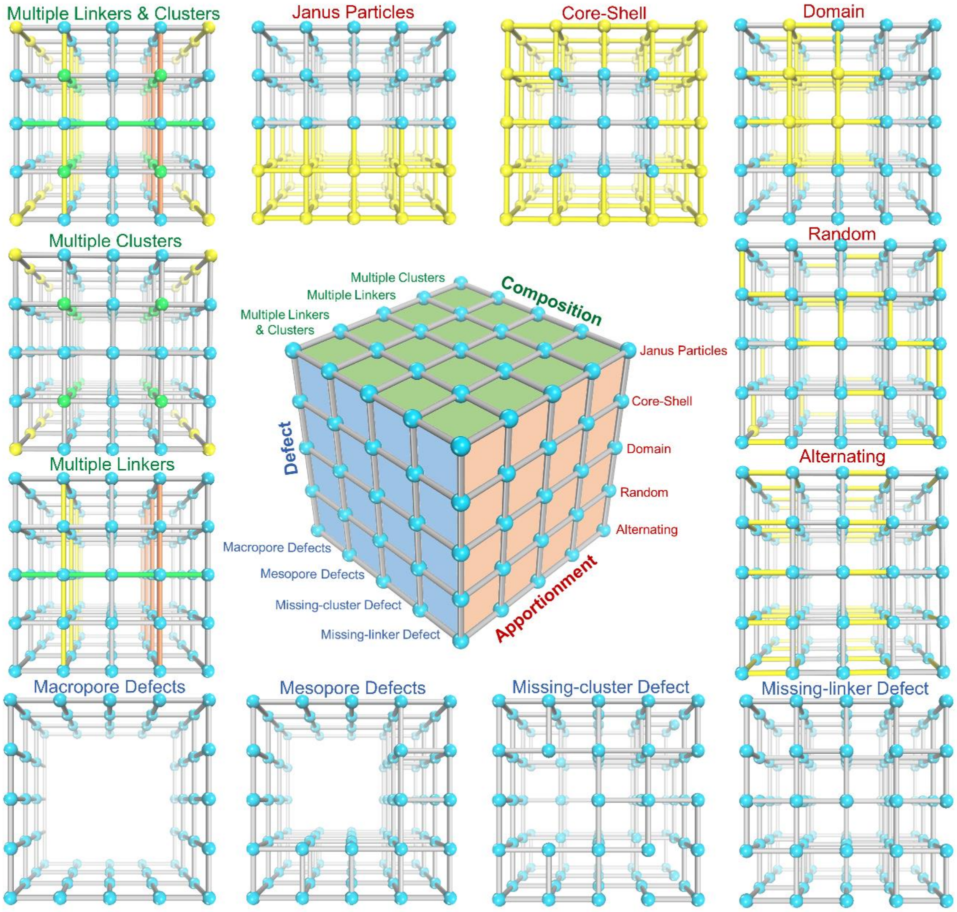

Scheme 1. Programmable pore environment in multi-component hierarchical metal-organic frameworks.

ease of introducing synergistic effects originating from the alignment and apportionment of specific functional groups in the proper proximity, something that is highly desired for areas such as cooperative catalysis. To expand upon these ideas, new synthetic methodologies geared towards precisely engineering heterarchy and hierarchy are urgently needed.

Heterarchy, also known as heterogeneity, requires the construction of complex structures with multiple organic and/or inorganic components.[16] The heterarchical features of porous framework materials allow them to operate in parallel on the molecular level due to the specific functionalities compartmentalized within their structures (Scheme 1). Usually, MOFs are prepared through the self-assembly of metal ions and organic ligands under solvothermal conditions in a "one-pot" reaction, and while this facile and effective method has led to the discovery of numerous framework materials, it possesses inherent limitations. The generation of complex frameworks with multiple ligands or metals in a one pot reaction remains difficult as these structures tend to be less symmetric and therefore stable, with many multicomponent "one-pot" syntheses resulting in a mixture of MOF products. At that same time, multi-component framework materials show promise for advanced applications, particularly in catalysis, where having multiple functional groups in close proximity can result in alteration of products or product ratios. In addition, the "one-pot" method is less effective for the preparation of stable frameworks with inert metal–ligand bonds.[6] This gap between framework design and synthesis has become a critical limitation: with the "one-pot" solvothermal reaction process essentially being a black box, necessitating new means of rationally designing and building new heterarchical frameworks.

Hierarchy refers to the incorporation of multi-level or multi-domain organizations within a system. Hierarchy is well-known within biological systems and is of particular interest for artificial materials.[17] Tuning the hierarchical structure of a material for targeted binding behaviors involves not only optimizing the environment of the binding center, but also improving the selectivity of the porous framework as a whole.[4] This is chiefly done via tuning the order, sequence, and interactivity within the hierarchical network. For example, catalytic activity is primarily focused on the geometry and electronics of the active metal centers, typically using the design philosophies found within homogeneous catalyst design. However, while incorporation of catalytically active moieties within MOFs can allow for improved geometric control, it does also introduce problems associated with the slow diffusion of large reactants into the micropores of the structure. Furthermore, when a microporous framework is used to immobilize bulky catalysts, the active-site accessibility and catalytic activity will plummet due to pore blockage. As such, the incorporation of hierarchical, or multi-scale size, porosity is expected to allow for the well-organized transport of substrates within the pore structures.[18]

With increased attention on expanding the diversity and properties of porous materials, there has been an extensive increase in the study of pore engineering strategies, controlling the compositions, defects, and apportionment within the porous structures.[18] The simplest and most efficient method to control these pore structures is through enriching the diversity of metal and linker compositions available for the structures. Linkers with various functional groups, with their tunable steric and electronic effects, can be incorporated into the pore walls. Meanwhile metal ions with varying redox activity and Lewis acidity are also able to be integrated at the metal nodes adjacent to the functionalized linkers, allowing for the simple incorporation of tandem methodologies. As such, controlling the arrangement of these structures becomes an important concern for improving their overall performance. Theoretically, when multiple linkers or clusters are incorporated into one framework backbone, they are expected to exhibit one of five common classes of distribution: alternating, random, domain, core-shell, or Janus-particle types. Among these five classes, core-shell and Janus-particle types are usually considered as hierarchical structures due to their macroscopic multi-level arrangement. Additionally, defects are another important component for framework materials. Missing-linker or missing-cluster defects can also lead to the colossal changes in adsorption or catalytic properties. When there are mesoporous or macroporous defects created inside a traditional microporous material, the resulting material is dubbed a hierarchically porous materials, as the defects result in secondary domains of pores that can affect diffusion and transportation. The apportionment of these multi-level defects dispersed inside the frameworks is also vital for enhancing our understanding on the fundamentals of molecular diffusion within these framework materials.

CHAPTER II

CONTROLLING COMPOSITION HETEROGENEITY IN MULTICOMPONENT MOFS*

2.1 Introduction

The well-defined sequences and apportionment of multiple building units in biomolecules have inspired researchers to develop tailored architectures with controllable heterogeneity in polymers, nanomaterials and porous materials.[5, 19-22] For example, multi-component MOFs have recently gained increasing attention due to their enhanced sorption and separation behaviors, efficient cooperative catalytic activities and programmable luminescence or guest delivery behaviors.[8, 11, 14-15, 23-27] For multi-component MOFs with linkers taking different crystallographic positions, functional groups can be precisely placed into predetermined positions (Scheme 2a).[28-31] Although the positions and arrangements of functional groups are fixed and ordered in this case, placement of linkers in fixed positions presents a lack of tunability over linker distances, interactions, apportionments and thus overall properties. Another set of mixed-linker MOFs, known as multivariate (MTV) MOFs, contains multiple types of linkers at identical crystallographic positions. MTV-MOF-5 and MTV-UiO-66 are representative MTV-MOFs synthesized using a one-pot approach (Scheme 2b).[32-33] In this case, the

---

[*] This chapter is reproduced with permission from Feng, L.; Wang, K.; Lv, X.-L; Powell, J.; Yan, T.; Willman, J.; Zhou, H.-C., Imprinted Apportionment of Functional Groups in Multivariate Metal–Organic Frameworks, *J. Am. Chem. Soc.* **2019,** 141, 37, 14524-14529, Copyright 2019 by American Chemical Society.

apportionment of the newly introduced functionalities is usually determined by characterization after synthesis, while *ab initio* construction of MTV-MOFs with predictable arrangement is almost impossible to achieve during the "black-box" synthesis.[23] In addition, post-synthetic linker exchange can alter the apportionment modes depending on the diffusion and exchange kinetics.[34-35] However, the mechanism of linker exchange and the influence of ligand sterics on the apportionment are far from fully understood. Therefore, novel strategies to regulate apportionment of functional

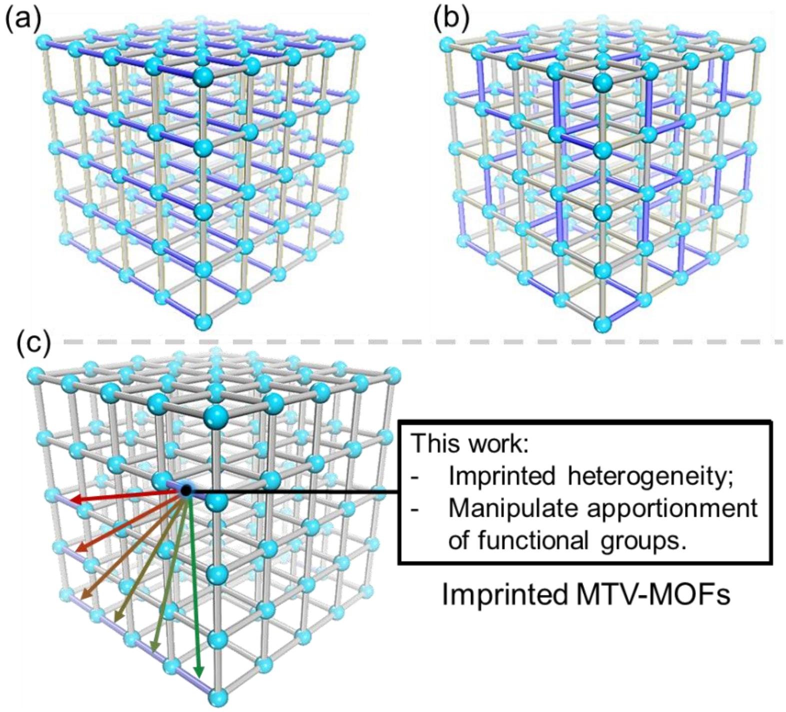

Scheme 2. **Types of mixed-linker MOFs**: (a) MOFs with mixed-linkers taking different crystallographic positions; (b) MTV-MOFs with multiple linkers taking identical crystallographic positions; (c) Imprinted MTV-MOFs should enable control over linker sequence and apportionment within one framework.

groups in MTV-MOFs are an urgent need and will create new and unexpected opportunities for data recognition, replication, storage and delivery.

One possible solution is to synthesize MTV-MOFs *ab initio* with enhanced interactions between various functional groups.[36-38] For instance, cleavable covalent links between the functional groups on linkers can be judiciously introduced during a pre-synthetic step, and maintain this pre-interlocked sequence during the incorporation step. Subsequent cleavage of interlocking groups in the resultant heterogeneity-controlled imprinted MTV-MOFs will produce an MTV-MOF with precisely apportioned functional groups (Scheme 2c). Herein, we introduce a novel strategy to regulate apportionment of functional groups in MTV-MOFs by forming a pre-interlocked template (Scheme 3). Initially, a pre-interlocked linker with cleavable links is incorporated inside the MTV-MOF under mild post-synthetic conditions. The control of apportionment and sequence is directed and ensured by the fixed covalent links within frameworks. These labile linkages between functionalized linkers are then selectively cleaved in the framework through hydrolysis, leading to the exposure of functional groups at correlated positions. Eventually, controlled heterogeneity in MTV-MOFs can be easily achieved by regulating apportionment of functionalities.

2.2 Experimental Section

Materials and Instrumentation

All the reagents and solvents were commercially available and used as received. Powder X-ray diffraction (PXRD) was carried out with a Bruker D8-Focus Bragg-

Brentano X-ray Powder Diffractometer equipped with a Cu sealed tube (λ = 1.54178 Å) at 40 kV and 40 mA. Nuclear magnetic resonance (NMR) data were collected on an Inova 500 spectrometer. Inductively Coupled Plasma-Mass Spectrometry (ICP-MS) data were collected with a Perkin Elmer NexION® 300D ICP-MS. For thermogravimetric analysis (TGA), about 10 mg of the sample was heated on a TGA-50 (SHIMADZU) thermogravimetric analyzer from room temperature to 600 °C at a rate of 5 $°C \cdot min^{-1}$ under O_2 flow of 15 $mL \cdot min^{-1}$. Diffuse reflectance infrared Fourier transform spectroscopy (DRIFTS) measurements were performed on a SHIMADZU IR Affinity-1 spectrometer equipped with DRS-8000A drift diffuse reflectance attachment. Gas sorption measurements were conducted using a Micromeritics ASAP 2020 system. Prior to gas sorption measurements, about 50 mg MOF materials were washed thoroughly with N,N-dimethylformamide (DMF) to remove any remaining solvent or uncoordinated linker, and exchanged by methanol for 3 times. The solvent was then removed under vacuum at 85 ^{o}C for 12 h, yielding porous material.

Ligand Synthesis

Synthesis of L2. 2-imidazolecarboxaldehyde (1.92 g, 20 mmol), ethylenediamine (C2, 0.60 g, 10 mmol) and 50 mL ethanol were mixed in a 250 mL flask and refluxed for 12 h under continuous stirring. After cooling to room temperature, the precipitates were collected by filtration and washed with cold ethanol (2.31 g, yield: 92%). ^{1}H-NMR (500 MHz, dimethyl sulfoxide-d_6/DMSO-d_6) δ 12.68 (s, 2H), 8.16 (s, 2H), 7.17 (s, 2H), 7.03 (s, 2H), 3.87 (s, 4H).

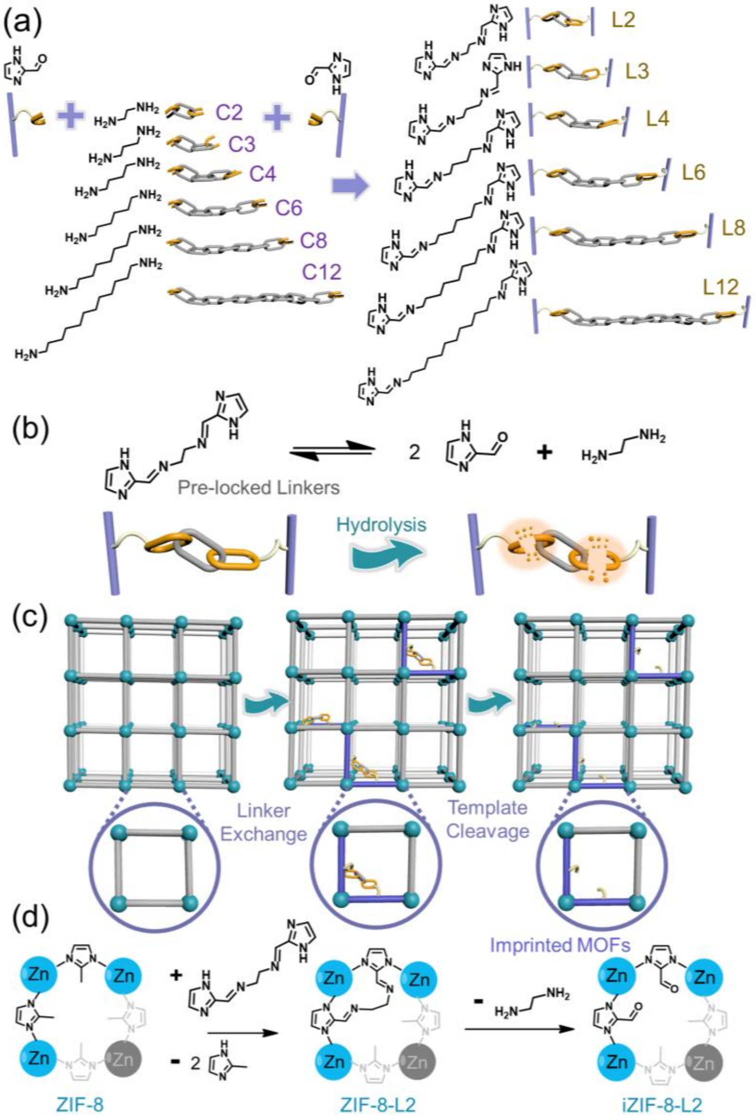

Scheme 3. Controlled heterogeneity in MTV-MOFs: (a) The synthesis of pre-locked linkers (LX, X = 2, 3, 4, 6, 8 and 12). (b) The dissociation and association of imine bonds in pre-locked linker (L2); (c, d) Illustration of the sequential linker exchange and dissociation processes.

Synthesis of L3. 2-imidazolecarboxaldehyde (1.92 g, 20 mmol), 1,3-

diaminopropane (C3, 0.74 g, 10 mmol) and 50 mL ethanol were mixed in a 250 mL flask and refluxed for 12 h under continuous stirring. After cooling to room temperature, the precipitates were collected by filtration and washed with cold ethanol (2.52 g, yield: 95%). ^{1}H-NMR (500 MHz, DMSO-d_6) δ 12.67 (s, 2H), 8.18 (s, 2H), 7.19 (s, 2H), 7.05 (s, 2H), 3.65 (m, 4H), 1.96 (m, 2H).

Synthesis of L4. 2-imidazolecarboxaldehyde (1.92 g, 20 mmol), 1,4-diaminobutane (C4, 0.88 g, 10 mmol) and 50 mL ethanol were mixed in a 250 mL flask and refluxed for 12 h under continuous stirring. After cooling to room temperature, the precipitates were collected by filtration and washed with cold ethanol (2.46 g, yield: 89%). ^{1}H-NMR (500 MHz, DMSO-d_6) δ 12.63 (s, 2H), 8.17 (s, 2H), 7.18 (s, 2H), 7.04 (s, 2H), 3.59 (m, 4H), 1.68 (m, 4H).

Synthesis of L6. 2-imidazolecarboxaldehyde (1.92 g, 20 mmol), 1,6-diaminohexane (C6, 1.16 g, 10 mmol) and 50 mL ethanol were mixed in a 250 mL flask and refluxed for 12 h under continuous stirring. After cooling to room temperature, the precipitates were collected by filtration and washed with cold ethanol (2.71 g, yield: 88%). ^{1}H-NMR (**Figure 1,** 500 MHz, DMSO-d_6) δ 12.65 (s, 2H), 8.14 (s, 2H), 7.18 (s, 2H), 7.04 (s, 2H), 3.55 (m, 4H), 1.61 (m, 4H), 1.34 (m, 4H).

Synthesis of L8. 2-imidazolecarboxaldehyde (1.92 g, 20 mmol), 1,8-diaminooctane (C8, 1.44 g, 10 mmol) and 50 mL ethanol were mixed in a 250 mL flask and refluxed for 12 h under continuous stirring. After cooling to room temperature, the precipitates were collected by filtration and washed with cold ethanol (2.96 g, yield: 88%). ^{1}H-NMR (500 MHz, DMSO-d_6) δ 12.64 (s, 2H), 8.13 (s, 2H), 7.17 (s, 2H), 7.03

(s, 2H), 3.52 (m, 4H), 1.59 (m, 4H), 1.29 (m, 8H).

Synthesis of L12. 2-imidazolecarboxaldehyde (1.92 g, 20 mmol), 1,12-diaminododecane (C12, 2.00 g, 10 mmol) and 50 mL ethanol were mixed in a 250 mL flask and refluxed for 12 h under continuous stirring. After cooling to room temperature, the precipitates were collected by filtration and washed with cold ethanol (3.53 g, yield: 90%). ^{1}H-NMR (500 MHz, DMSO-d_6) δ 12.65 (s, 2H), 8.13 (s, 2H), 7.17 (s, 2H), 7.03 (s, 2H), 3.53 (m, 4H), 1.58 (m, 4H), 1.24 (m, 16H).

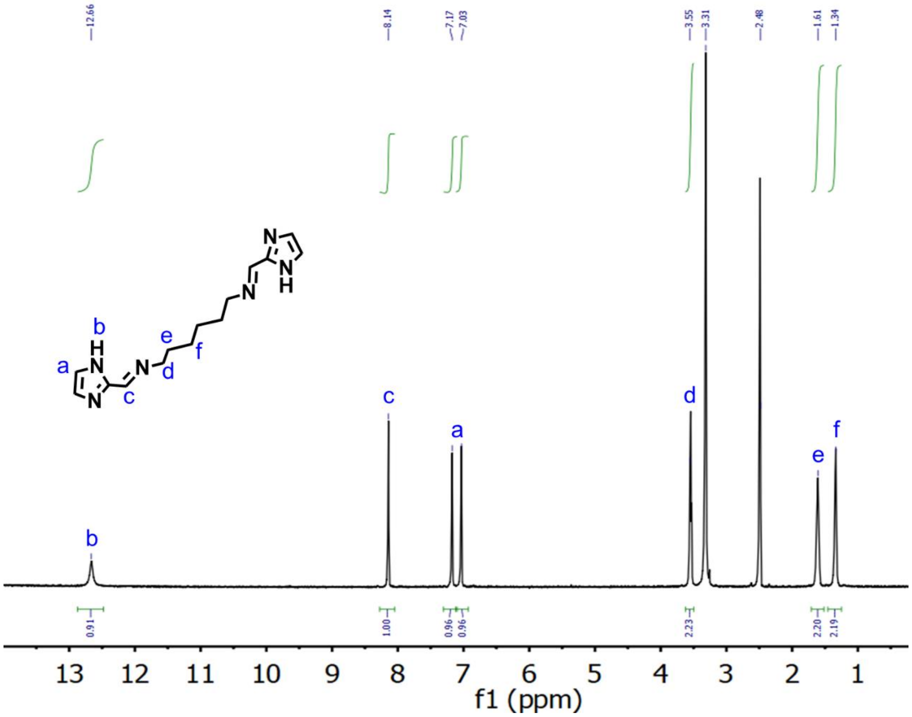

Figure 1. ^{1}H NMR spectroscopy of L6.

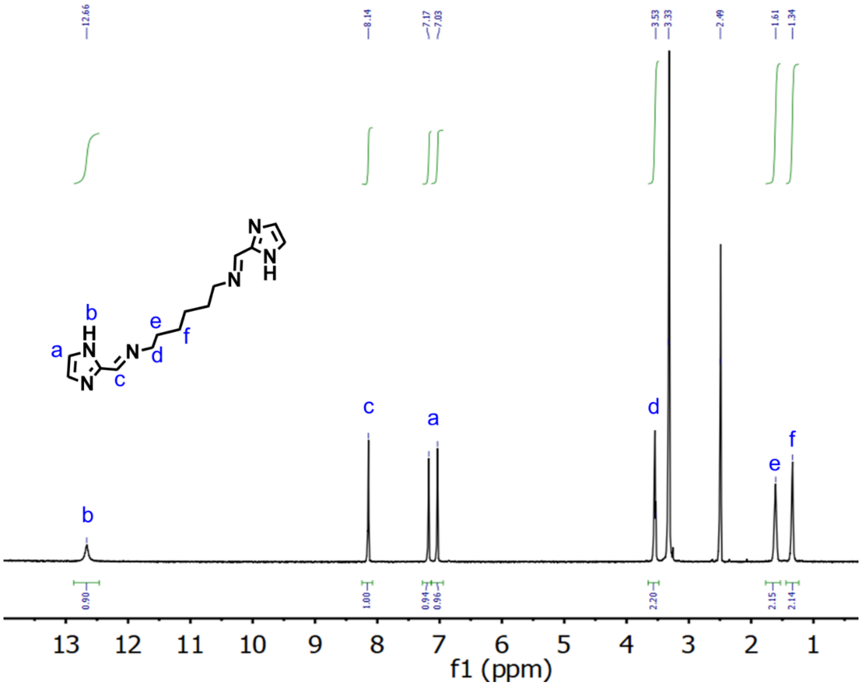

Figure 2. ^{1}H NMR spectroscopy of L6 in DMSO for 24 h.

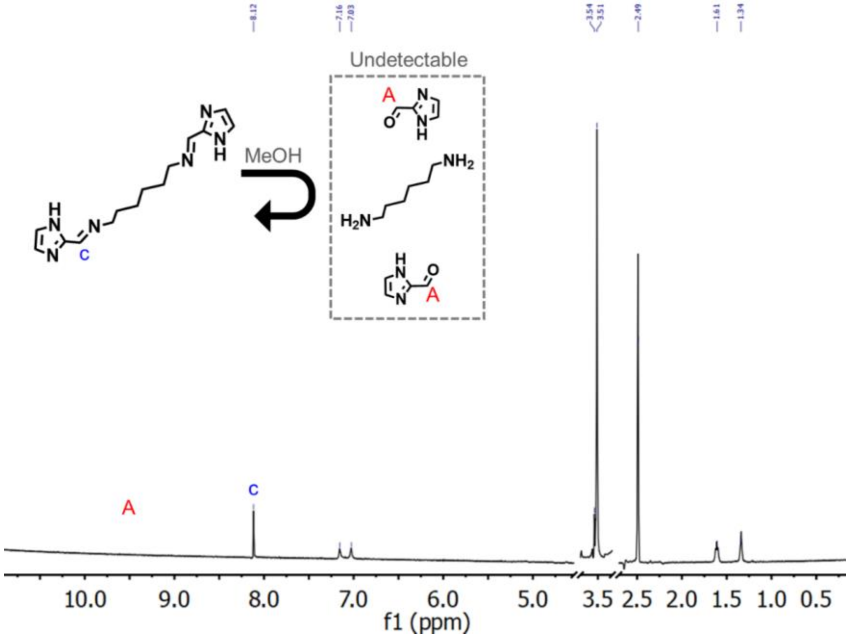

Figure 3. ^{1}H NMR spectroscopy (DMSO-d_6) of L6 in MeOH at 65 °C for 24 h.

MOF Synthesis

Synthesis of ZIF-8 microcrystals. Zeolitic imidazolate framework-8 (ZIF-8) microcrystals were synthesized according to the literature with slight modification.[39] $Zn(NO_3)_2{\cdot}4H_2O$ (0.210 g) and 2-methylimidazole (2-MeIm) (0.060 g) were dissolved in 18 mL DMF in a 20-mL vial. The vial was then capped and placed in a 140°C oven for 24 h to yield colorless polyhedral crystals. The crystals were then washed with fresh DMF three times.

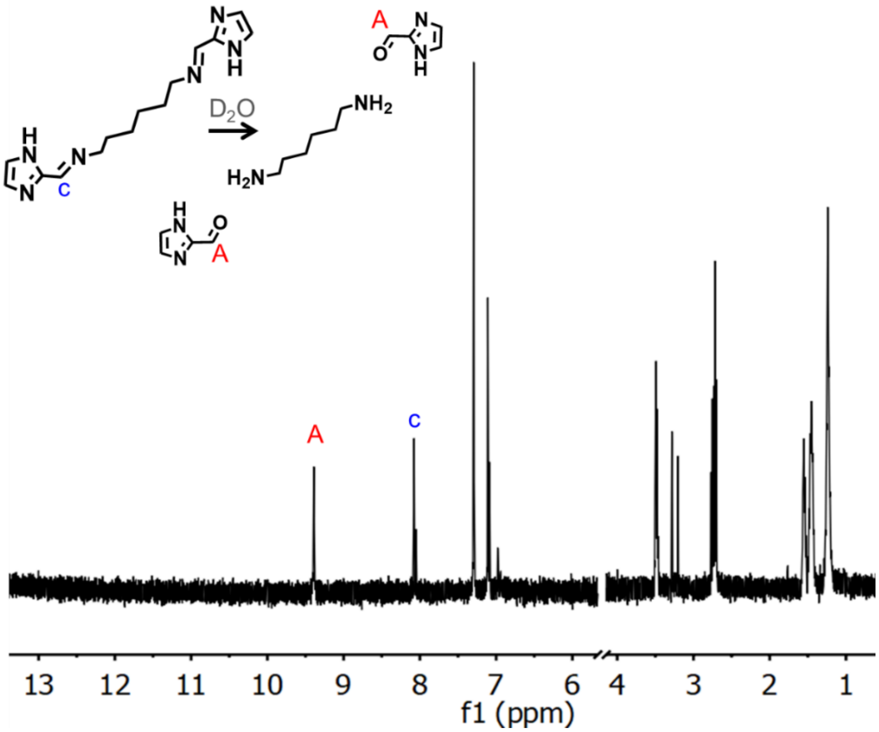

Figure 4. ^{1}H NMR spectroscopy of L6 in D_2O at 25°C for 24 h.

Synthesis of mixed-linker ZIF-8 with pre-locked linkers through linker

exchange. The procedure of linker exchange in ZIF-8 was conducted according to the literature with slight modification.[40] ZIF-8-LX-R% (X = 2, 3, 4, 6, 8 and 12) were synthesized by the linker exchange of ZIF-8 with pre-locked linker (L2, L3, L4, L6, L8 and L12) solution of various concentrations (15 and 30 mM, respectively). Generally, crystals of ZIF-8 (100 mg) were incubated with the linker L solution in methanol (MeOH, 20 mL) at 60 ºC for 4 - 288 h. The crystals of ZIF-8-LX-R% were collected by filtration and washed with fresh MeOH for 3 times. The exchange ratio in MOFs (R%) was calculated from ^{1}H-NMR results of digested samples. For ^{1}H NMR spectroscopy, the dry samples (around 5 mg) were dissolved in about 1 mL 5% DCl/DMSO-d_6. The pre-locked linker (LX) was decomposed into Im-CHO (2-imidazolecarboxaldehyde) and diamines after hydrolysis. Therefore, the exchange ratio can be calculated by the integration of H from 2-MeIm and Im-CHO.

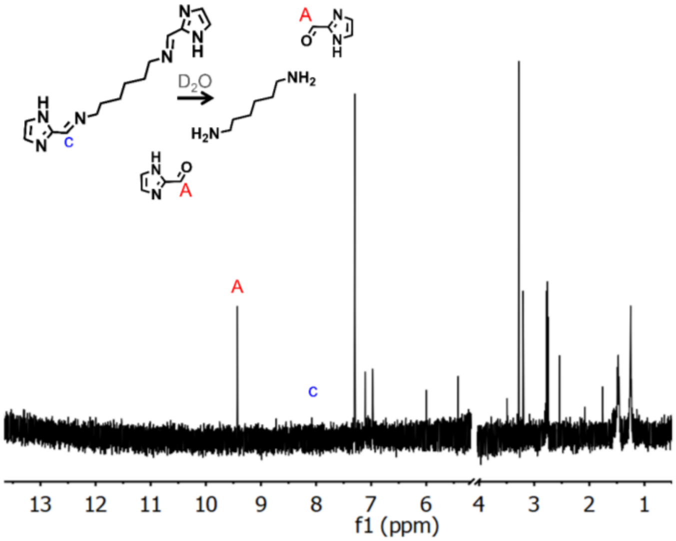

Figure 5. ^{1}H NMR spectroscopy of L6 in D_2O at 50ºC for 24 h.

Linker dissociation analysis. We proposed that labile imine bonds in pre-locked linker (LX) are dissociated and removed during water treatment to create exposed aldehyde groups (Figure 4-8). The stability of imine bonds in various solvent conditions was verified by ^{1}H NMR.

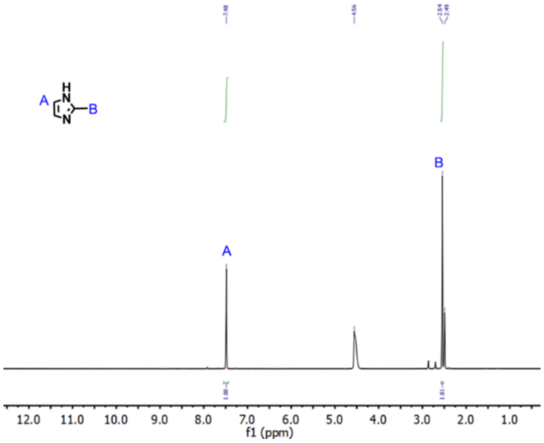

Figure 6. ^{1}H NMR spectroscopy of digested ZIF-8.

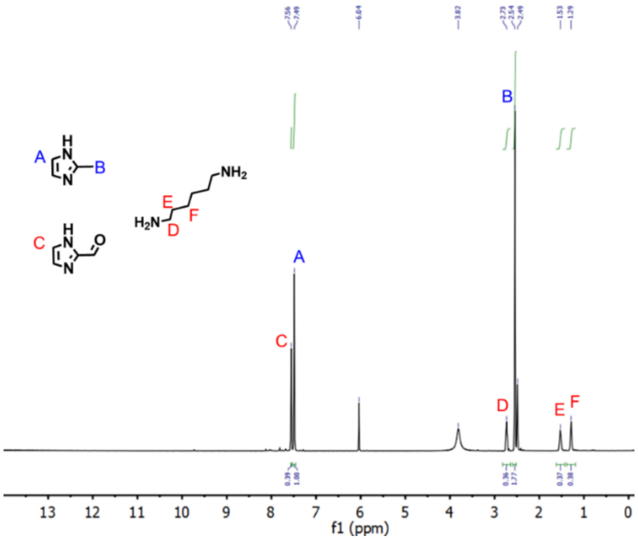

Figure 7. ^{1}H NMR spectroscopy of digested ZIF-8-L6-26%.

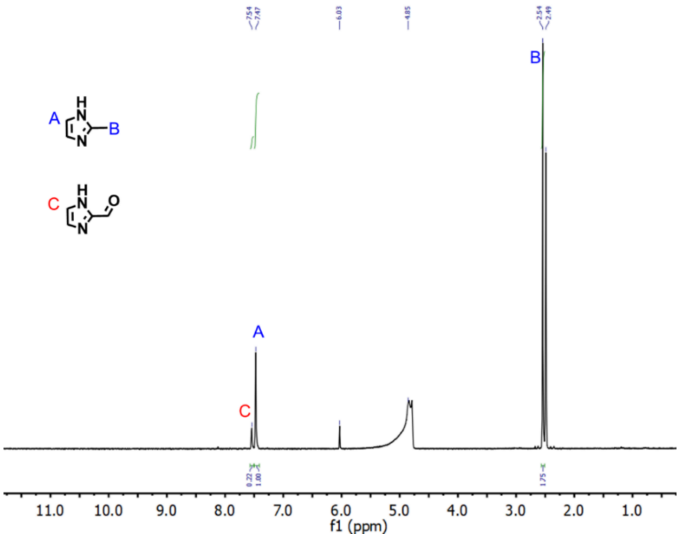

Figure 8. ^{1}H NMR spectroscopy of digested iZIF-8-L6-18%.

Calculation Methods

The DFT calculation was performed by DMol^3 program. To describe approximation of exchange-correction energy, gradient-corrected functional developed by Perdew *et al* (GGA-PBE) was chosen for geometry optimization.[41] The weak van der Waals interaction was considered by introduction of semi-empirical Grimme dispersion correction method.[42] Besides, double numerical plus polarization basis set in version 4.4 (DNP 4.4) was applied and all core electrons of atoms were taken into consideration.[43] The convergence tolerance of total energy, maximum force, and displacement were set as 2×10^{-5} Ha, 0.004 Ha Å^{-1}, and 0.005 Å. Due to the complexity and high number of atoms in the ZIF lattice, only a limited number of atoms were considered to simplify the calculations. To simulate constraint of framework, nitrogen atoms of terminal imidazoles and zinc atoms are fixed.

2.3 Results and Discussion

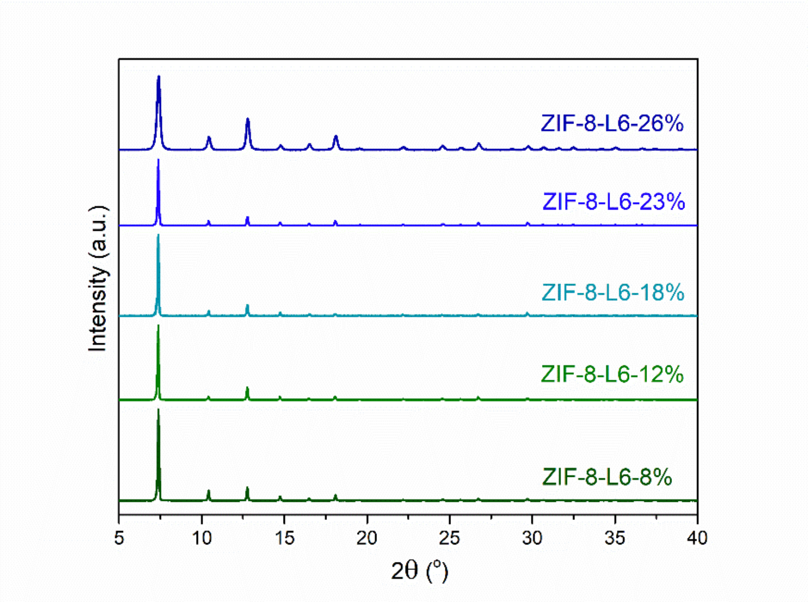

Figure 9. PXRD patterns of ZIF-8-L6-R%.

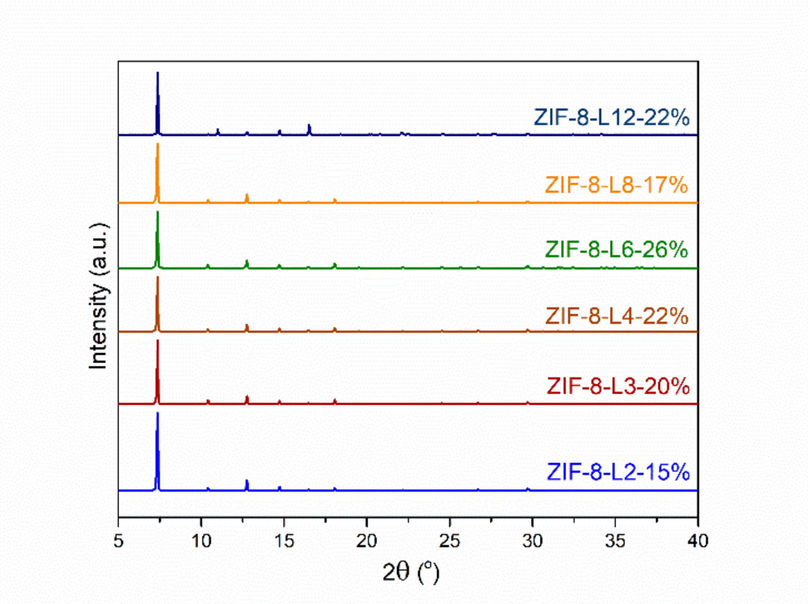

Figure 10. PXRD patterns of ZIF-8-LX-R%.

One of the most studied MOFs, ZIF-8, was introduced as a model to demonstrate our strategy because of its excellent stability and strong tolerance towards post-synthetic modification.[40, 44-45] An aldehyde-based linker, denoted as Im-CHO, was chosen as a prototype to study the controlled heterogeneity within the framework while 2-MeIm is main matrix for dispersion. In order to form a pre-locked linker template (LX, X = 2, 3, 4, 6, 8 and 12), Im-CHO was firstly linked to diamines (CX, X = 2, 3, 4, 6, 8 and 12), to form a pre-labile linker, which can easily dissociate into the corresponding monomers in a single step through hydrolysis (Scheme 3).[46-47] Post-synthetic linker exchange at a mild condition (LX/MeOH solutions at 60 °C) was adopted (Figure 2-3), which shall maintain the integrity of the imine bonds in pre-locked linker templates (LX).[48] Relatively low concentration solutions of LX (15-30 mM) were utilized to minimize the possibility of a "dangling" exchange mode (Figure 11). After exchange, the crystals underwent a color change from white to light yellow as indicated by the optical images. The preservation of the imine bonds after soaking in MeOH at 60°C for 24 h was verified by ^{1}H NMR spectroscopy (Figure 3). ^{1}H NMR spectroscopy of digested samples also demonstrated that both imidazoles of LX successfully replaced the original 2-MeIm linkers, verifying that the exchange of LX happens in a locking/bridging mode. The exchanged ZIF-8 was denoted as ZIF-8-LX-R%, where the exchange ratio (R%) was defined as moles of imidazole from pre-locked linkers (LX) divided by the moles of total imidazole in exchanged ZIF-8. It was found that the exchange ratio R% of ZIF-8-L6-R% gradually increased as incubation time increased and leveled off after 300 min. Further elongation of incubation time did not increase the L6 content, indicating that a dynamic equilibrium is reached between the solid and the solution. The exchange ratios of ZIF-8-L6 vary from 18% to 26%, when incubated with different concentrations of L6/MeOH solutions

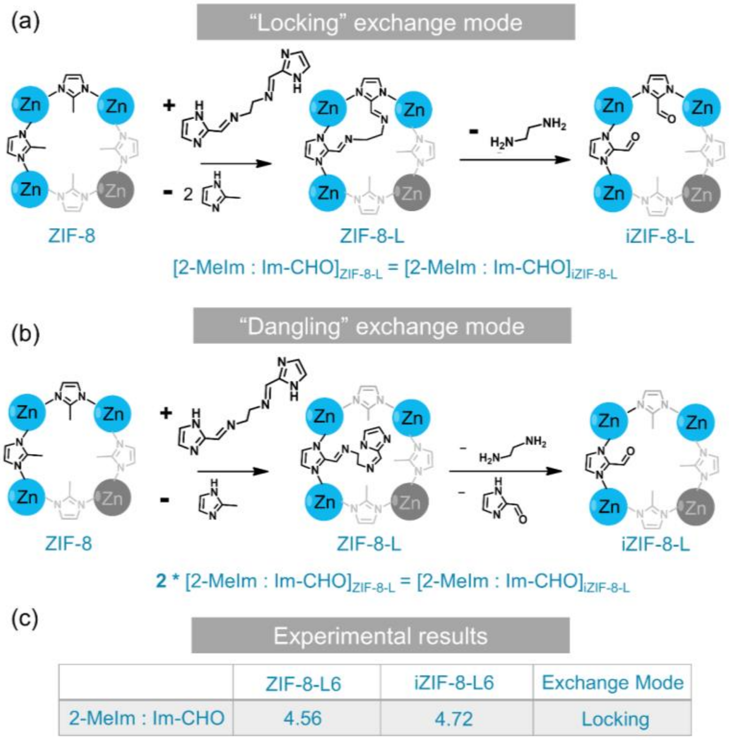

	ZIF-8-L6	iZIF-8-L6	Exchange Mode
2-MeIm : Im-CHO	4.56	4.72	Locking

Figure 11. Studies on exchange modes of template linkers LX. (a) If the exchange of template LX happens in a locking mode, the ratio between 2-MeIm and Im-CHO will remain even after the hydrolysis of LX; (b) If the exchange of template LX happens in a dangling mode, the ratio between 2-MeIm and Im-CHO will double after the hydrolysis of LX since the dangling imidazole linkers will be removed; (c) Experimental results of digested ZIF-8-L6-18% and iZIF-8-L6-18% shown the locking mode happens mainly during the given exchange condition.

(15 and 30 mM, respectively) for 10 h. The supernatants after linker exchange were analyzed by ICP-MS, which showed no detectable Zn^{2+}. ZIF-8-LX-R% samples also maintain crystallinity as revealed by the PXRD patterns (Figure 9-10) and the microscope images of the respective crystals. The N_2 adsorption isotherms of ZIF-8-L6-R% after post-synthetic linker exchange showed a clear decrease of N_2 total uptake compared with as-synthesized ZIF-8, corresponding to the cavity being filled by the newly-introduced bulky linkers with removable diamine linkages. Additionally, the BET (Brunauer, Emmett and Teller) surface areas of ZIF-8 decreased after exchange because of the partially occupied pore spaces.

The successful incorporation of pre-locked linkers in MTV-ZIF-8 can also be confirmed by comparing the DRIFTS of ZIF-8 and ZIF-8-LX-R%. The appearance of imine bonds in ZIF-8-LX-R% is confirmed by the associated peaks [ν(C=N) at ~1651 cm^{-1}]. The composition of exchanged ZIF-8 was further analyzed by TGA (Figure 14). The initial weight loss before 200 °C is attributed to the removal of the solvent molecules in the pores whereas the removal of organic linkers corresponds to the weight loss from 200 to 500 °C. Notably, ZIF-8-L6-26% shows much higher weight loss than ZIF-8 without post-synthetic treatment between 200 to 500 °C, due to the removal of the pre-locked linkages inside frameworks. These results show that the exchange ratio of ZIF-8 can be tuned with retention of framework integrity and porosity, which ensures the imprinted apportionment of functional groups in MTV-MOFs. Solid-state NMR spectroscopy of exchanged ZIFs indicates the complete deprotonation of templated linkers, which rules out the dangling possibility during the exchange process (Figure 12-13).

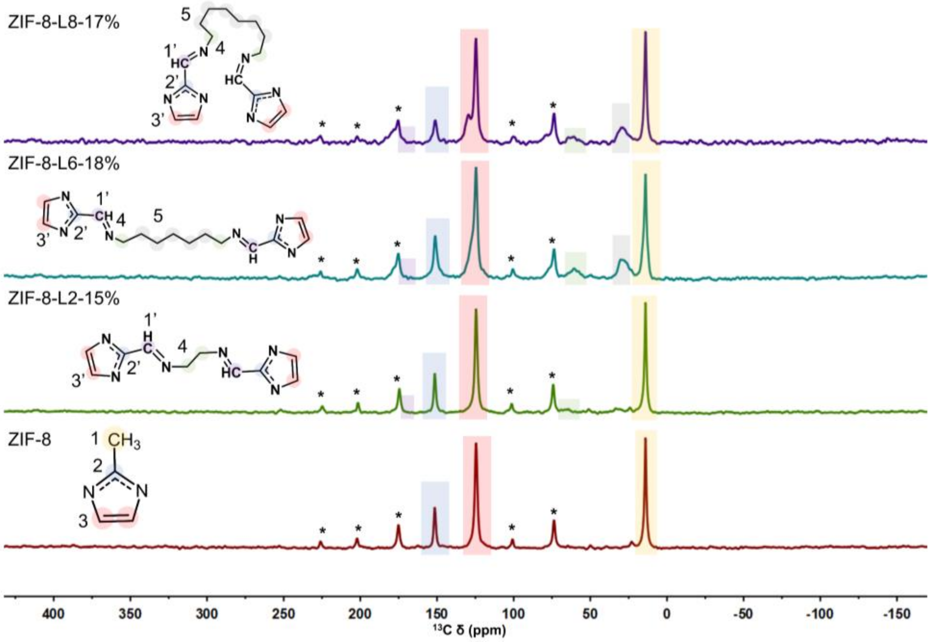

Figure 12. ^{13}C CP-MAS NMR spectra of various functionalized ZIFs. Spinning sidebands are indicated by *.

When exposed to aqueous solution, the pre-locked linkers (LX) in the framework were expected to dissociate into 2-methylimidazole and diamines (CX) through hydrolysis. When performed at room temperature for 24 h, the reaction between L6 and water does not go to completion (Figure 4). However, when the hydrolysis is performed at 50 °C, nearly quantitative cleavage of the imine bonds was observed, generating exposed aldehyde functional groups and released diamines (Figure 5). The cleaved diamines can be easily removed from the framework with sufficient washing, while the exposed functional groups (-CHO) are apportioned in a controlled fashion and manipulated by the tunable pre-locked chains. The resulting imprinted MTV-MOFs were donated as iZIF-8-LX-R%, where i stands for “imprinted”. Note that the coordination bonds between Zn nodes and imidazole linkers are robust enough to survive from the mild water treatment.[6]

ZIF-8 samples with various exchange ratios were prepared and treated with aqueous solution at 50 °C for 24 h. PXRD patterns of the resulting iZIF-8-LX-R% showed that the MOF materials after hydrolysis possessed the same diffraction patterns as the parent ZIF-8. The microscope images of the respective crystals demonstrated that the crystal morphology was not affected by the template cleavage process. The porosity of iZIF-8-LX-R% was also studied by N_2 sorption measurements, which confirm an increase in pore size due to the release of template molecules. Compared to ZIF-8-LX-R%, the N_2 sorption isotherms of microporous iZIF-8-LX-R% at 77 K demonstrated increased uptakes with a type-I isotherm, indicating the release of template molecules from the framework. No notable mesopores were observed in the N_2 sorption isotherms, ruling out the possibility of partial decomposition of ZIF-8 during post-synthetic treatment. The subsequent cleavage of pre-locked linkers significantly changed the pore volume and corresponding environment.

To examine whether the imine bonds were successfully dissociated during the hydrolysis treatment, DRIFTS absorption spectroscopy was utilized to confirm the linker dissociation process. A clear blue shift of the stretching bands of the imine group [ν(C=N), ~1651 cm^{-1}] to aldehyde group [ν(C=O), ~1683 cm^{-1}] was observed. Besides, there are also appearance of peaks around 2768 cm^{-1} and 2733 cm^{-1}, associated with ν(C-H, aldehyde) and δ(C-H, aldehyde) modes, respectively, which indicates successful cleavage of the imine bond. In addition, the composition of iZIF-8 was further analyzed by TGA and compared with ^{1}H NMR results (Figure 14). The weight losses corresponding to the thermal decomposition of organic fragments match well with the calculation.

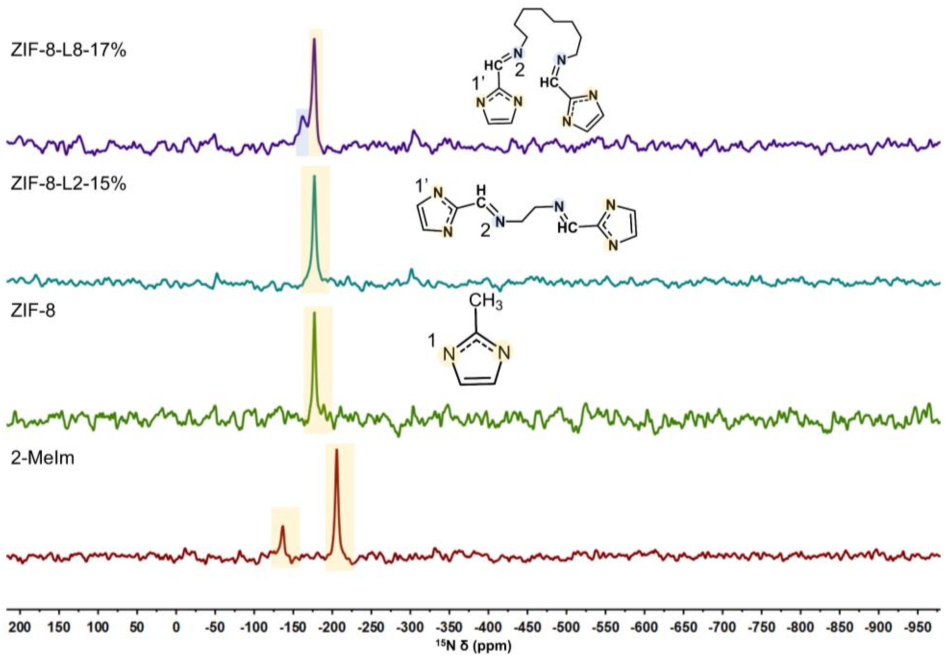

Figure 13. ^{15}N CP-MAS NMR spectra of linkers and ZIFs. Spinning sidebands are indicated by *.

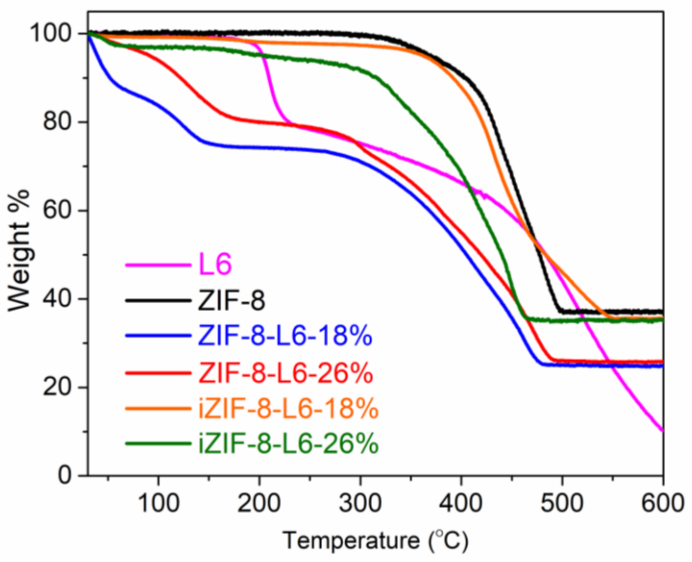

Figure 14. TGA of pre-locked linker L6, ZIF-8, ZIF-8-L6-18%, ZIF-8-L6-26%, iZIF-8-L6-18%, and iZIF-8-L6-26%.

Table 1. Summary of energy changes (unit: kcal/mol) after the exchange of 2-methylimidazole pairs with a chain template (LX, X = 2, 3, 4, 6, 8 and 12).

	I	**II**	**III**	**IV**	**V**	**VI**	**VII**	**VIII**	**IX**
2	26.05	12.32	30.47						
3	24.98	8.13	37.72	13.08					
4	30.90	10.53	24.29	9.51		15.55			
6	41.02	7.23	33.25	−1.94	25.93	24.84			
8	38.66	5.57	27.59	−1.99	1.44	22.13	−14.04	−11.13	9.20
12	33.87	6.94	9.66	−9.07		−20.43	−12.64	−17.92	-12.85

We further extended the strategy to other diamines with various chain lengths to investigate the versatility of regulated apportionment of pre-locked linkers. Six pre-locked linkers were introduced with variable lengths to regulate the distribution of functional groups in the ordered frameworks. The successful sequential linker exchange and dissociation were achieved in these systems with well-maintained crystallinity, as indicated by optical images, N_2 sorption isotherms, and PXRD patterns. To gain insights into the controlled linker apportionment in iZIF-8-LX-R%, we inspected the possible models of linker apportionment to study the distances and distributions of ZIF frameworks. We found that spatial distributions of pre-locked linker templates (LX) could be influenced by the distance and orientation of imidazole ligands in original frameworks. The ZIF cage was modelled as a truncated octahedron, with the zinc nodes represented by the vertices and the ligands represented by the edges of the polyhedron (Figure 15). Faces of the polyhedron are comprised of squares and hexagons. For conciseness, the spatial relationship between ligands can be displayed through a projection on the polyhedron. The orientations of two imidazole ligands can be described as one of four different patterns: opposite, inverse, parallel, and anti-parallel. According to the calculation results, the opposite and parallel patterns are the most favored, while the inverse pattern is almost impossible because of the torsional strain it imposes on LX. Therefore, a total of nine possible apportionment patterns, labeled from I to IX, can be found within a ZIF cage (Figure 15).

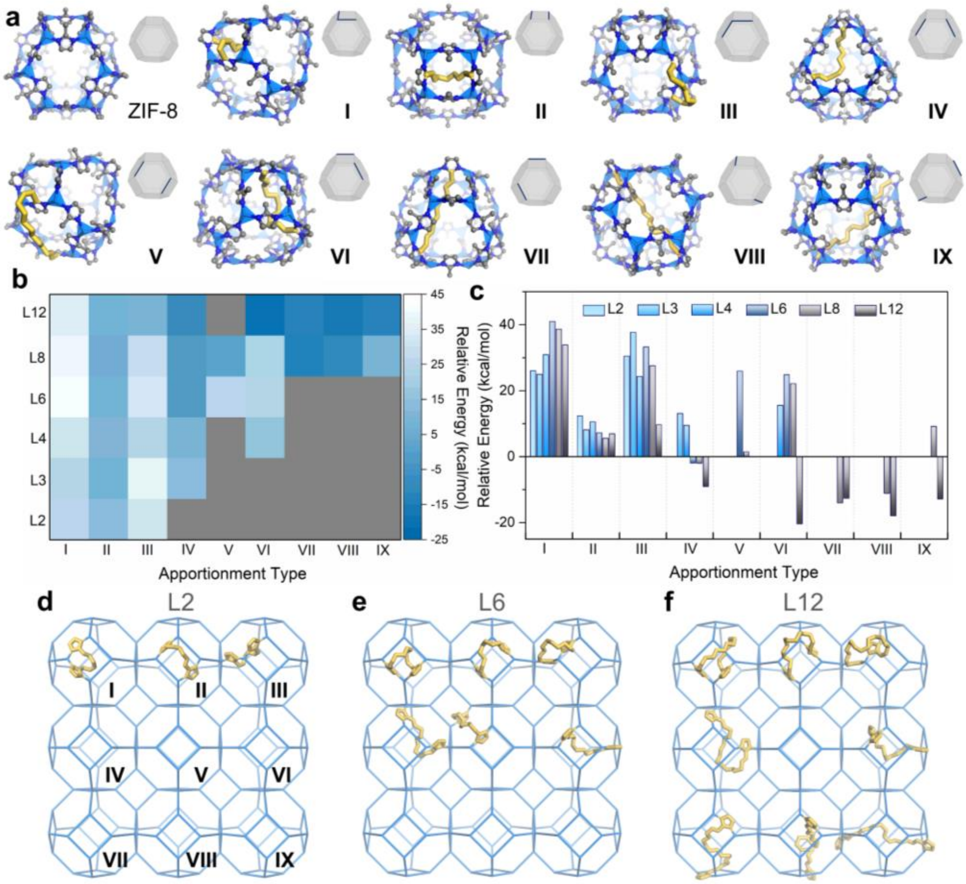

Figure 15. (a) The cage structure of ZIF-8 and nine possible apportionment types with linked template linkers LX; (b-c) Illustration of energy changes (unit: kcal/mol) after the exchange of 2-methylimidazole pairs with a chain template (LX, X = 2, 3, 4, 6, 8 and 12); (d-f) Illustration of possible link modes of L2, L6 and L12 within ZIF-8 cages.

According to density-functional calculations performed by the DMol^3 program of Materials Studio, relative energies of substitution can be obtained by subtracting the energy of ZIF-8 and LX from that of ZIF-8-LX (Figure 15, Table 1).[49] Remarkably, for

LX with a longer chain length, more diverse substitution patterns can be accessed. In general, the results shown that a shorter linker tends to connect adjacent positions with parallel ligands because of the length limitation, while for a longer linker, although with increased freedom and length, its torsion strain becomes a dominant factor for spatial distribution, as a result, it prefers a non-distortion pattern and substitutes two distant opposite ligands (Table 1). Our results here exemplify the idea of *ab initio* synthesis with predictable arrangement of functional groups within MTV-MOFs, which provides a tool for sequence manipulation in multi-component materials.

2.4 Conclusions

In conclusion, our results here exemplify the idea of *ab initio* synthesis with predictable arrangement of functional groups within MTV-MOFs. The imprinted apportionment within ZIF-8 was achieved by pre-incorporating interlocked linkers into framework materials and subsequent cleavage, leading to the formation of architectures with controlled heterogeneity. The detailed apportionment of functional groups was further analyzed by computational methods, showing that the programmable distribution of template linkers can be regulated by the variable linker lengths. This synthetic approach also enables investigations into other ZIF materials, or even carboxylate-based MOFs such as UiO-66, which is a vital design feature of future materials for precise control over pore environment and functionality sequences.

CHAPTER III

CREATING HIERARCHICAL PORES IN MULTICOMPONENT MOFS*

3.1 Introduction

Most MOFs exhibit microporosity, which impedes the diffusion of large molecules. Their structural integrity is often compromised when they are exposed to moisture, aqueous solution or high temperature, which limits their utility in catalysis and other applications.[50] Furthermore, when a microporous MOF is used to immobilize enzyme and other large-size catalysts, the active-site accessibility and catalytic activity will plummet because of pore blockage.[51] Thus, sufficient pore size, appropriate stability and hierarchical porosity are three prerequisites for open frameworks designed for drug delivery, enzyme immobilization and catalysis involving large molecules.

Currently, two main approaches, direct or templated synthesis, have been developed to build hierarchically porous MOFs (HP-MOFs). PCN-222, PCN-333 and NU-1000 are HP-MOFs from direct synthesis.[52-54] Yet the number of such MOFs, whose pore size distribution is predetermined by the linker length and MOF topology, is limited. In the latter approach, templates are incorporated at random in the framework during the *in situ* MOF synthesis.[55-61] Although the removal of template molecules may create mesopores inside the MOF, it often triggers partial or even total collapse of the

---

* This chapter is reproduced with permission from Feng, L.; Yuan, S.; Zhang, L.-L.; Tan, K.; Li, J.-L.; Kirchon, A.; Liu, L.-M., Zhang, P.; Han, Y.; Chabal, Y. J.; Zhou, H.-C., Creating Hierarchical Pores by Controlled Linker Thermolysis in Multivariate Metal-Organic Frameworks, *J. Am. Chem. Soc.* **2018**, 140 (6), 2363-2372, Copyright 2018 by American Chemical Society.

framework, leading to reduced crystallinity, low porosity, and poor stability. An unconventional alternative is to judiciously utilize labile chemical bonds or linkers susceptible to cleavage for the construction of porous materials, which should play an essential role in making HP-MOFs that could not be obtained otherwise.[62, 48, 63-64]

This pore engineering strategy based on labile chemical bonds has been explored extensively recently, leading to MOF construction strategies such as linker installation, linker labilization, solvent-assisted ligand incorporation and modulator removal in Zr-MOFs.[28-29, 65-66] Linker installation and solvent-assisted ligand incorporation both utilize acid-base chemistry between the hydroxyl groups on the coordinatively-unsaturated $Zr_6O_4(OH)_8(H_2O)_4$ clusters and linear linkers or terminal ligands. The terminal –OH/H_2O on these positions are further replaced by carboxylates in the solution postsynthetically. Linker labilization and modulator removal are two reverse processes to linker installation and solvent-assisted ligand incorporation. In modulator removal, a MOF is initially constructed with coordinatively-saturated clusters and modulator as terminal ligands; the terminal ligands are subsequently removed by activation under vacuum at high temperatures. This method leads to the formation of a more open framework with a large number of open coordination sites, which could act as catalytic centers in Lewis acid catalyzed reactions. However, the pore size of this resulting microporous framework increases only slightly, which is still unsuitable for applications involving large molecules. In contrast, linker labilization is a powerful tool to produce hierarchically porous structures with precisely controllable pore size distributions. A mixed-linker MOF is constructed with a “pre-labile” linker, which represents a nonlabile linker that can be converted to a labile one in a single step. The defects are created subsequently by splitting the “pre-labile” linker into two labile monocarboxylates under acidic conditions. Yet, several concerns still remain in linker labilization. First, the relatively long ligand used in PCN-160 would lead to an overall compromised stability.[67] Secondly, linker labilization has only been successful in a few particular examples, which highly restricts its application scope. This is because the “pre-labile” linker used in the framework is intrinsically reactive, and therefore decomposes under common synthetic conditions. This in turn makes it challenging to incorporate the “pre-labile” linkers into the framework. Therefore, it is urgent to find highly stable prototypical MOFs with relatively stable substitutes for previously reported imine-based linker, which can still undergo linker decomposition post-synthetically, in order to prepare ultrastable HP-MOFs with large pore sizes.

Herein, we introduce a powerful and general strategy, called linker thermolysis, to create mesopores in a series of microporous MOFs controllably. Initially, a multivariate MOF (MTV-MOF) is built from ordinary and thermal-sensitive (thermolabile) linkers (Scheme 4). The thermolabile linker can then be selectively cleaved in the framework through a decarboxylation process, by carefully controlling the decomposition temperature (Scheme 5). Hierarchical pores are created while the crystallinity and chemical stability remain after linker thermolysis. It is analogous to the modulator removal process, a thermal method to remove terminal ligands instead of bridging ones as in linker thermolysis. There exists a stark contrast between the stability of common and thermolabile linkers due to their distinct functional groups, which leads to selective thermolysis.[68-69] Not only does linker thermolysis allow for the generation of tunable hierarchically porous structures in a series of ultrastable MOFs with various clusters and functional groups, but it can also produce ultrasmall metal oxide (MO) nanoparticles immobilized in the framework. This resulting composite material, denoted as MO@HP-MOF, offers new opportunities for large molecule adsorption and catalysis.

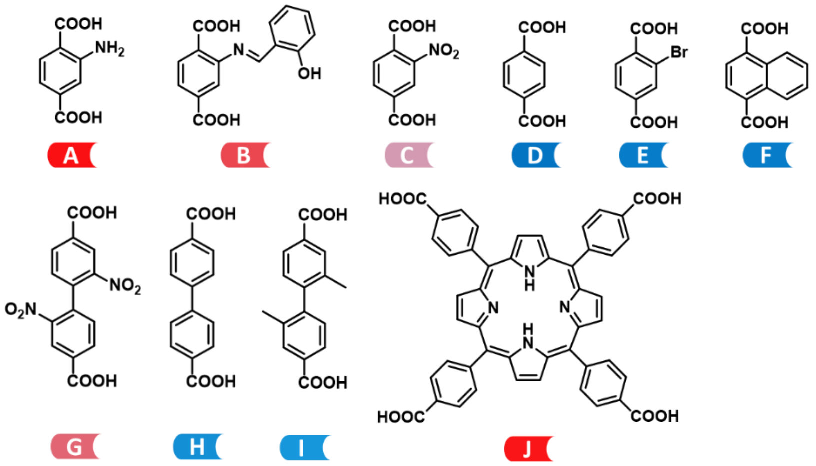

Scheme 4. Organic linkers (A-J) used in this work.

3.2 Experimental Section

Synthesis of UiO-66-NH$_2$-R% (R= 0, 9, 17, 26, 32, 41, 100). ZrOCl$_2$ (300 mg), H$_2$BDC (200, 180, 160, 140, 120, 100, 0 mg, respectively), H$_2$BDC-NH$_2$ (0, 20, 40, 60, 80, 100, 200 mg, respectively), acetic acid (10 mL) and DMF (10 mL) were charged in a Pyrex vial. The mixture was heated in a 120ºC oven for 24 h. After cooling to room temperature, the resulted powder was separated by centrifugation and washed several times with aliquots of DMF and EtOH, respectively. The solvent was removed under vacuum at 150°C for 12 h.

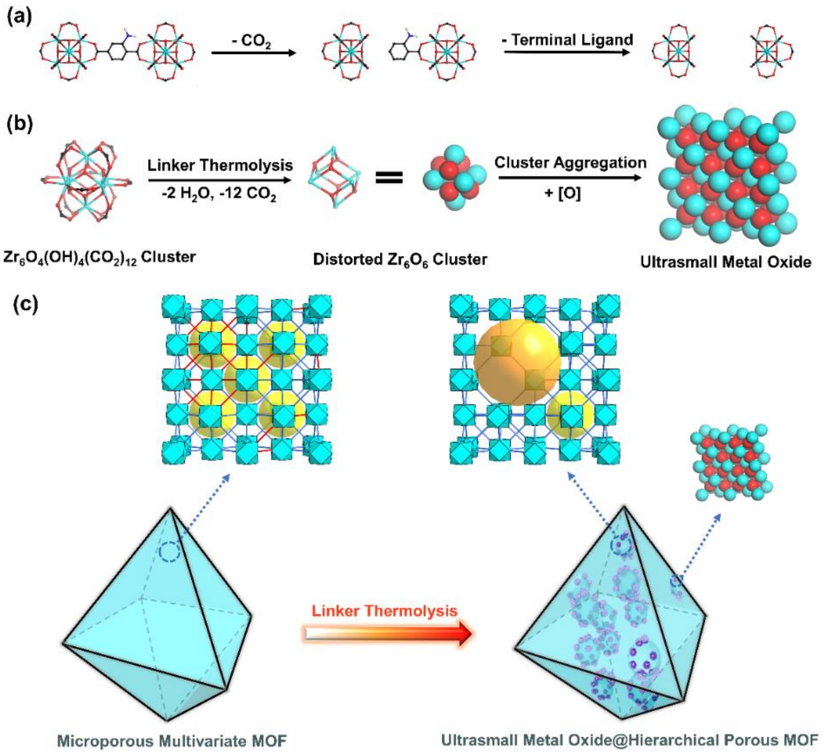

Scheme 5. Mechanism of hierarchically porous structure formation. (a) The amino functionalized linker tends to undergo a decarboxylation process under relatively low temperature; (b) $Zr_6O_4(OH)_4(CO_2)_{12}$ clusters are transformed into decarboxylated Zr_6O_6 clusters after linker thermolysis; (c) Overall, the microporous MTV-MOF, UiO-66-NH_2-R%, is converted into ultrasmall MO@HP-MOFs composites through controlled linker thermolysis.

Synthesis of HP-UiO-66-NH$_2$-R%-Temp-Time. Activated samples UiO-66-NH$_2$-R% (about 120 mg) were placed in a thermostatic furnace. The samples were heated at a certain temperature (300 ºC, 325 ºC, 350 ºC, 375 ºC, 400 ºC, respectively) for a certain period of time (15 min, 30 min, 60 min, 120 min, 180 min, 240 min, respectively) under air. After cooling to room temperature, the samples were activated again under vacuum at 150 ^{o}C for 12 h before gas sorption experiments.

N$_2$ sorption isotherm. Gas sorption measurements were conducted using a Micrometritics ASAP 2020 system. Prior to gas sorption measurements, about 100 mg MOF materials UiO-66-NH$_2$-R% were washed thoroughly with DMF and water to remove any remaining acetic acid, and exchanged by ethanol for 3 days, during which the solvent was decanted and freshly replenished three times every day. The solvent was then removed under vacuum at 150 ^{o}C for 12 h, yielding porous material. After linker thermolysis, about 100 mg UiO-66-NH$_2$-R%-*Temp*-*Time* was treated under vacuum at 150 ^{o}C for 8 h before gas sorption experiment.

BET Analysis. The determination of the BET surface of UiO-66-NH$_2$-26% and UiO-66-NH$_2$-26%-350^{o}C-120 min is demonstrated as an example in **Figure 16-17**. The nitrogen adsorption isotherm obtained is displayed in part a) of the figure. The data presented in the rest of the figure is derived from this isotherm. Part b) of the figure concerns the 1st consistency criterion. As indicated, $\boldsymbol{V(1-P/P_0)}$ increases continuously as a function of the relative pressure $\boldsymbol{P/P_0}$ until $\boldsymbol{P/P_0}$ = 0.050, a value highlighted by the vertical dashed line on the figure. In accordance with the 1st consistency criterion, the entire $\boldsymbol{P}/\boldsymbol{P_0}$ range used for the BET analysis must be ≤ 0.050. Displayed in part c) of the figure is the BET plot in which the linear range was chosen. In order to maximize the correlation ($R^2 = 0.9999$), only the points shown in the plots were included in the fit. In accordance with the 2nd consistency criterion, the value for $\mathbf{1}/(\sqrt{\boldsymbol{C}}+\mathbf{1})$ (= 0.034, as highlighted by the vertical dashed line) is well within the chosen pressure range ($\boldsymbol{P}/\boldsymbol{P_0}$ = 0.004 - 0.050). Finally, the table in the figure provides all the information relevant to the BET analysis. In accordance with the 3rd consistency criterion, the value of the BET constant, $\boldsymbol{C}$, is positive (= 843.4).

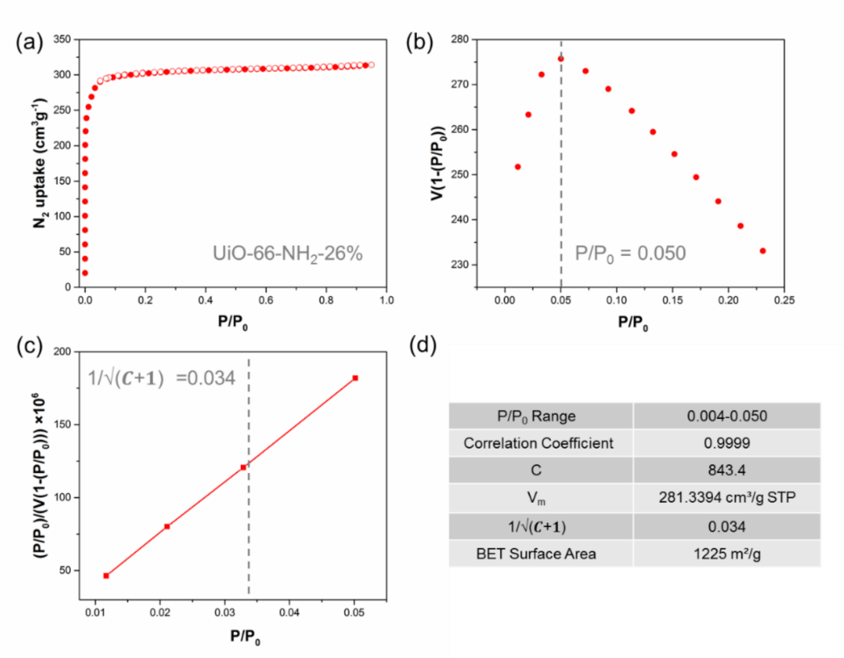

P/P_0 Range	0.004-0.050
Correlation Coefficient	0.9999
C	843.4
V_m	281.3394 cm³/g STP
$1/\sqrt{(C+1)}$	0.034
BET Surface Area	1225 m²/g

Figure 16. BET analysis of UiO-66-NH2-26%.

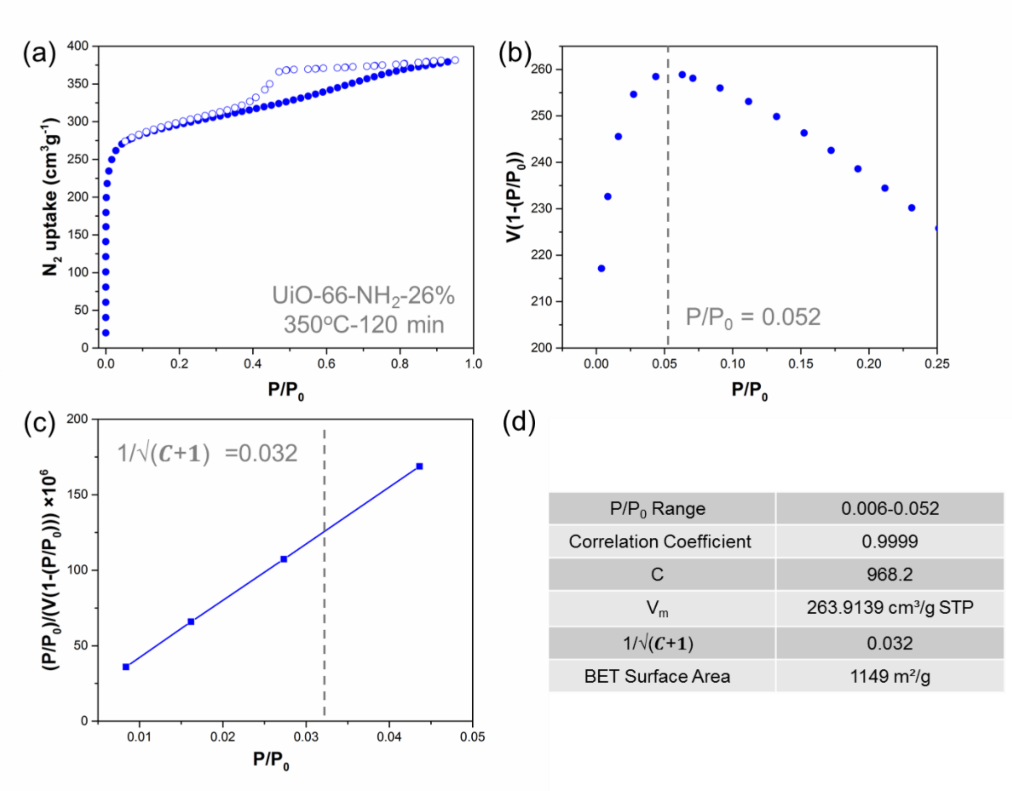

P/P_0 Range	0.006-0.052
Correlation Coefficient	0.9999
C	968.2
V_m	263.9139 cm³/g STP
$1/\sqrt{(C+1)}$	0.032
BET Surface Area	1149 m²/g

Figure 17. BET analysis of UiO-66-NH$_2$-26%-350^{o}C-120 min.

***In situ* infrared (IR) spectroscopy.** *In situ* IR measurements upon annealing were performed on a Nicolet 6700 FTIR spectrometer (purchased from Thermo Scientific Inc., USA) equipped with a liquid N_2 -cooled mercury cadmium telluride MCT-A detector. The MOFs (powder, ~5 mg) were gently pressed onto a KBr pellet (~1 cm diameter, 1–2 mm thick) and placed in the pressure cell, which is installed in the sample compartment of the infrared spectrometer with the sample at the focal point of the beam and connected to the nitrogen purge.

X-ray photoelectron spectroscopy (XPS). XPS measurements were performed with a Perkin Elmer PHI system. The sample after thermal treatment at 350 °C for 5 min and 3.5 h respectively was transferred into the XPS chamber with a base pressure of <1.0 × 10−9 Torr. Al Kα (1486.6 eV) X-ray source at a chamber was used to excite photoelectrons. The spectra were recorded by using a 16-channel detector with a hemispherical analyzer.

Thermogravimetric analysis. About 10 mg of the sample was heated on a TGA Q500 thermogravimetric analyzer from room temperature to 600 °C at a rate of 5 °C·min^{-1} under air flow of 20 mL·min^{-1} (Figure 18). TGA-MS analyses were performed in STA449C-QMS403 C Thermal Analysis-Quadrupole Mass Spectrometer.

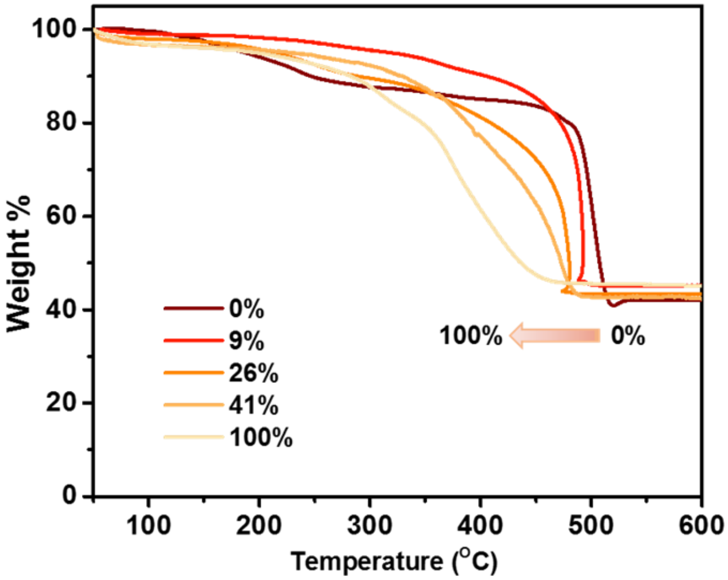

Figure 18. Thermogravimetric analyses of UiO-66-NH_2-R%.

Powder X-ray diffraction (PXRD). PXRD was carried out with a Bruker D8-Focus Bragg-Brentano X-ray Powder Diffractometer equipped with a Cu sealed tube (λ = 1.54178 Å) at 40 kV and 40 mA (Figure 19).

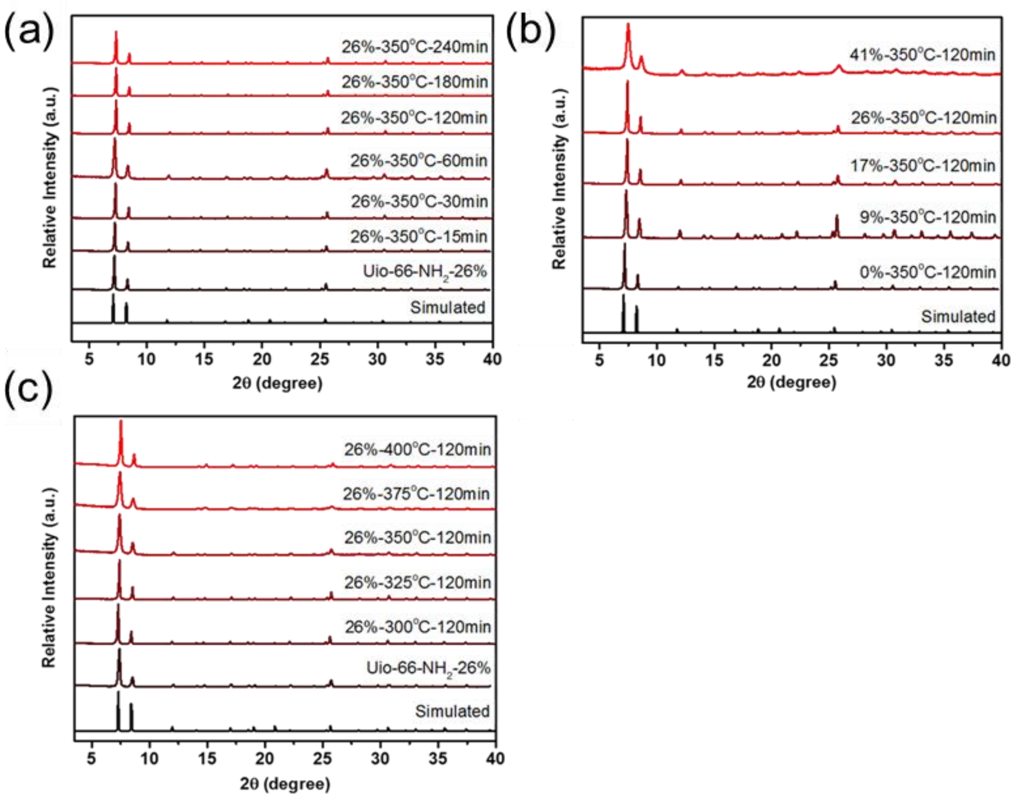

Figure 19. PXRD patterns of UiO-66-NH_2-R%-*Temp-Time*.

^{1}H NMR spectroscopy. Nuclear magnetic resonance (NMR) data were collected on a Mercury 300 spectrometer (Figure 20, Table 2). For ^{1}H NMR spectroscopy, the activated samples (around 10 mg) were dissolved in 600 µL DMSO-d_6 solution containing 20 µL HF.

Transmission electron microscopy (TEM). TEM experiments were conducted on a FEI Tecnai G2 F20 ST microscope (America) operated at 200 kV.

ICP-MS analysis. Calibration standards were prepared from certified reference standards from RICCA Chemical Company. Samples were further analyzed with a Perkin Elmer NexION® 300D ICP-MS. Resulting calibration curves have minimum R^2 = 0.9999. Additionally, in order to maintain accuracy, quality control samples from certified reference standards and internal standards were utilized. The individual results of the triplicate samples were averaged to determine the metal concentration.

Figure 20. Photographs images of UiO-66-NH_2-R% and UiO-66-NH_2-R%-Temp-Time (R=9, 26, 41).

Table 2. The ratio of thermolabile linker BDC-NH_2 in MOFs calculated by ^{1}H-NMR spectra.

Starting weight of BDC-NH_2/BDC (mg/mg)	0	20/180	40/160	60/140	80/120	100/100
Starting ratio of BDC-NH_2 (mol%)	0	9%	19%	28%	38%	48%
Actual ratio of BDC-NH_2 (mol%)	0	9%	17%	26%	32%	41%

Synthesis of UiO-66-BD and HP-UiO-66-BD. UiO-66-BD was prepared through post-synthetic modification based on the reported procedure with minor modifications.[70] Activated UiO-66-NH_2-26% (about 300 mg) was suspended in 10 ml toluene solution containing 50 mg salicylaldehyde. After standing for seven days, the powder shown a noticeable yellow hue; the resulted powder then was separated by centrifugation and washed several times with toluene and EtOH, respectively. The solvent was removed under vacuum at 150 ^oC for 12 h, yielding microporous material. Activated samples UiO-66-BD (about 120 mg) were placed in a thermostatic furnace. The samples were heated at 350 ºC for 120 min under air. After cooling down to room temperature, the samples were activated again under vacuum at 150^{o}C for 12 h before gas sorption experiment (Figure 21).

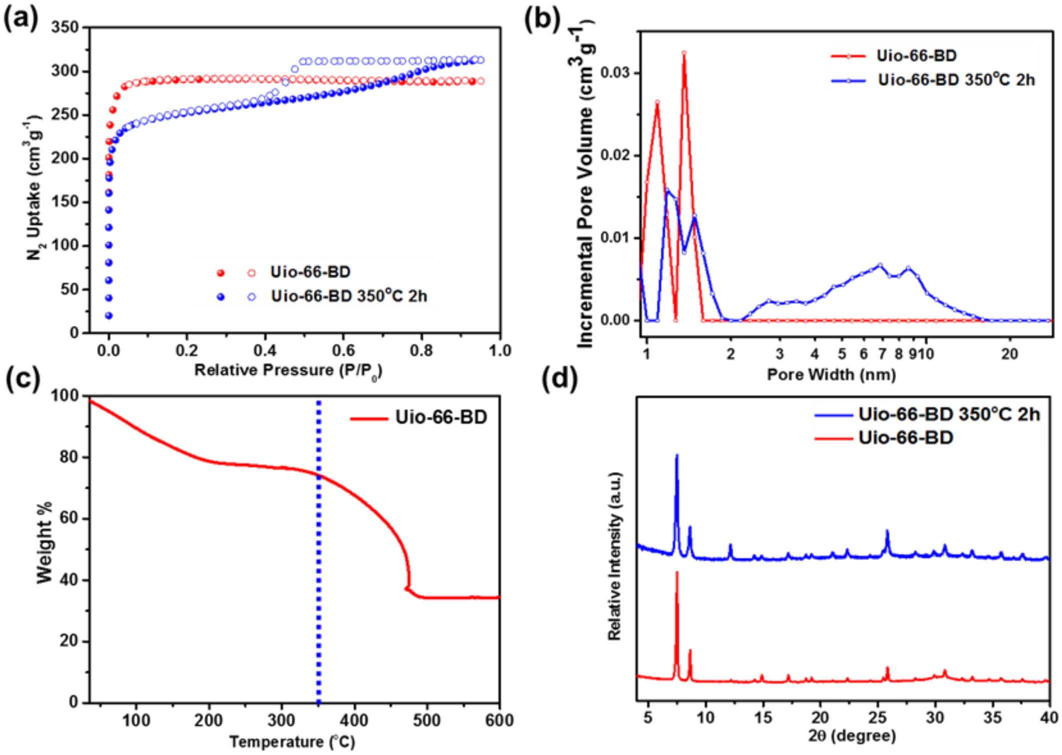

Figure 21. N_2 uptakes (a), pore size distributions (b), TGA curve (c) and PXRD patterns (d) of UiO-66-BD and HP-UiO-66-BD. The dashed line in (c) indicates the thermal treatment temperature.

Synthesis of UiO-66-CD and HP-UiO-66-CD. $ZrOCl_2$ (300 mg), H_2BDC (140 mg), $H_2BDC-NO_2$ (70 mg), acetic acid (10 mL) and DMF (10 mL) were charged in a Pyrex vial. The mixture was heated in 120 ºC oven for 24 h. After cooling down to room temperature, the resulted powder was separated by centrifugation and washed several times with DMF and EtOH, respectively. The solvent was removed under vacuum at 150 ºC for 12 h, yielding microporous material. Activated samples UiO-66-CD (about 120 mg) were placed in a thermostatic furnace. The samples were heated at 400 ºC for 60 min under air. After cooling down to room temperature, the samples were activated again under vacuum at 150 ºC for 12 h before gas sorption experiment (Figure 22).

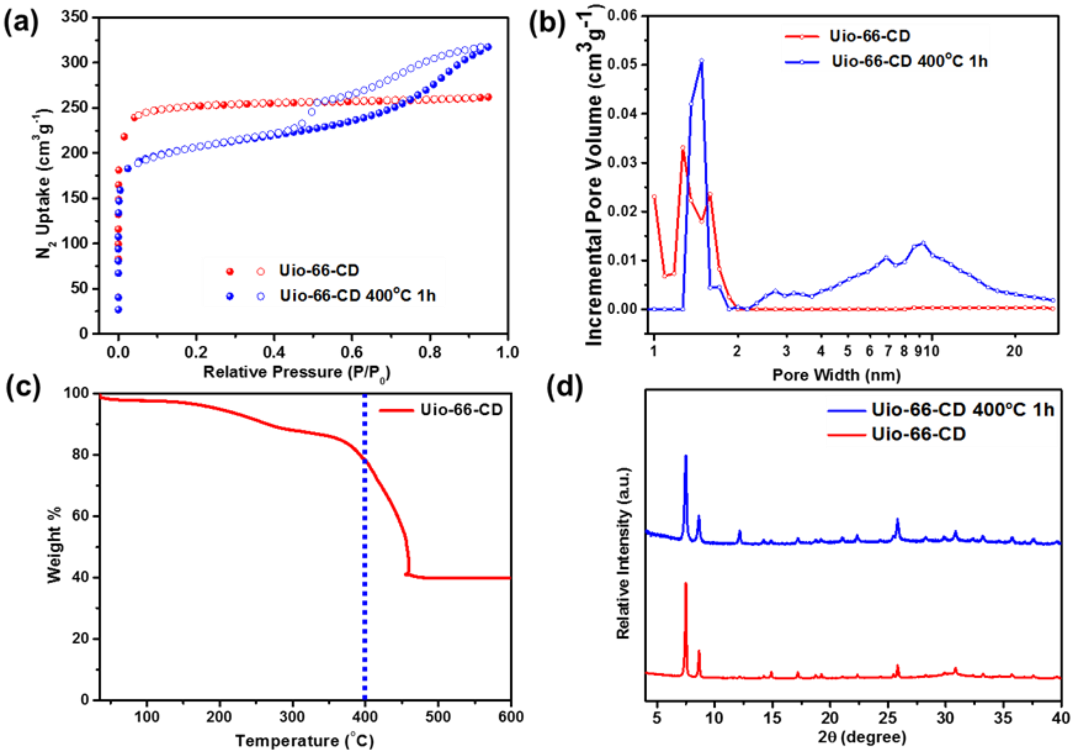

Figure 22. N_2 uptakes (a), pore size distributions (b), TGA curve (c) and PXRD patterns (d) of UiO-66-CD and HP-UiO-66-CD. The dashed line in (c) indicates the thermal treatment temperature.

Synthesis of UiO-66-AE and HP-UiO-66-AE. $ZrOCl_2$ (300 mg), H_2BDC-Br (160 mg), H_2BDC-NH_2 (50 mg), acetic acid (10 mL) and DMF (10 mL) were charged in a Pyrex vial. The mixture was heated in 120 °C oven for 24 h. After cooling down to room temperature, the resulted powder was separated by centrifugation and washed several times with DMF and EtOH, respectively. The solvent was removed under vacuum at 150 °C for 12 h, yielding microporous material. Activated samples UiO-66-AE (about 120 mg) were placed in a thermostatic furnace. The samples were heated at 350 °C for 60 min under air. After cooling down to room temperature, the samples were activated again under vacuum at 150 °C for 12 h before gas sorption experiment (Figure 23).

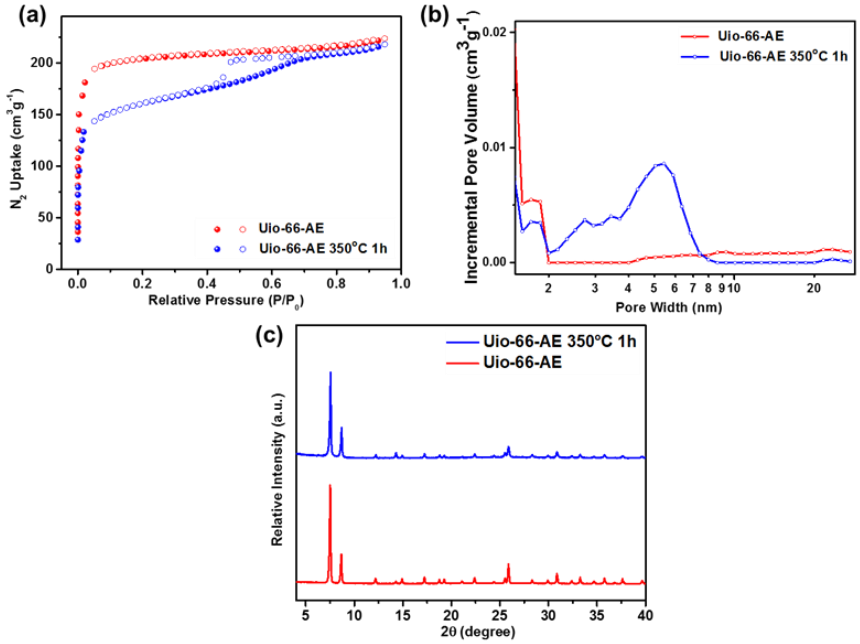

Figure 23. N_2 uptakes (a), pore size distributions (b), and PXRD patterns (c) of UiO-66-AE and HP-UiO-66-AE.

Synthesis of UiO-66-AF and HP-UiO-66-AF. $ZrOCl_2$ (300 mg), 1,4-H_2NDC (160 mg), H_2BDC-NH_2 (50 mg), acetic acid (10 mL) and DMF (10 mL) were charged in a Pyrex vial. The mixture was heated in 120 ºC oven for 24 h. After cooling down to room temperature, the resulted powder was separated by centrifugation and washed several times with DMF and EtOH, respectively. The solvent was removed under vacuum at 150 ºC for 12 h, yielding microporous material. Activated samples UiO-66-AF (about 120 mg) were placed in a thermostatic furnace. The samples were heated at 350 ºC for 60 min under air. After cooling down to room temperature, the samples were activated again under vacuum at 150 ºC for 12 h before gas sorption experiment (Figure 24).

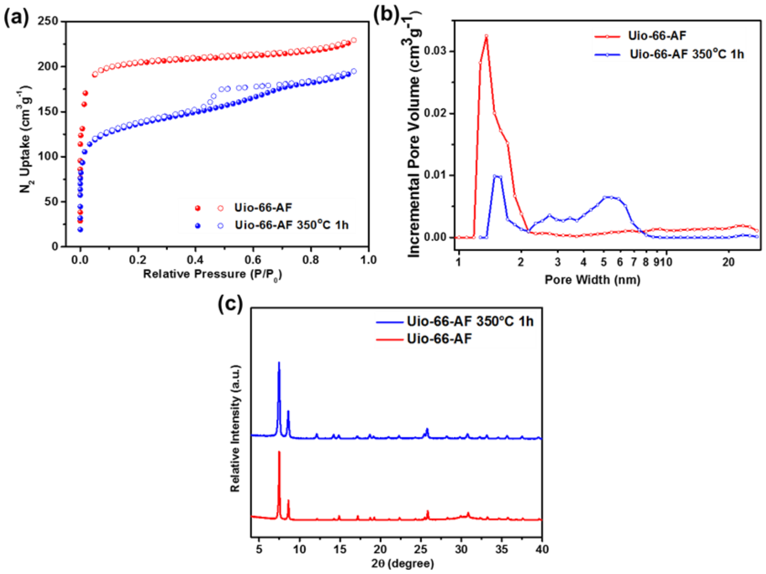

Figure 24. N_2 uptakes (a), pore size distributions (b), and PXRD patterns (c) of UiO-66-AF and HP-UiO-66-AF.

Synthesis of UiO-67-GH and HP-UiO-67-GH. $ZrCl_4$ (200 mg), H_2BPDC (100 mg), TFA (2.0 mL) and DMF (20 mL) were charged in a Pyrex vial. The mixture was heated in 120 ºC oven for 5 days. After cooling down to room temperature, the resulted single crystals UiO-67 was separated by centrifugation and washed several times with DMF. UiO-67 (120 mg), $H_2BPDC\text{-}(NO_2)_2$ (50 mg), and DMF (20 mL) were charged in a Pyrex vial. The mixture was heated in 85 ºC oven for 24 h. After linker exchange, the crystals were separated by centrifugation and washed several times with DMF and EtOH, respectively. The solvent was removed under vacuum at 150 ºC for 12 h, yielding microporous material. The ratio of thermolabile linker G in MOFs was calculated by ^{1}H-NMR spectra. Activated samples UiO-67-GH (about 120 mg) were placed in a thermostatic furnace. The samples were heated for 30 min under air at 420 ºC. After cooling down to room temperature, the samples were activated again under vacuum at 150 ºC for 12h before gas sorption experiment (Figure 25).

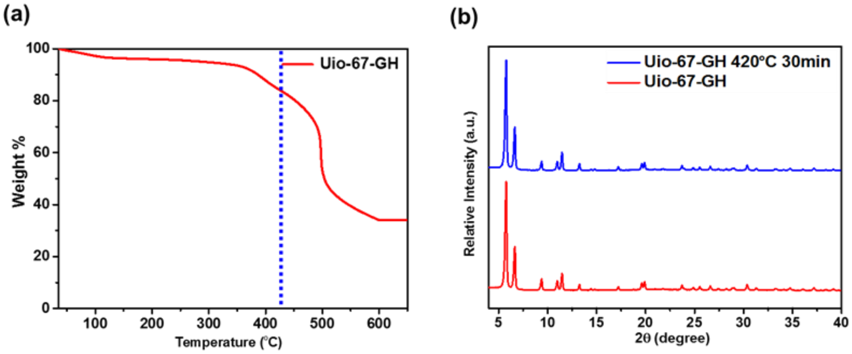

Figure 25. TGA curve (a) and PXRD patterns (b) of UiO-67-GH and HP-UiO-66-GH. The dashed line in (a) indicates the thermal treatment temperature.

3.3 Results and Discussion

UiO-66, one of the most studied MOFs, was firstly introduced as an example to illustrate our strategy because of its excellent stability and strong tolerance towards defects.[71-74] The linker, 2-Amino-1,4-benzenedicarboxylate (BDC-NH_2), was applied as the thermolabile linker, which can be easily removed under relatively low temperature (300 ^oC) through thermal decomposition. In contrast, UiO-66 with BDC as linker shows high thermal stability, starting decomposition at nearly 480 ^oC. The remarkable thermal stability differences provide an excellent platform to study the aforementioned selective linker thermolysis strategy. MTV-UiO-66-NH_2-R%, where R% stands for the percentage of the thermolabile linker determined by ^1H-NMR (Table 2, Figure 27), were synthesized with good crystallinity as indicated from PXRD patterns and TEM images. N_2 sorption isotherms indicated that MTV-UiO-66 samples were microporous as expected with an extra **reo**-type[75] micropore diameter of ~15 Å due to missing-cluster defects, which is very common in Zr- and Hf-MOFs.

Thermal stability of UiO-66-NH_2-R% was accessed by TGA (Figure 18). TGA plots indicate thermal stability of UiO-66-NH_2-R% decreases with increasing R%. UiO-66 samples with BDC-NH_2 ratios varying from 0 to 41% were prepared and treated with various temperatures for certain periods of time. The resulting materials are denoted as UiO-66-NH_2-R%-*Temp*-*Time*, where *Temp* represents the thermal treatment temperature and *Time* represents the thermal treatment time. PXRD measurements showed that the MOF materials after thermolysis possessed the same diffraction patterns as the parent

UiO-66 MOF (Figure 19). The crystal morphology was not affected by the relatively mild heating process as indicated by the TEM images of the respective particles (Figure 28). The N_2 sorption isotherms at 77 K demonstrated the formation of HP-MOF materials, which possess both micro- and mesopores (Figure 26).

In general, the porosities and pore sizes of these MOFs could be easily tuned through varying the thermolabile linker ratio, temperature and heat time (Figure 29). When sample UiO-66-NH_2-26%-350^{o}C was held under the temperature for different periods of 15 min, 30 min, 60 min, and 120 min, the porosities and N_2 uptakes increased as heating time became longer. Noticeable mesopores with an average diameter of 5.5 nm emerged after thermal treatment. The ratio of meso- to micropore volume increased proportionally with the elongated time period as indicated by N_2 uptake and pore size distribution. The effects of thermolysis temperature and thermolabile linker ratio on the porosity and pore size distribution were also studied. When UiO-66-NH_2-26%-120 min was set as the basis, the overall porosity and N_2 uptake increased as the thermolysis temperature elevated. A pronounced hysteresis loop, corresponding to mesopores with average diameter of 5.5 nm, arose when temperature reached 325^{o}C. Further temperature increase to 350 ^{o}C led to the augmentation of the proportion of 5.5 nm mesopores, however, the average pore size remained almost unchanged. When the temperature was raised to 375 ^{o}C, BDC-NH_2 decomposed completely, which caused the porosity expansion to 13 nm. In addition, when the thermolabile linker ratio increased, so did the porosity and N_2 uptake as expected.

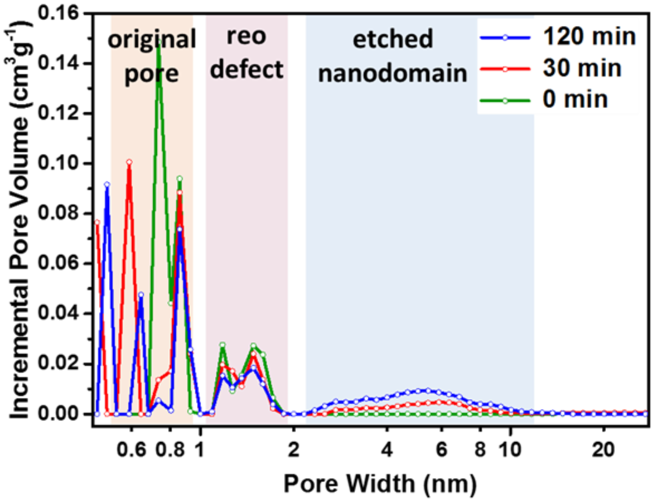

Figure 26. Pores size distribution of UiO-66-NH_2-26%-350°C treated with different times calculated by DFT method.

The hierarchical porosity is also corroborated by TEM images (Figure 28). After linker thermolysis, the HP-UiO-66 MOFs display a sponge-like morphology with defects randomly arranged throughout each particle. The crystallinity of all samples after thermal treatment remains intact as indicated by PXRD, although slightly broader PXRD peaks were observed for frameworks with a larger portion of mesopores (Figure 19). The stability of HP-MOFs toward aqueous solution has also been investigated. Although a large number of defects have been created inside the framework, HP-UiO-66 retained the chemical stability of the pristine UiO-66. The ultrastable nature of HP-UiO-66 is encouraging as MOF with hierarchical pores and high stability should be ideal for practical applications. Additionally, nanoparticles with ultrasmall sizes (1-3 nm) were generated from the linker thermolysis process. TEM images showed that the ultrasmall

ZrO_2 nanoparticles are well-dispersed in the framework by the clear lattice fringes with a lattice spacing of 0.295 nm, corresponding to a stack of the [101] planes of the tetragonal ZrO_2 lattice.[76-77]

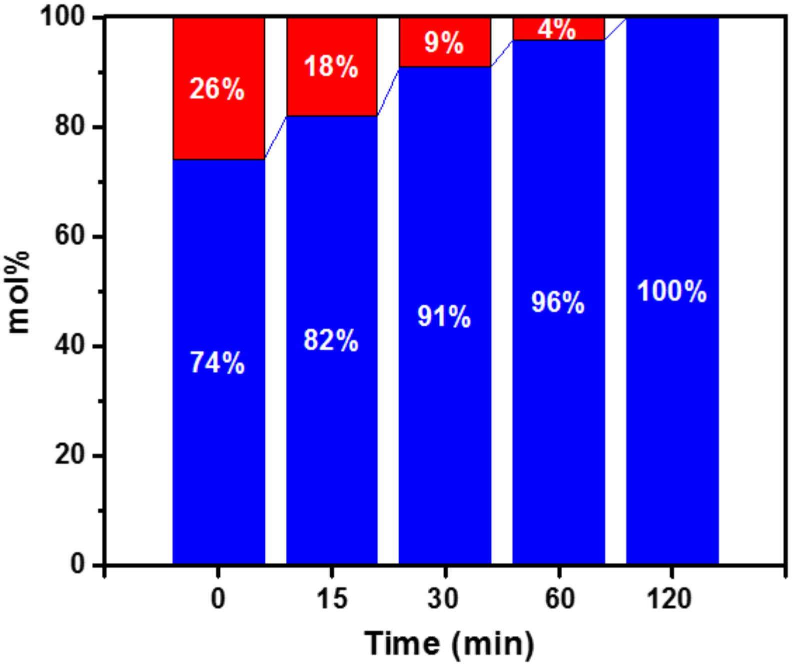

Figure 27. Linker ratio in UiO-66-NH_2-26%-350°C calculated by ^1H NMR of digested samples. The blue bar indicates the mol% of BDC and the red bar indicates the mol% of BDC-NH_2.

The decarboxylation mechanism of linker thermolysis was elucidated through many *in situ* and *ex situ* techniques. Combined TGA/MS studies were performed in air to determine the products of linker thermolysis. The TGA plots and corresponding MS signals under two conditions were summarized (Figure 30): (a) increasing temperature from 30 ^{o}C to 600 ^{o}C and (b) holding at a constant temperature of 350 ^{o}C. As indicated in Figure 30, a small amount of water and DMF solvent trapped inside the pores or coordinated on Zr_6 cluster firstly came out before temperature reached 300 ^{o}C. Between 300 ^{o}C and 400 ^{o}C (controlled linker thermolysis range), the amount of CO_2 dramatically increased while no other signal was detected, which clearly indicated a decarboxylation process before the collapse of the framework. When temperature reached 400 ^{o}C, a sharp peak with MS signal m/z = 78 appeared, corresponding to the cracking residue of the MOF linker. Additionally, to investigate the formation of mesopores, UiO-66-NH_2-26% was held at 350^{o}C and the gaseous products were analysed with TGA/MS. Only the signal of CO_2 could be detected after the removal of solvents, which confirmed the decarboxylation process of BDC-NH_2 in the framework.

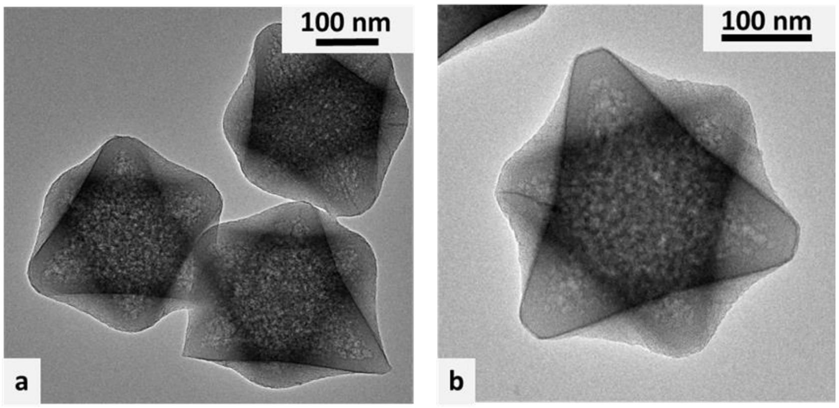

Figure 28. TEM images of UiO-66-NH_2-26% after thermal treatment (350^{o}C, 2h).

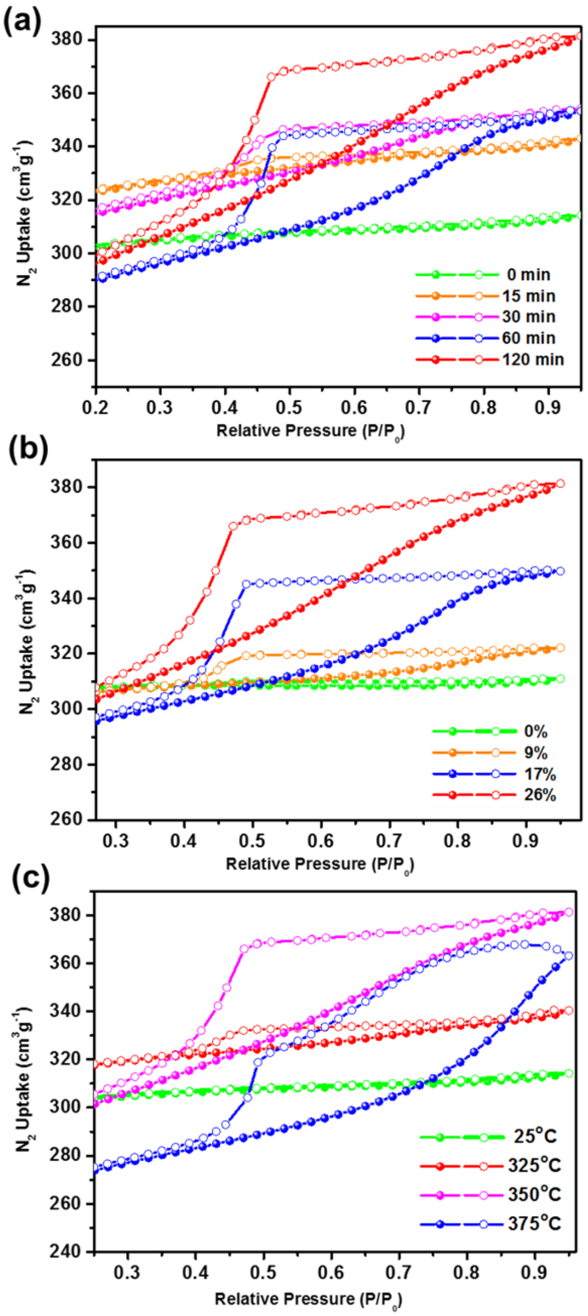

Figure 29. Hysteresis loop in type IV N_2 sorption isotherms of UiO-66-NH_2-R%-Temp-Time: UiO-66-NH_2-26%-350^{o}C treated with different time (a), UiO-66-NH_2-R%-350^{o}C-2h containing R% BDC-NH_2 (b), UiO-66-NH_2-26%-2h treated at different temperature (c).

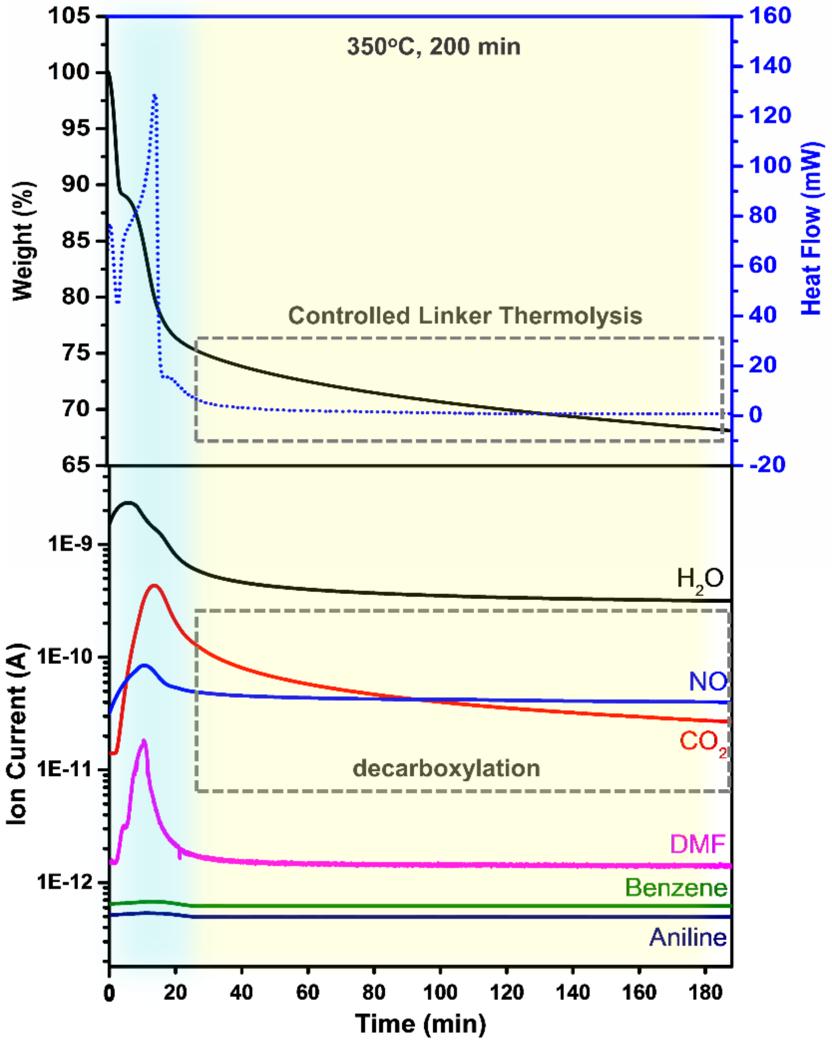

Figure 30. Linker thermolysis of UiO-66-NH_2-26% holding at a constant temperature of 350°C investigated by TGA-MS.

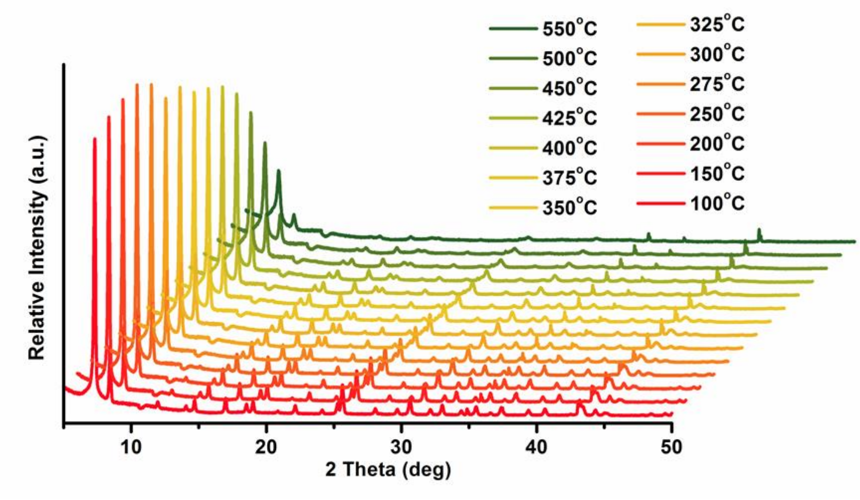

Figure 31. *In-situ* Variable Temperature PXRD patterns of UiO-66-NH_2-26%; Temperature interval 100°C-550°C; Step length 25°C; samples are hold on each temperature for 15 min.

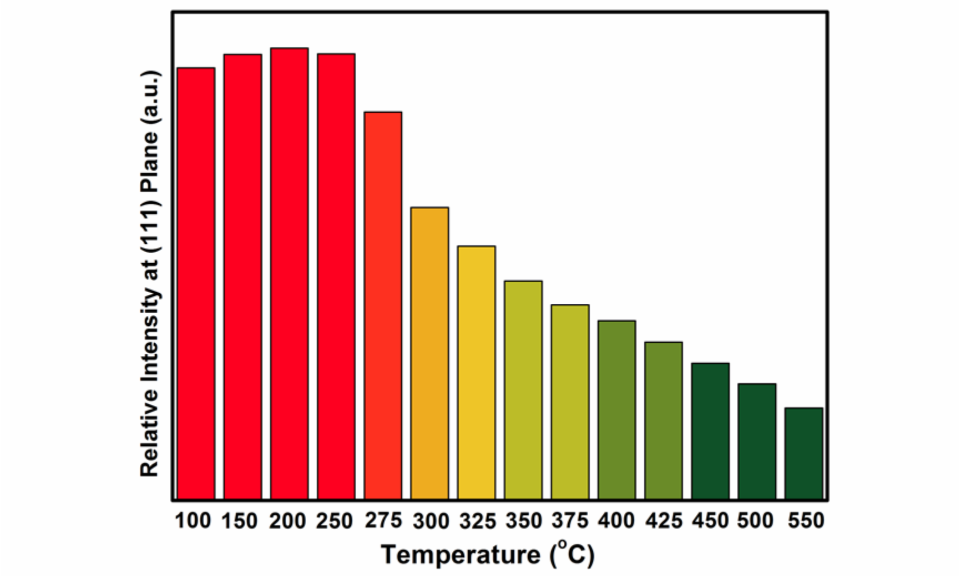

Figure 32. Decrease of relative intensity at (111) plane as indicated by VT-PXRD.

In situ infrared (IR) spectroscopy and *ex situ* X-ray photoelectron spectroscopy (XPS) were used to monitor the decarboxylation process of the sample upon thermal treatment. The losses (negative features) in the differential IR absorption spectra before 300 ^{o}C anneal are associated with solvent molecules including H_2O [ν(OH)] and DMF [ν(-CH_3) and ν(C=O)]. The process starts with dehydration of bridging μ_3-OH of $Zr_6O_4(OH)_4$ (loss of the 3676 cm^{-1} mode above 250 ˚C) and proceeds with a transition to a Zr_6O_6 cluster, as evidenced by a slight blue shift of the symmetric and asymmetric stretching bands[78] of the COO^- group bound to Zr metal center. Above 300 °C, there is a gradual loss of carboxylate bands (1582, 1428, 1393 cm^{-1}), particularly at 350 ^{o}C over the time observed, which was consistent with TGA-MS results. *Ex situ* XPS measurements, performed on UiO-66-NH_2-41%, after thermal treatment of sample at 350°C for ~5 min and 3.5 h, clearly show a decrease of the COO^-/Zr ratio from ~41% to ~25% after linker thermolysis at 350 °C for 3.5 h, which directly supports the decarboxylation inside the framework. Besides decarboxylation, there are also losses between 3500 to 3300 cm^{-1} and at 1257 cm^{-1}, associated with ν(-NH_2) and ν(C-N) modes, respectively, at 350 ˚C.[78] These observations indicate that the amino-functionalized linker is a thermolabile part of the framework. Finally, variable-temperature PXRD was also used to monitor the *in situ* transformation of MOF structure (Figure 31-32). The dramatic decline of the diffraction intensity of the [111] planes began at nearly 300 ^{o}C, which can be attributed to a structure change caused by the decarboxylation process (Scheme 6).

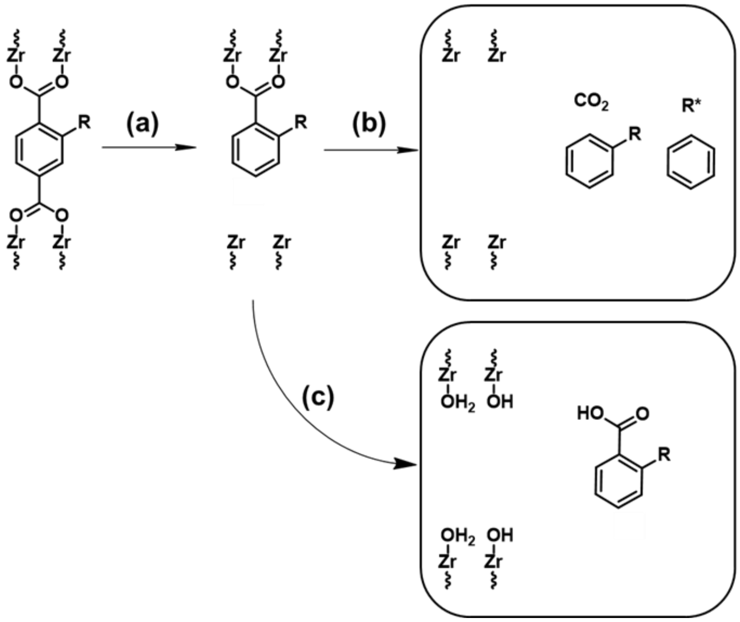

Scheme 6. Proposed mechanism of linker thermolysis: (a) decarboxylation process; (b) linker decomposition at high temperature; (c) terminal ligand removed by treatment in HCl/DMF solution at 85°C.

Investigating compositions of UiO-66-NH$_2$-R%-Temp-Time. Combing the results from ^{1}H NMR and TGA, we could calculate the composition of these materials approximately (Figure 33-34, Table 3). The total weight of linkers (BDC and BDC-NH$_2$) in the framework was determined by the TGA results. $X_{BDC}\%$ and $X_{BDC\text{-}NH2}\%$ were obtained from the ^{1}H NMR result.

$$\frac{m_{BDC} + m_{BDC-NH2}}{m_{ZrO2}} = \frac{n_{BDC} \cdot M_{BDC} + n_{BDC-NH2} \cdot M_{BDC-NH2}}{n_{ZrO2} \cdot M_{ZrO2}}$$

$$n_{Total} \cdot X_{BDC}\% = n_{BDC}$$

$$n_{Total} \cdot (1 - X_{BDC}\%) = n_{Total} \cdot X_{BDC-NH2}\% = n_{BDC-NH2}$$

For samples after thermal treatment, the amount of BDC is fixed with the original sample before linker thermolysis because of the unlikely decomposition of this thermostable linker at 350°C. The amount of BDC-NH_2 and its derivatives were calculated based on the rest weight loss. The results are shown in Table 3.

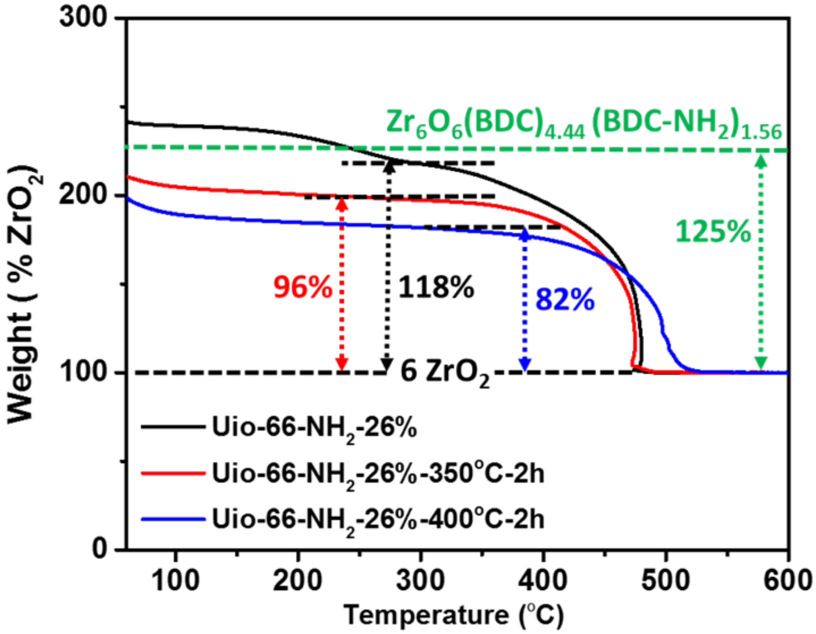

Figure 33. Thermogravimetric analyses of UiO-66-NH_2-26% before and after linker thermolysis. The green dash line refers to ideal defect-free UiO-66-NH_2-26%.

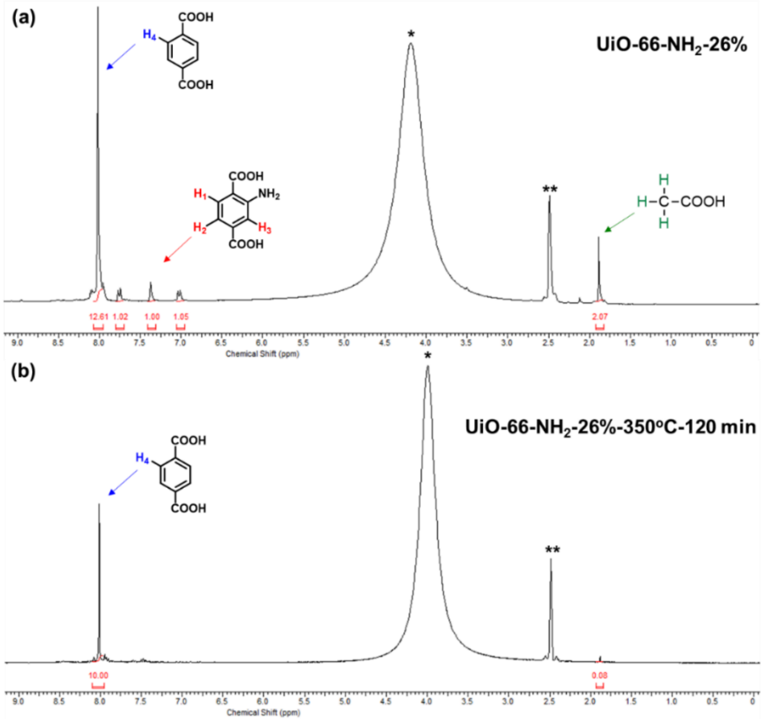

Figure 34. ^{1}H NMR of digested samples (a) UiO-66-NH_2-26% and (b) UiO-66-NH_2-26%-350^{o}C-120 min.

Table 3. Approximate composition and CN of cluster of UiO-66-NH_2 -R%-Temp-Time.

Sample Name	Average Composition	CN of Cluster
UiO-66-NH_2-26%	$Zr_{12}O_8(OH)_8$ $BDC_{7.6}$ $(BDC\text{-}NH_2)_{2.6}\cdot(H_2O)_{3.6}(OH)_{3.6}$	10.2
UiO-66-NH_2-26% -350^{o}C-2h	$Zr_{12}O_8(OH)_8$ $BDC_{7.6}$ $(D\text{-}BDC\text{-}NH_2)_{0.9}(H_2O)_{7.0}(OH)_{7.0}$*,†	8.5
UiO-66-NH_2-26% -400^{o}C-2h	$Zr_{12}O_8(OH)_8$ $BDC_{7.3}$ $(H_2O)_{9.4}(OH)_{9.4}$†	7.3

*D-BDC-NH_2 refers to BDC-NH_2 and its related derivatives.

†Although -OH and H_2O coordinated on the Zr_6 cluster would be removed above 300°C, when cooling to room temperature, these -OH and H_2O could easily be coordinated to Zr_6 cluster reversibly due to the presence of trace water in the environment.

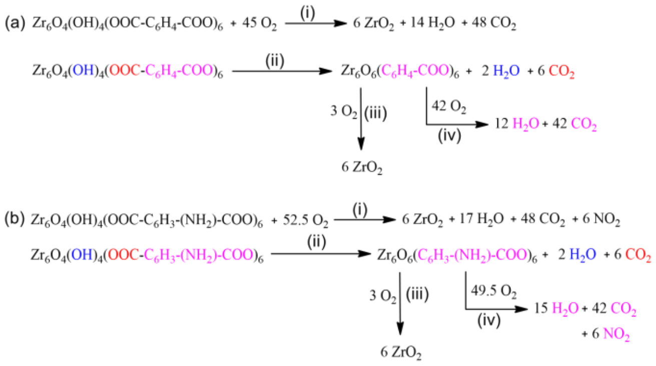

Figure 35. Composition analysis of MOF thermolysis showing thermal decomposition equation of UiO-66 (a) and UiO-66-NH_2 (b) in air or oxygen atmosphere.

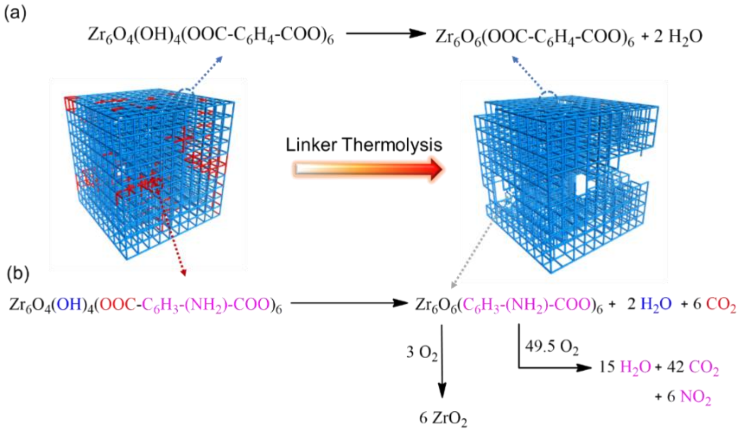

Figure 36. Illustration of linker thermolysis of UiO-66-NH_2-26% from a chemical equation perspective.

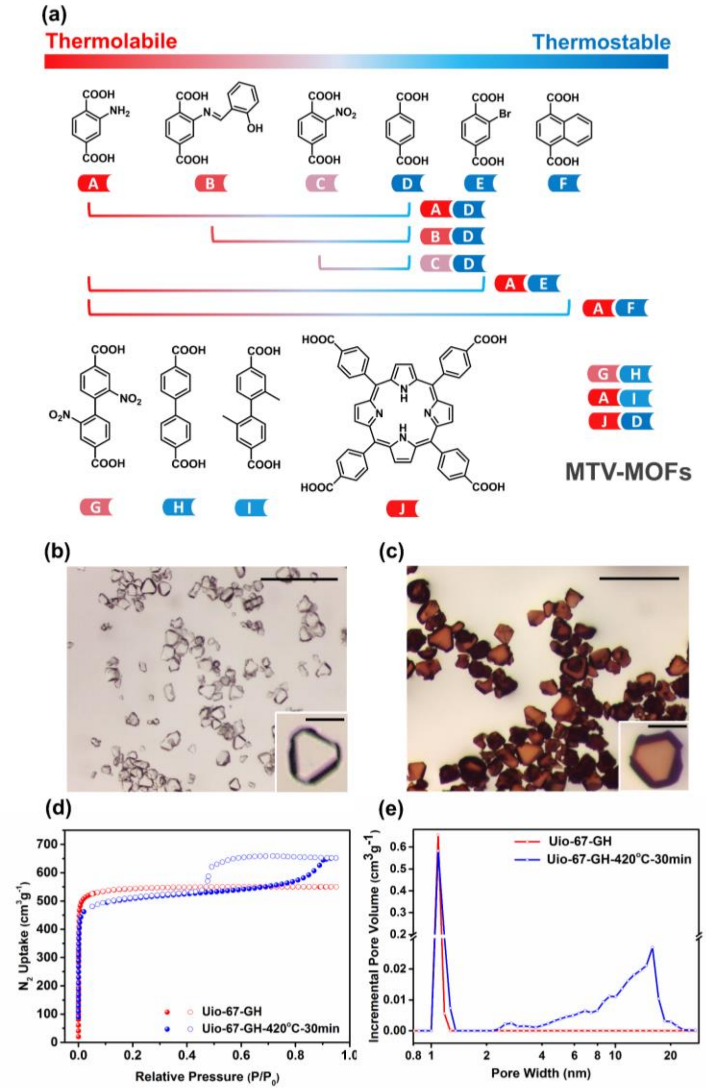

Figure 37. Versatility of controlled linker thermolysis. (a) Versality of linker thermolysis to construct HP-MOFs with various linkers A-J showing different thermal stability. Combination of relatively thermolabile and relatively thermostable linkers resulted in MTV-MOFs capable of controllable linker thermolysis. (b)(c) Images of UiO-67-GH crystals before and after linker thermolysis; (d)(e) N_2 sorption isotherms and pore size distributions of UiO-67-GH before and after linker thermolysis. Scale bar is 500 µm in (b)(c) and 100 µm in (b)(c) insert figures.

As described above, thermally susceptible linkers tend to go through a decarboxylation process at relatively low temperatures while the other parts of the frameworks remain intact, as vacancies are created after the removal of CO_2 (Figure 35-36). Unlike the creation of missing linker and cluster defects by linker labilization that takes place in solution, linker thermolysis goes through a cluster aggregation process. An interesting phenomenon in solid solution called Ostwald ripening may help explain the cluster aggregation. This occurs because the freshly formed decarboxylated Zr_6O_6 clusters[79], with the assistance of oxygen species, tend to aggregate to form a "giant" ZrO_2 cluster (ultra-small ZrO_2 nanoparticle), which is a thermodynamically driven and spontaneous process. The oxygen species presumably originate from the reduced oxygen during the oxidation of organic species. Based on the proposed mechanism, after thermolabile linkers undergo a decarboxylation process, the resulting fragments, terminal ligands, are still coordinated to the cluster. Two methods were then adopted to remove these terminal ligands in order to achieve even larger pore sizes: (1) thermal activation at high temperatures; (2) treatment with diluted acid solution.

To examine whether linker thermolysis could function as a general approach, we extended the strategy to other common linkers and other types of clusters for developing various highly stable HP-MOFs (Figure 37). The influences of different functional groups on the thermal stabilities of the UiO-66 series were investigated. Herein we introduced six ligands, BDC and its derivatives (donated as A-F), and combined two linkers to form the corresponding sets of MTV-MOFs. Each MTV-MOF possesses relative thermolabile and relative thermostable linkers. It is noteworthy that the TGA plots provided us direct information about the linker thermal stability.[68-69] Guided by the weight loss information of MTV-MOFs from TGA curves, appropriate thermal treatment parameters including temperature and treatment time were chosen carefully to avoid the complete collapse of the framework. As expected, all sets of the UiO-66 series have been transformed from microporosity to hierarchical porosity without the loss of crystallinity or porosity (Table 4). By further extending the linker length, a single-crystalline MTV-UiO-67-GH was synthesized through linker exchange. The pore size of UiO-67 was successfully tuned from 1.2 to 15 nm by controlled linker thermolysis. Optical images of UiO-67-GH crystals shown the well-maintained single crystallinity after linker thermolysis, which was extremely difficult to achieve by conventional template-based methods.

Table 4. Porosity parameters of HP-MOFs created by linker thermolysis.

HP-MOF	**S_{BET}† (cm^3g^{-1})**	**D_{Meso}‡ (nm)**	**V(meso)§/V(micro)‖**
HP-UiO-66-AD	1022	9.8	0.83
HP-UiO-66-BD	1012	7.5	0.60
HP-UiO-66-CD	825	7.2	0.82
HP-UiO-66-AE	702	5.5	0.79
HP-UiO-66-AF	571	6.0	1.00
HP-UiO-67-GH	2185	14.8	0.66
HP-MOF-5-AD (Zn)	1736	9.8	0.55
HP-MIL-125-AD (Ti)	1038	2.0, 21	0.28

To further verify the versatility of linker thermolysis, MTV-MOFs with different metal clusters, including MOF-5(Zn), MIL-53(Fe), MIL-125(Ti), and UiO-66(Hf), were also tested. It is evident that the mesopores arose after the thermal treatment as indicated by gas sorption studies. Note that postsynthesis annealing of single-linker MOF-5, companied by the formation of mesopores, has been previously reported by Gadipelli et al.[80] However, controlled linker thermolysis in MTV-MOFs could achieve better tunability on both the amount and the distribution of mesopores by selectively removing thermolabile linkers, whose distribution could be tuned by controlling synthetic conditions.

Realizing the arrangement of various functional groups within MTV-MOFs was found to be critical for understanding the formation of hierarchically porous structures. Inspection of the possible models of linker apportionment would help us gain better insight into the mesoscale mechanism of nanodomain defect formation. Theoretically, when two linkers are mixed to form an MTV-MOF, the nondominant linker is considered to disperse in a matrix formed by the dominant linker, leading to domains with different sizes. Four scenarios of MTV-MOFs are categorized based on the size of domain: (a) Large Domain, (b) Small Domain, (c) Random and (d) Ordered model with no domain formed (Scheme 7).[23] Linker thermolysis proceeds through the decarboxylation process, which enables us to selectively remove the thermolabile linkers inside frameworks. This leads to the formation of defects, whose distribution is almost identical to that of the untreated linkers. Further analysis of the defect distribution through porosity measurements and imaging techniques would enable us to deduce the original linker distribution. Conversely, by controlling the linker distribution through tuning synthetic conditions, a series of HP-MOFs with a variety of defect distributions and defect domain sizes could be constructed. From this perspective, in order to prepare HP-MOFs through linker thermolysis, the linker arrangement must follow the domain distribution models (a) and (b).

To further support the foregoing hypothesis, three typical examples of MTV-MOFs were investigated in order to show the relationship between linker distribution and vacancy apportionment. UiO-66-NH_2-26% prepared from one-pot synthesis exhibits a small-domain linker distribution throughout the framework. After linker thermolysis, mesopores from 2 to 20 nm began to arise due to the decomposition of thermolabile linkers. As indicated from TEM, the mesopores are well dispersed inside each particle. It also shows similar distribution from particle to particle. These defect apportionment information gives us a reflection about how BDC-NH_2 is dispersed within the matrix formed by BDC in the original MTV-UiO-66. In contrast, PCN-700-BDC-NH_2, where BDC-NH_2 was orderly distributed inside MOF frameworks through linker installation[28-29], displays no formation of mesopores after linker thermolysis due to the ordered distribution of the thermolabile linkers. This is consistent with our previous conclusion that only missing linker vacancies would not result in the formation of mesopores, while missing cluster accompanied by pore propagation would be the reason for the formation of mesopores.[81] Another example, MTV-UiO-66-TCPP (TCPP = tetrakis(4-carboxyphenyl)porphyrin), reported by us recently[82], was shown to maintain evenly mixed linker distribution as indicated from SEM-EDS mapping. After linker thermolysis, TCPP was completely removed from the framework and mesopores from 2-4 nm arose, ruling out the possibility of domain formation inside MTV-UiO-66-TCPP.

Overall, the analysis of linker distribution from vacancy apportionment in MTV-MOFs is analogous to the analysis of basic unit (amino acid/nucleotide unit) sequencing in multivariate biosystem (peptides/DNA). On one hand, the complicated assembly process from multiple linkers with various functional groups to a uniform framework is similar to that of protein or DNA from a limited number of amino acids or nucleotides, respectively. On the other hand, selective removal of the functionalized linkers from the MTV-MOFs through thermolysis is analogous to the selective removal of terminal amino acids from peptides through Edman degradation, or the selective breakage of chemically labelled sites along DNA chains through Maxam–Gilbert sequencing. The conceptual similarity among MTV-MOFs, peptides and DNA provides an inspiring solution for analysing the unit distribution by utilizing the relationship between the integrated multivariate systems and the selectively removable individual parts.

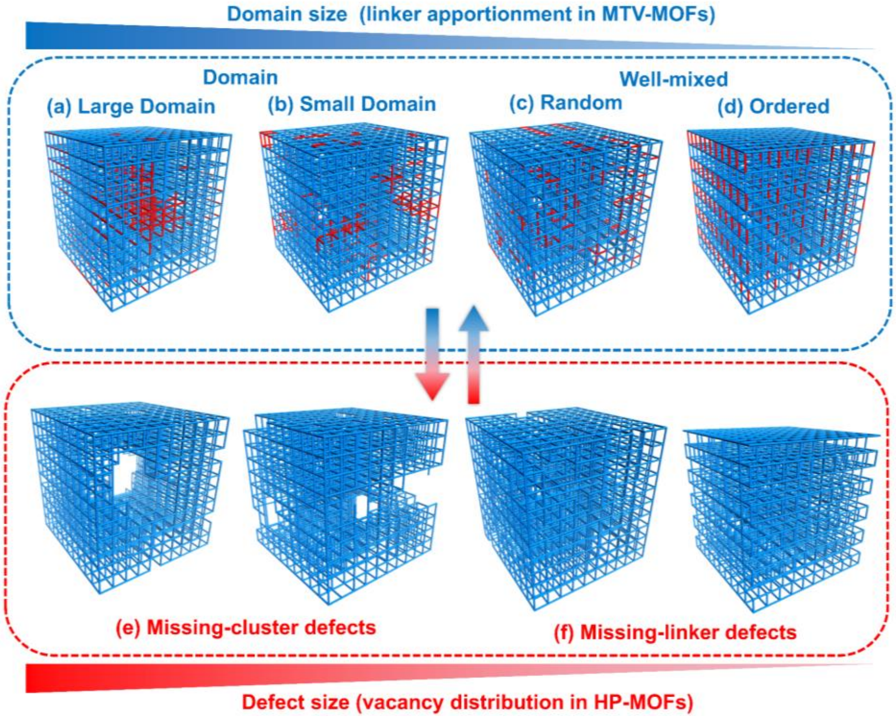

Scheme 7. Relationship between linker spatial apportionment in MTV-MOFs and vacancy spatial distribution in HP-MOFs.

3.4 Conclusion

In conclusion, we report a general approach, linker thermolysis, to construct ultrastable hierarchically porous structures from a series of MTV-MOFs. The thermolabile linker in the frameworks can be removed selectively through a decarboxylation process, leading to the formation of ultra-small MO@HP-MOF composites. The pore sizes can be tuned from 0.8 to 15 nm by controlling the temperature of thermolysis, time of heating, and ratio of thermolabile linker. The relationship between linker distribution in MTV-MOFs and vacancy apportionment in

HP-MOFs was further explored. A domain linker distribution inside MTV-MOF structures plays a pivotal role to create mesopores from a microporous framework. The resulting MO@HP-MOFs exhibited enhanced adsorption properties and catalytic performances. This work not only offers a synthetic approach toward hierarchically porous structures, but also opens a door to a tunable catalytic platform for various MO@HP-MOF composites. Most importantly, linker thermolysis provides a unique tool for deciphering unit distribution in multivariate systems, mimicking biological methods by selectively removing individual parts from integrated multivariate systems.

CHAPTER IV

DYNAMIC BEHAVIORS IN HIERARCHICALLY POROUS MOFS[*]

4.1 Introduction

Design and synthesis of highly porous MOFs with large pore sizes have attracted significant interest during the past two decades.[7-8, 10, 13, 33, 46, 48, 83] The nanoscale voids inside porous materials enable small molecules such as gases and even large molecules such as proteins and enzymes to be trapped and transported.[9, 84] In order to expand the pore sizes of MOFs, several techniques have been developed, but none more applicable than isoreticular expansion.[13, 18] For example, the isoreticular MOF-74 series was obtained by liner elongation, leading to the expansion of pore sizes from 1.4 nm to 9.8 nm.[85] However, large-pore MOFs are not always preferred when longer linkers are applied in a solvothermal synthesis. In many cases, the reaction between clusters and elongated linkers often results in interpenetrated structures or undesired topologies, which in turn reduces the pore sizes of the obtained MOFs. Over the years, many different methods were attempted in order to control the structure and topology of MOFs by designing non-interpenetrated networks or using templates.[86] One successful example is a stepwise linker exchange strategy, in which the short linkers of small-pore MOFs are replaced by progressively longer ones via postsynthetic linker exchange. Eventually, the

---

[*] This chapter is reproduced with permission from Feng, L.; Yuan, S.; Qin, J.-S.; Wang, Y.; Kirchon, A.; Qiu, D.; Cheng, L.; Madrahimov, S.; Zhou, H.-C., Lattice Expansion and Contraction in Metal-Organic Frameworks by Sequential Linker Reinstallation, *Matter*, **2019**, 1, 156-167, Copyright 2019 by Elsevier Inc.

cavity of MOFs was expanded while the topology and non-interpenetrated network was maintained. This method was proven effective for Zn-based MOFs including bio-MOF-100 and a series of layer-pillared structures.[87-89]

Although successful, the application of stepwise linker exchange is limited to low valent metal-based MOFs, in which the M(II)-carboxylate coordination bonds are relatively labile. However, the high valent metal based MOFs are not able to undergo the exchange process of longer linkers due to the strong M(III/IV)-carboxylate bonds and rigid framework structures.[6] To date, controlling interpenetration of high valent metal based MOFs, such as Zr(IV), has yet to be explored. For instance, linker elongation of Zr-MOFs with the UiO (University of Oslo) structure often results in interpenetrated structures, known as porous interpenetrated zirconium–organic frameworks (PIZOF).[71, 90-91] The interpenetrated Zr-MOFs yield smaller cavities and more densely packed framework fragments, which are expected to be thermodynamically more favorable than the non-interpenetrated ones. Therefore, a one-pot synthesis typically ends up with interpenetrated framework structures as the thermodynamic products, while post-synthetic methods are considered to be favorable over one-pot syntheses when preparing non-interpenetrated structures. Ideally, non-interpenetrated Zr-MOFs with short linkers could be used as templates for linker exchange with longer linkers allowing for highly porous Zr-MOFs as kinetic products to be isolated by circumventing the undesirable thermodynamic sink in a one-pot reactions.

However, direct linker exchange of UiO-type MOFs by slightly longer linkers was proven unsuccessful due to extremely low linker exchange rates. The slow linker exchange rate within UiO-type MOFs is attributed to the kinetic barrier caused by the stable Zr(IV)-carboxylate bonds and the rigid framework.[92] We proposed that the kinetic barrier of linker exchange can be overcome by first destabilizing the parent Zr-MOFs. By labilizing and removing the original linkers, secondary linkers with different lengths can be subsequently reinstalled into the unsaturated coordination sites. Herein, we demonstrate that the exchange of Zr-MOFs with linkers of different lengths can be achieved by sequential linker labilization and reinstallation. A stable, non-interpenetrated Zr-MOF was initially synthesized as a template. Subsequently, labile linkers with imine bonds were post-synthetically introduced into the structure to destabilize the Zr-MOF, followed by the progressive dissociation and removal of imine-based linker, which allows for the continuous incorporation of secondary linkers with different lengths. This method enables pore expansion and contraction by reinstalling longer or shorter linkers (Scheme 8), giving rise to a series of non-interpenetrated isoreticular Zr-MOFs.

4.2 Experimental Section

Materials and Instrumentation

All reagents and solvents were commercially available and used as received. PXRD was carried out with a Bruker D8-Focus Bragg-Brentano X-ray Powder Diffractometer equipped with a Cu sealed tube (λ = 1.54178 Å) at 40 kV and 40 mA. NMR data were collected on an Inova 500 spectrometer. The UV-vis absorption spectra were recorded on a Shimadzu UV-2450 spectrophotometer. ICP-MS data were collected with a Perkin Elmer NexION® 300D ICP-MS. TGA was conducted on a TGA-50 (SHIMADZU) thermogravimetric analyzer. Gas sorption measurements were conducted using a Micromeritics ASAP 2020 system. Prior to gas sorption measurements, about 50 mg MOF materials were washed thoroughly with DMF, and exchanged with acetone for two days, during which the solvent was decanted and freshly replenished three times every day. The solvent was then removed under vacuum at 100°C for 12 h, yielding porous material. For UiO-69, PCN-162 and PCN-164-inter, a two-step exchange procedure was carried out.[93] About 50 mg MOF materials were washed thoroughly with DMF and exchanged with CH_2Cl_2 (3 × 20 mL) and n-hexane (3 × 20 mL), during which the solvent was decanted and freshly replenished three times every hour. The solvent was then removed under vacuum at 100°C for 12 h, yielding porous material.

Ligand Synthesis

Synthesis of L2’. In separate beakers, hydrazine (0.16 g, 5 mmol) and 4-formylbenzoic acid (1.5 g, 10 mmol) were dissolved respectively in 50 mL methanol. The solutions were mixed in a 500 mL flask and refluxed for 3 h under continuous stir. After cooling to room temperature, the precipitates were collected by filtration and washed with methanol (1.4 g, yield: 94%). ^{1}H-NMR (500 MHz, DMSO-d_6) δ 8.80 (s, 2H), 8.06 (d, 4H), 8.00 (d, 4H).

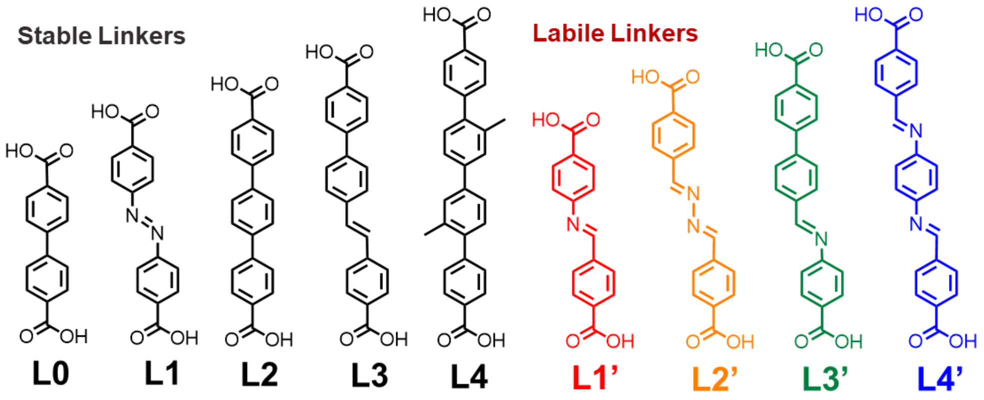

Scheme 8. Stable (L0-L4) and labile linkers (L1’-L4’) used in this work.

Synthesis of L3’. In separate beakers, 4-amino benzoic acid (1.4 g, 10 mmol) and 4'-formyl-[1,1'-biphenyl]-4-carboxylic acid (2.3 g, 10 mmol) were dissolved respectively in 50 mL methanol. The solutions were mixed in a 500 mL flask and refluxed for 3 h under continuous stir. After cooling to room temperature, the precipitates were collected by filtration and washed with methanol (2.9 g, yield: 83%). ^{1}H-NMR (500 MHz, DMSO-d_6) δ 8.71 (s, 1H), 8.06 (q, 4H), 8.00 (d, 2H), 7.91 (q, 4H), 7.35 (d, 2H).

Synthesis of L4’. In separate beakers, p-phenylenediamine (0.5 g, 5 mmol) and 4-formylbenzoic acid (1.5 g, 10 mmol) were dissolved respectively in 50 mL methanol. The solutions were mixed in a 500 mL flask and refluxed for 3 h under continuous stir. After cooling to room temperature, the precipitates were collected by filtration and washed with methanol (1.6 g, yield: 86%). ^{1}H-NMR (500 MHz, DMSO-d_6) δ 8.82 (s, 2H), 8.09 (d, 8H), 7.45 (d, 4H).

MOF Synthesis

Synthesis of UiO-67.5 or PCN-160. $ZrCl_4$ (200 mg), L1 (100 mg), trifluoroacetic acid (1.0 mL) and DMF (20 mL) were charged in a Pyrex vial. The mixture was heated in 120 °C oven for 72 h. After cooling down to room temperature, the red crystals were harvested.

Synthesis of PCN-161. PCN-161 was synthesized by repeatedly linker exchange of PCN-160 with L1' DMF solution. Generally, crystals of PCN-160 (100 mg) were incubated with the solution of L1' in DMF (80 mM, 20 mL) at 85°C for 24 h. The supernatant was replaced with fresh solution of L1' in DMF (80 mM, 20 mL) every 6 h.

Synthesis of UiO-68. UiO-68 was synthesized by repeatedly linker reinstallation of PCN-161 with L2 DMF solution. Generally, crystals of PCN-161 (100 mg) were incubated with the solution of L2 in DMF (80 mM, 20 mL) at 85°C for 48 h. The supernatant was replaced with fresh solution of L2 in DMF (80 mM, 20 mL) every 12 h.

Synthesis of UiO-67. UiO-67 was synthesized by repeatedly linker reinstallation of PCN-161 with L0 DMF solution. Generally, crystals of PCN-161 (100 mg) were incubated with the solution of L0 in DMF (80 mM, 20 mL) at 85°C for 48 h. The supernatant was replaced with fresh solution of L0 in DMF (80 mM, 20 mL) every 12 h.

Synthesis of PCN-162. PCN-162 could be synthesized through two routes. (1) PCN-162 was synthesized by repeatedly linker exchange of UiO-68 with L2' DMF solution. Generally, crystals of UiO-68 (100 mg) were incubated with the solution of L2' in DMF (80 mM, 20 mL) at 85°C for 24 h. The supernatant was replaced with fresh solution of L2' in DMF (80 mM, 20 mL) every 6 h. (2) PCN-162 could also be obtained by directly linker reinstallation with PCN-161. Generally, crystals of PCN-161 (100 mg) were incubated with the solution of L2’ in DMF (80 mM, 20 mL) at 85 °C for 48 h. The supernatant was replaced with fresh solution of L2’ in DMF (80 mM, 20 mL) every 12 h.

Synthesis of PCN-163. PCN-163 was synthesized by repeatedly linker reinstallation of PCN-162 with L3’ DMSO solution. Generally, crystals of PCN-162 (100 mg) were incubated with the solution of L3’ in DMSO (80 mM, 20 mL) at 85°C for 72 h. The supernatant was replaced with fresh solution of L3’ in DMSO (80 mM, 20 mL) every 12 h. DMSO is chosen as reinstallation solution because L3’ shows better solubility in DMSO than in DMF or DEF.

Synthesis of PCN-164. PCN-164 was synthesized by repeatedly linker reinstallation of PCN-163 with L4’ DMF solution. Generally, crystals of PCN-163 (20 mg) were incubated with the solution of L4’ in DMF (80 mM, 20 mL) at 85°C for 72 h. The supernatant was replaced with fresh solution of L4’ in DMF (80 mM, 20 mL) every 12 h.

Synthesis of UiO-69. UiO-69 was synthesized by repeatedly linker exchange of PCN-164 with L4 DMF solution. Generally, crystals of PCN-164 (100 mg) were incubated with the solution of L4 in DMF (80 mM, 20 mL) at 85°C for 72 h. The supernatant was replaced with fresh solution of L4 in DMF (80 mM, 20 mL) every 12 h.

Synthesis of PCN-163-inter. PCN-163-inter was synthesized through one-pot reaction. $ZrCl_4$ (20 mg), L3’ (200 mg), benzoic acid (100 mg) and DMF (2 mL) were charged in a Pyrex vial. The mixture was heated in 120 °C oven for 48 h. After cooling down to room temperature, the microcrystalline crystals were harvested.

Synthesis of PCN-164-inter. PCN-163-inter was synthesized through one-pot reaction. $ZrCl_4$ (20 mg), L4' (200 mg), benzoic acid (100 mg) and DMF (2 mL) were charged in a Pyrex vial. The mixture was heated in 120 °C oven for 48 h. After cooling down to room temperature, the microcrystalline crystals were harvested.

Synthesis of UiO-69-inter. UiO-69-inter was synthesized through one-pot reaction. $ZrCl_4$ (20 mg), L4 (20 mg), benzoic acid (200 mg) and DMF (2 mL) were charged in a Pyrex vial. The mixture was heated in 120 °C oven for 48 h. After cooling down to room temperature, the microcrystalline crystals were harvested.

Single Crystal X-Ray Diffraction

All as-synthesized crystals were taken from the mother liquid without further treatment, transferred to oil, and mounted onto a loop for single crystal X-ray data collection. Diffraction data were measured on a Bruker Smart Apex diffractometer equipped with a Mo-$K\alpha$ microfocus X-ray source (λ = 0.71073 Å) and Cu-$K\alpha$ microfocus X-ray source (λ = 1.54184 Å) and a low temperature device (100 K). The data frames were recorded using the program APEX2 and processed using the program *SAINT* routine within APEX2.[5] The data were corrected for absorption and beam corrections based on the multi-scan technique as implemented in *SADABS*. The structures were solved by direct method using *SHELXS* and refined by full-matrix least-squares on F^2 using *SHELXL* software.[6] The contribution of disordered solvent molecules was treated as diffuse using SQUEEZE procedure implemented in PLATON.[7] The diffraction of some MOF crystals can be weak because of the large unit cell, disordered atom and solvents (**Table 5**).[8]

Table 5. Crystal data and structure refinements of PCN-16X and UiO-6X.

	PCN-161	**PCN-162**	**PCN-164-inter**
Formula	$C_{180}H_{108}N_{12}O_{64}Zr_{12}$	$C_{48}H_{30}N_6O_{16}Zr_3$	$C_{66}H_{42}N_6O_{16}Zr_3$
Formula weight	4557.42	1220.44	1448.72
Color/Shape	Light Yellow	Light Yellow	Yellow
Crystal system	Cubic	Cubic	Cubic
Space group	*Fm-3m*	*Pn-3*	*Fd-3m*
a (Å)	29.3907(4)	32.8112(2)	38.4025(5)
b (Å)	29.3907(4)	32.8112(2)	38.4025(5)
c (Å)	29.3907(4)	32.8112(2)	38.4025(5)
α (º)	90.00	90.00	90.00
β (º)	90.00	90.00	90.00
γ (º)	90.00	90.00	90.00
V (Å^3)	25388.1(10)	35323.7(6)	56634(2)
Z	2	8	16
T (K)	100	100	100
Wavelength (Å)	0.71073 (MoK$_\alpha$)	1.54184 (CuK$_\alpha$)	0.71073 (MoK$_\alpha$)
$d_{\text{calcd.}}$ (g/cm^3)	0.596	0.459	0.680
μ(mm^{-1})	0.269	1.611	0.250
F(000)	4528.0	4864.0	11648.0
θ_{max} [deg]	27.480	74.743	26.371
Parameters	30	136	50
Reflections	1502	12116	2744
Completeness	0.998	0.999	0.999
R_1 (all data)	0.1308	0.0914	0.1802
wR_2 (all data)	0.2942	0.2620	0.3575
GOF on F^2	1.740	1.138	1.275

Table 5. Continued

	UiO-67	**UiO-68**
Formula	$C_{42}H_{24}O_{16}Zr_3$	$C_{132}H_{84}O_{32}Zr_6$
Formula weight	1058.27	2729.31
Color/Shape	Colorless	Colorless
Crystal system	Cubic	Cubic
Space group	*Fm-3m*	*Fm-3m*
a (Å)	26.742(3)	32.7670(7)
b (Å)	26.742(3)	32.7670(7)
c (Å)	26.742(3)	32.7670(7)
α (º)	90.00	90.00
β (º)	90.00	90.00
γ (º)	90.00	90.00
V (Å^3)	19124(6)	35181(2)
Z	8	4
T (K)	100	100
Wavelength (Å)	0.71073 (MoK$_\alpha$)	0.40651
$d_{\text{calcd.}}$ (g/cm^3)	0.735	0.515
μ(mm^{-1})	0.353	0.257
F(000)	4192.0	5488.0
$\theta_{\max}$ [deg]	29.580	15.306
Parameters	37	66
Reflections	1399	2034
Completeness	0.982	0.991
R_1 (all data)	0.0434	0.0518
wR_2 (all data)	0.1245	0.1639
GOF on F^2	1.146	1.148

4.3 Results and Discussion

Although the linker exchange of Zr-MOFs has been reported, linkers with the same lengths are often required. Linker exchange of Zr-MOFs with longer linkers has been attempted but to no avail. Considering the strong Zr(IV)-carboxylate bonds and the rigid framework, the linker exchange process needs to overcome a high kinetic barrier. In order to accelerate the linker exchange process, the parent Zr-MOF needs to be destabilized. As shown in Scheme 9, a stable Zr-MOF is labilized by introducing organic linkers that contain labile imine bonds. The creation of missing linker defects by the subsequent removal of imine-linkers introduces flexibility to the rigid framework, which in turn allows for the installation of longer linkers into the defect sites. In other words, the labilized MOF will act as a reaction intermediate, which allows for mild insertion of longer linkers to complete the linker reinstallation process.

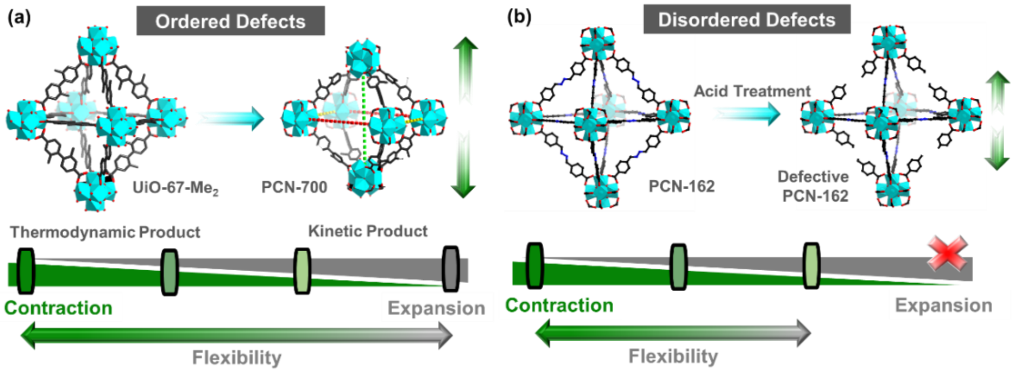

Scheme 9. Introducing labile bonds into robust Zr-MOFs in order to achieve sequential linker reinstallation.

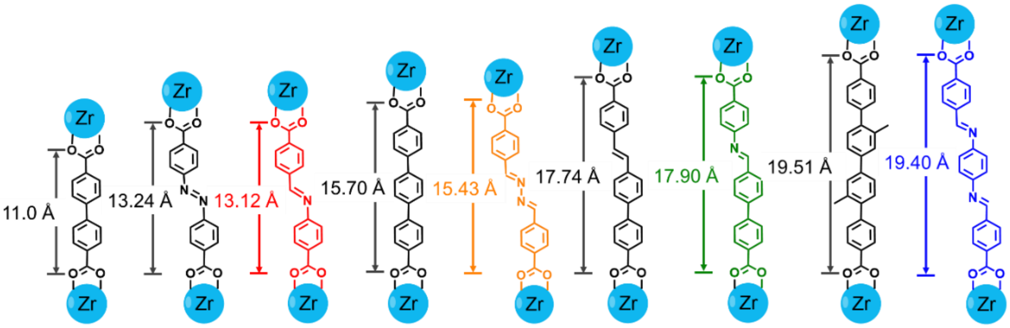

Scheme 10. Lengths of various linkers (L0-L4 and L1’-L4’) used in this work.

To prove our hypothesis, a previously reported Zr-MOF, namely Zr_6-AZDC or UiO-67.5 was chosen as the parent MOF.[94-98] UiO-67.5 is constructed by 12-connected Zr_6 clusters and azobenzene-based linkers (L1, azobenzene-4,4’-dicarboxylic acid). The orange color and distinctive ultraviolet–visible (UV-vis) absorption of azobenzene moieties allows for easy monitoring of the linker exchange process by UV-vis spectroscopy. Initially, direct linker exchange for longer linkers was attempted for UiO-67.5 by incubating the crystal of UiO-67.5 in a *N,N’*-dimethylformamide (DMF) solution containing L2 (terphenyl-4,4"-dicarboxylic acid, 50 mM) at 85°C. The color of the UiO-67.5 crystals as well as the solution was unchanged after 24 h. The PXRD of the sample was also maintained, indicating a failed linker exchange process.

Instead, UiO-67.5 can be labilized by replacing the stable L1 linker with an imine-based linker of identical length (L1’, 4-carboxybenzylidene-4-aminobenzoic acid, Scheme 10). The labilized analogue of UiO-67.5 is denoted as PCN-161. According to the literature, L1' can be dissociated into 4-amino benzoic acid and 4-formylbenzoic acid through hydrolysis by breaking the imine bond to create missing-linker defects (Scheme 9).[99] As expected, the labile imine-linker in PCN-161 can be easily and successfully exchanged by L2 when incubated in the solution of L2/DMF at 85 °C. The linker exchange process was monitored by ^{1}H-NMR spectra. ^{1}H-NMR spectra of digested samples revealed that the L1' were completely replaced by L2 after 24 h. The final product was known as UiO-68 and the corresponding PXRD matched well with the simulations based on single structure of UiO-68.

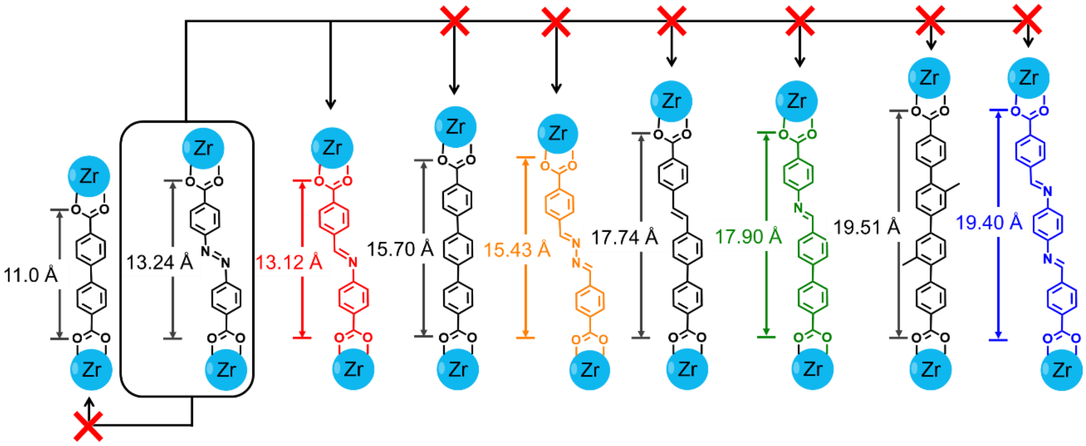

Scheme 11. Scheme of the transformation from UiO-67.5 (PCN-160) to other Zr-MOFs.

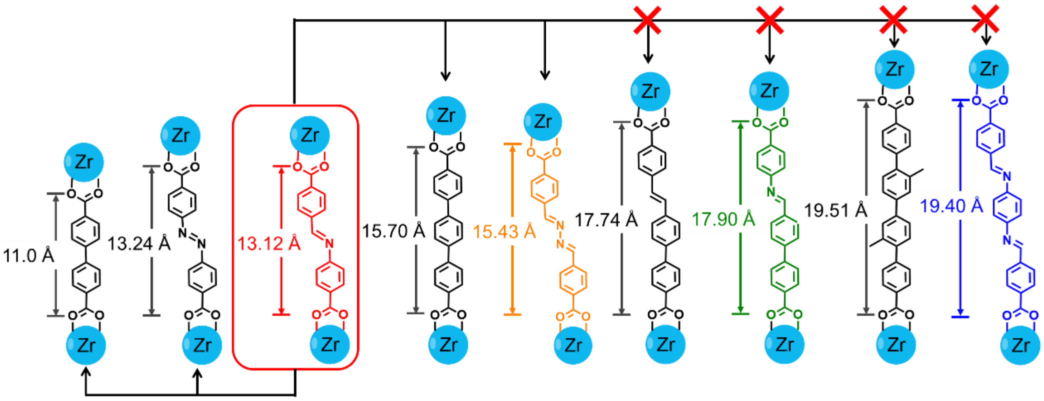

Scheme 12. Scheme of the transformation from PCN-161 to other Zr-MOFs.

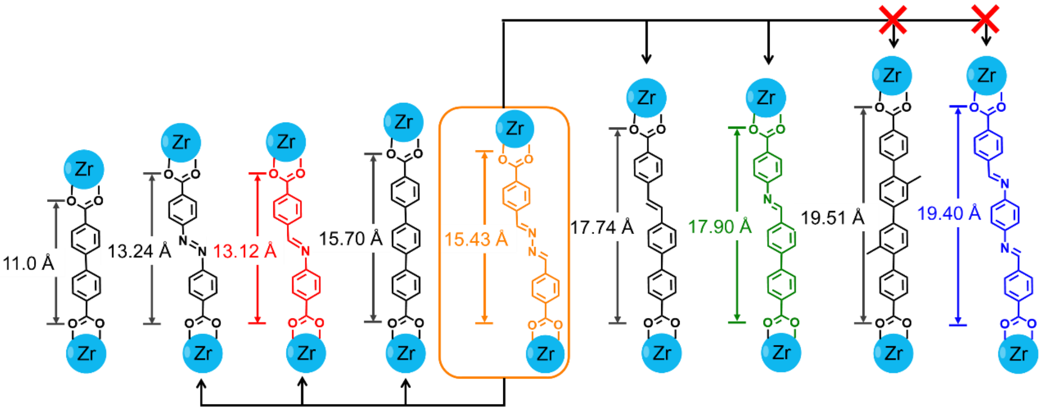

Scheme 13. Scheme of the transformation from PCN-162 to other Zr-MOFs.

Furthermore, the transformation occurred in a single-crystal to single-crystal manner, so that the structure of product can be clearly characterized by single-crystal X-ray diffraction (SCXRD, Table 5). The structures and lattice parameters of the product are consistent with the reported values for UiO-68. The morphology of crystals was unchanged after the linker reinstallation process was performed, although an obvious color change from yellow to colorless was observed (Figure 38). Additionally, the supernatant was analyzed by ICP-MS, which showed no Zr leaching during the linker reinstallation process. All of the evidence clearly shows a single-crystal to single-crystal transformation process occurs without dissolving or destructing the parent framework.

To further examine the possibility of continuously expanding the unit cell dimensions of non-interpenetrated Zr-MOFs, stepwise linker labilization and reinstallation was carried out by iteratively applying linker labilization and reinstallation (Scheme 11-13). A series of stable linkers were selected (L1 to L4) and their imine-based labile analogues with identical lengths were also designed and synthesized (L1’ to L4’, Scheme 8). Sequential linker reinstallation was realized by replacing the short imine-linker with progressively longer ones (Scheme 11-13). For example, PCN-162 was obtained by incubating the crystal of PCN-161 in the solution of L2’. Sequential exchange of PCN-162 with L3’ and L4’ further give rise to PCN-163 and PCN-164. The complete exchange of each step was characterized by ^{1}H-NMR spectra of digested samples. The gradually enlarged unit cell dimensions were clearly reflected by the peak shift in PXRD patterns (Figure 39). The unit cell parameters were determined by PXRD and shown in Table 6.

Single crystal structures of PCN-161 and PCN-162 were successfully obtained, providing direct evidence of linker exchange (Table 5). SCXRD experiments revealed that the PCN-161 crystallizes in cubic space group *Fm-3m*. Each Zr_6-cluster is connected to twelve L1’ linkers, giving rise to a non-interpenetrated framework with **fcu** topology. The L1’ was 4-fold disordered due to the high symmetry. PCN-162 shows the same network structure as PCN-161. However, it crystallizes in the lower symmetry space group *Pn-3*. As a result of the reduce symmetry, the conformation of L2' can be clearly determined. The replacement of L1' by L2' was clearly observed in single crystal structures. The cell-edge length of PCN-162 increased by 2.65 Å compared to that of PCN-161. The unit cell parameters determined by SCXRD matched well with the PXRD results.

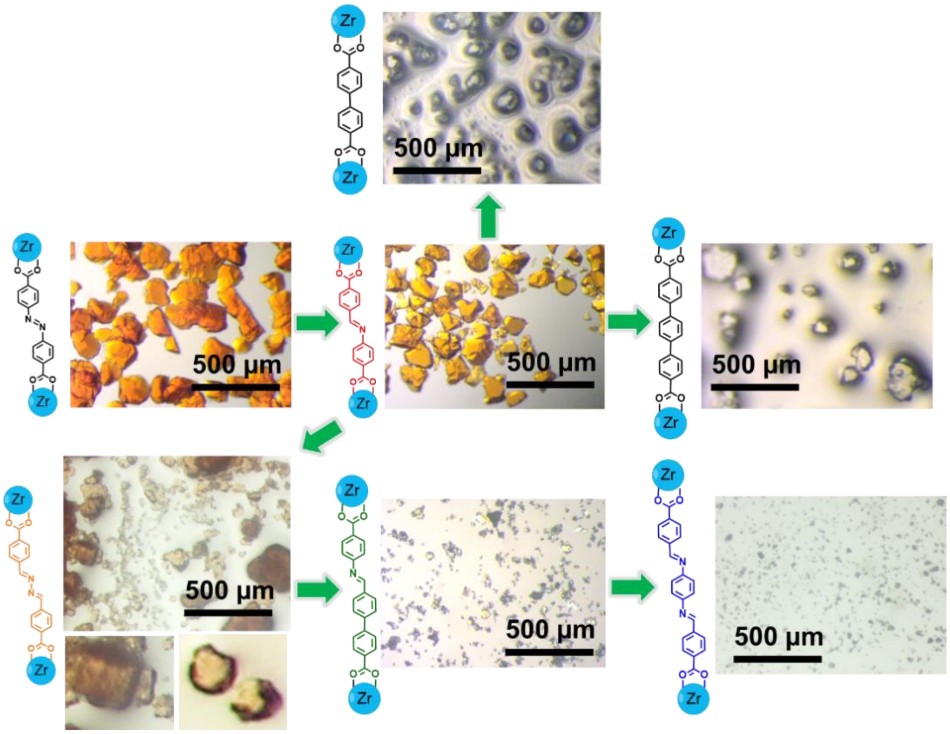

Figure 38. Microscopic images of PCN-16X crystals.

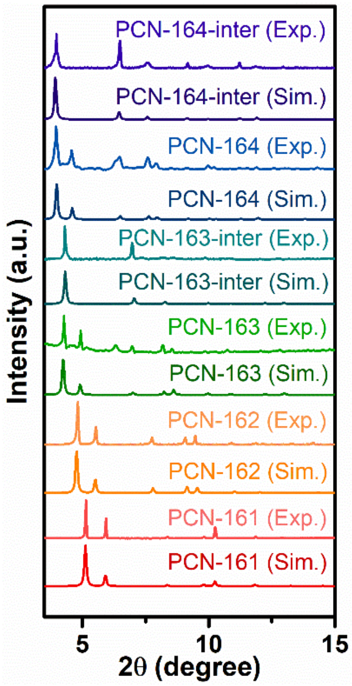

Figure 39. Experimental and simulated PXRD patterns of PCN-16X.

Note that PCN-163 and PCN-164 were obtained with non-interpenetrated structures, which would be extremely difficult to obtain from a one-pot synthesis. In contrast, one-pot synthesis of Zr-MOFs from L3’, L4’ or linkers with similar lengths always generate interpenetrated structures, as indicated by SCXRD and PXRD (Figure 40-42). Single crystal structure of interpenetrated PCN-164 was obtained, denoted as PCN-164-inter. PCN-164-inter crystalizes in the cubic space group *Fd-3m*. It consists of two sets of independent and mutually interpenetrating UiO-type frameworks and similar structures have been previously reported, known as PIZOFs.[71, 90-91] Due to the low solubility of L3’, only microcrystalline powders, denoted as PCN-163-inter, were obtained from one-pot synthesis, and the resulting structural model was built in Materials Studio by isoreticular contraction of PCN-164-inter. Experimental PXRD patterns of PCN-163-inter and PCN-164-inter indicate the absence of the second diffraction peaks, corresponding to the extinction of (200) plane diffraction and this matches well with the simulated PXRD patterns. The sequential linker labilization and reinstallation allows for the isolation of non-interpenetrated structures that are thermodynamic unfavorable during one-pot synthesis.

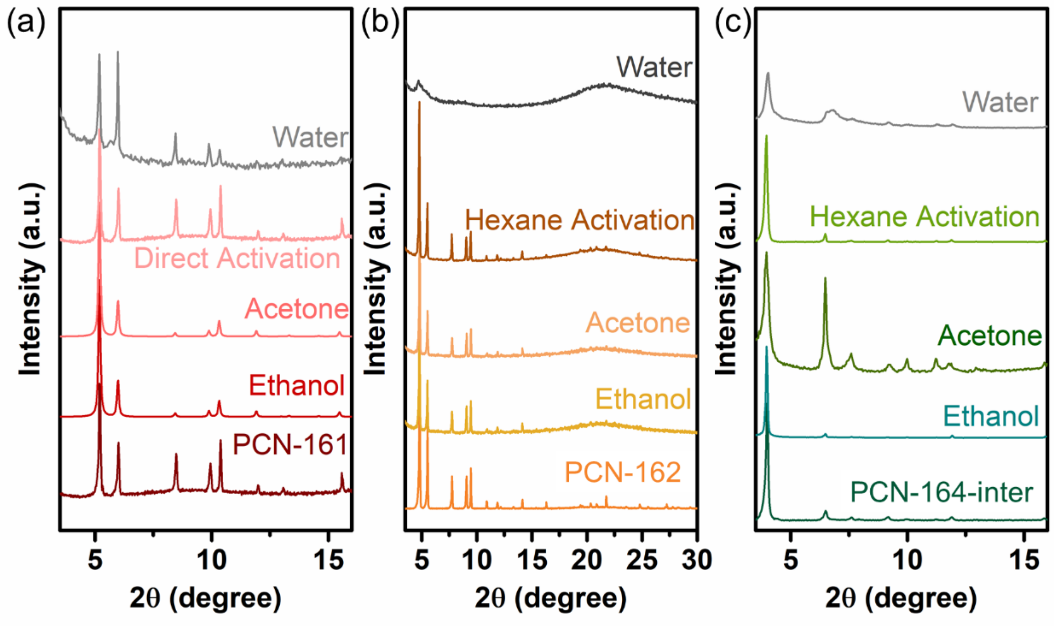

Figure 40. The PXRD patterns of PCN-161, PCN-162 and PCN-164-inter in various solvents and under activation condition.

To further explore the scope of the linker labilization and reinstallation method, the labilized MOFs with imine linkers (i.e. PCN-16X series) were treated with the solutions of linear linkers with different lengths. The products were digested and analyzed by ^{1}H-NMR to verify the linker reinstallation (Figure 43-44). Generally, the labilized MOFs can tolerate a linker difference within approximately 2.50 Å. This distance represents the maximum flexibility of the framework (Scheme 11-13). For example, the imine linker in PCN-161 (L1' 13.12 Å) can be replaced by L0 (biphenyl-4,4'-dicarboxylic acid, 11.00 Å), L1 (13.24 Å), L2 (15.70 Å), and L2' (15.74 Å) through singe crystal to single crystal transformation. However, longer linkers such as L3' (17.90 Å) or L4' (19.40 Å) cannot be accommodated by PCN-161. For comparison, the exchange of stable MOFs (i.e. UiO-6X series) requires the linker length to be identical. This indicates that the labile linkers enhance the flexibility of the framework so that linkers with different lengths can be easily incorporated.

The incorporation of labile imine bonds into the PCN-16X series reduced the chemical and mechanical stability of the framework (Figure 45-46). Although the PCN-16X series are stable in common organic solvents including DMF, methanol, ethanol and acetone, the frameworks are sensitive towards water. PXRD patterns show that PCN-16X partially lost its crystallinity after immersing in water for 24 h. The mechanical stability of PCN-16X series is also compromised, as indicated by the collapsed framework after solvent removal. Indeed, direct activation of PCN-162 from acetone leads to framework collapse as indicated by N_2 sorption isotherms. In order for PCN-162 to retain its porosity, the as-synthesized sample needs to be exchanged with low-surface tension solvents before activation. Following the literature,[93] PCN-162 was exchanged with CH_2Cl_2 and hexane, leading to the successful activation. Additionally, we fail to activate PCN-163 and PCN-164, possibly due to the large pore sizes and labile imine linkers.

Table 6. Unit cell parameters obtained from powder X-ray diffraction.

Unit Cell Parameters	Cell length	Cell Angle
UiO-67	a = b = c = 26.74 Å	α = β = γ = 90º
UiO-67.5	a = b = c = 29.86 Å	α = β = γ = 90º
UiO-68	a = b = c = 32.77 Å	α = β = γ = 90º
UiO-69	a = b = c = 38.55 Å	α = β = γ = 90º
UiO-69-inter	a = b = c = 38.40 Å	α = β = γ = 90º
PCN-161	a = b = c = 29.39 Å	α = β = γ = 90º
PCN-162	a = b = c = 32.81 Å	α = β = γ = 90º
PCN-163	a = b = c = 35.08 Å	α = β = γ = 90º
PCN-163-inter	a = b = c = 34.96 Å	α = β = γ = 90º
PCN-164	a = b = c = 38.56 Å	α = β = γ = 90º
PCN-164-inter	a = b = c = 38.40 Å	α = β = γ = 90º

The stability of PCN-16X series can be enhanced by replacing the labile imine linkers with stable ones. The resulting materials, known as the UiO series, display good chemical stability in water as indicated by PXRD patterns. Furthermore, the UiO series can be directly activated without losing any crystallinity or porosity (Table 7). N_2 sorption isotherms at 77 K shows progressively elevated N_2 total uptakes, which is in line with the change of unit cell dimensions. The pore sizes distribution derived from adsorption isotherms further indicates the gradual increase of pore sizes from 1.5 nm to 2.2 nm. These data further verified the non-interpenetrated structure obtained by sequential linker labilization and reinstallation. The density change of the samples was also studied during the linker exchange process. The height of the samples inside an NMR tube increased from 0.51 cm to 0.68 cm (PCN-162, pale yellow) after linker reinstallation. Furthermore, the density difference between PCN-161 and PCN-162 can be directly observed during the exchange process, as the lighter PCN-162 layer lies above the heavier PCN-161.

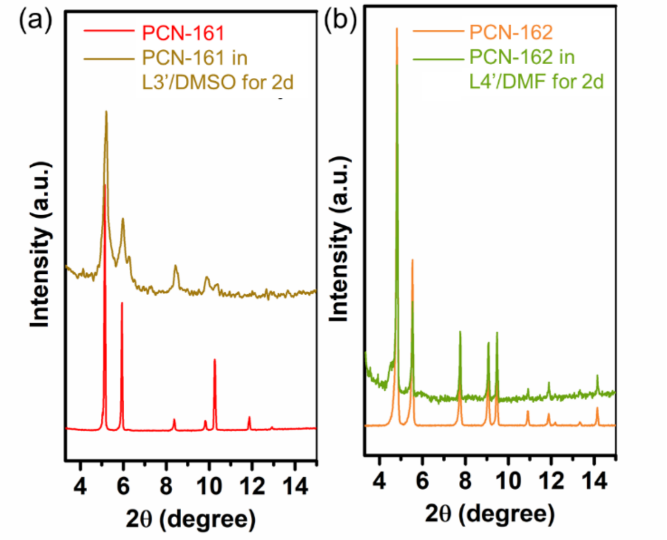

Figure 41. (a) The PXRD patterns of PCN-161 before and after soaking in L3’ solution; (b) The PXRD patterns of PCN-162 before and after soaking in L4’ solution.

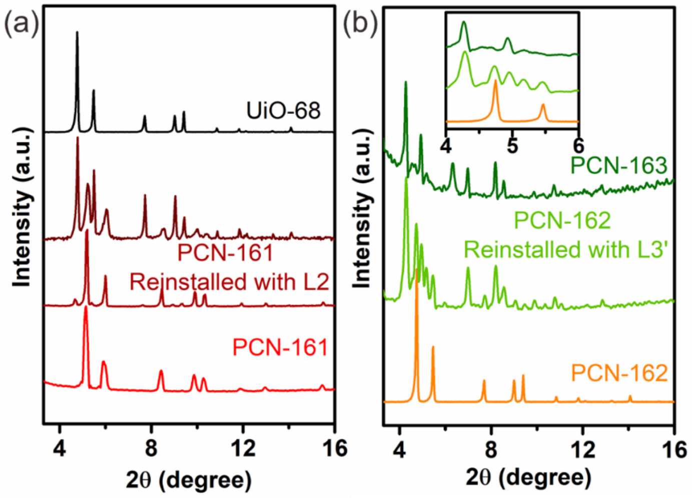

Figure 42. (a) The PXRD patterns of PCN-161 before and after soaking in L2 solution at 85°C as a function of time periods; (b) The PXRD patterns of PCN-162 before and after soaking in L3’ solution at 85°C as a function of time periods.

We proposed that labile CBAB linker is partially dissociated and removed during acid treatment to generate terminal ligands. Most likely, these terminal ligands would be replaced by TPDC linkers to compensate for the charge loss. The exchange ratio in MOFs were confirmed by the ^{1}H-NMR results of digested samples. For ^{1}H NMR spectroscopy, the dry samples (around 5 mg) were dissolved in about 1 mL 5% D_2SO_4/DMSO-d_6. The CBAB was decomposed into 4-amino benzoic acid and 4-formylbenzoic acid under acetic condition. Therefore, the exchange ratio was calculated by the integration of H from TPDC and 4-formylbenzoic acid.

The conventional linker exchange process relies on the reversible dissociation/association of coordination bonds. In contrast, sequential linker labilization and reinstallation takes advantage of the dynamic covalent bonds as well. The dynamic imine bond in the PCN-16X series not only facilitates linker the exchange process, but also provides additional opportunities to introduce new functional groups into MOFs. Reactions based on imine bonds have been well developed in organic chemistry, which is an essential component in dynamic covalent chemistry.[100-102] We show that the reversible dissociation/association of the imine bonds in PCN-164 enables the substitution of phenylenediamine fragments. The linker-fragment exchange was carried out by immersing PCN-164 crystals in the solution of substitute diamines at 85 °C for 24 h. PXRD measurements showed that the crystallinity was maintained after fragment exchange. ^{1}H-NMR of the digested samples further verifies the exchange with the diamine fragment. The substituents on the diamine fragment can affect the basicity of the resulting imine moieties, which in turn alters the pore environment of PCN-164. As a proof of concept, the catalytic activity of functionalized PCN-164 was tested in Knoevenagel condensation reactions. The Knoevenagel condensation reaction is a model of C-C bond-forming reactions catalyzed using basic conditions. It also plays an important role in the synthesis of organic intermediate such as coumarins and their derivatives.[103-105] Among functionalized PCN-164 samples, the diaminocyclohexane modified sample shows the highest activity due to the enhanced basicity of the imine sites. Substrates with various functional groups (-H, -Me, $-NO_2$ and -OH) were converted to their corresponding products in substantial conversion percentages. Furthermore, the catalytic activity of the MOF catalyst was well maintained after three catalytic cycles. Our postsynthetic approach brings new opportunities into the preparation of high-crystalline M(IV) based MOFs combining the reversible formation of imine bonds during postsynthetic process. Considering the diversity of both MOFs and dynamic covalent chemistry, a large family of MOFs with various metal clusters and dynamic linkers can be expected. This work also provides a route to activate the inert framework using dynamic covalent chemistry, which can be potentially applied to a variety of materials including supramolecular cages and COFs.

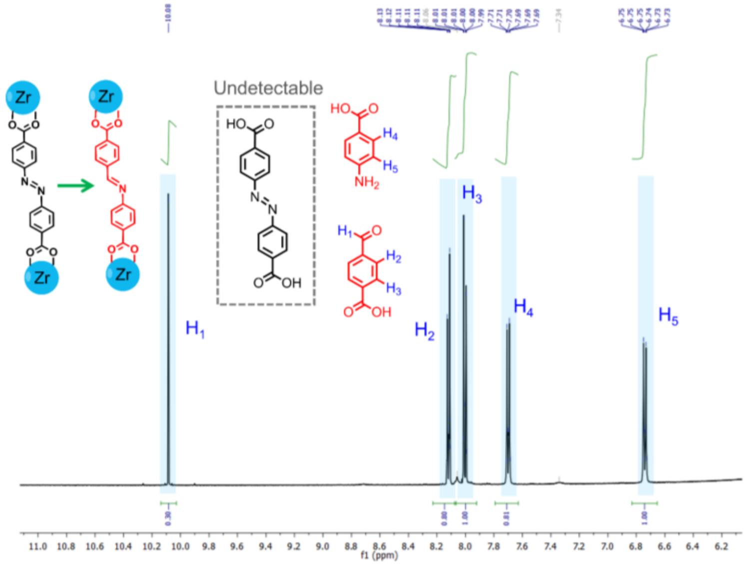

Figure 43. ^{1}H-NMR spectrum of digested PCN-161 showing complete conversion from UiO-67.5 (PCN-160) to PCN-161.

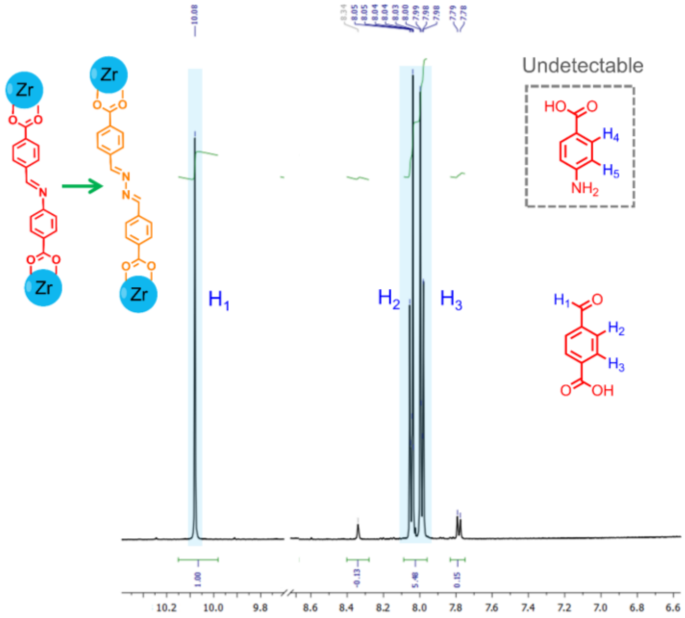

Figure 44. ^{1}H-NMR spectrum of digested PCN-162 showing complete conversion from PCN-161 to PCN-162.

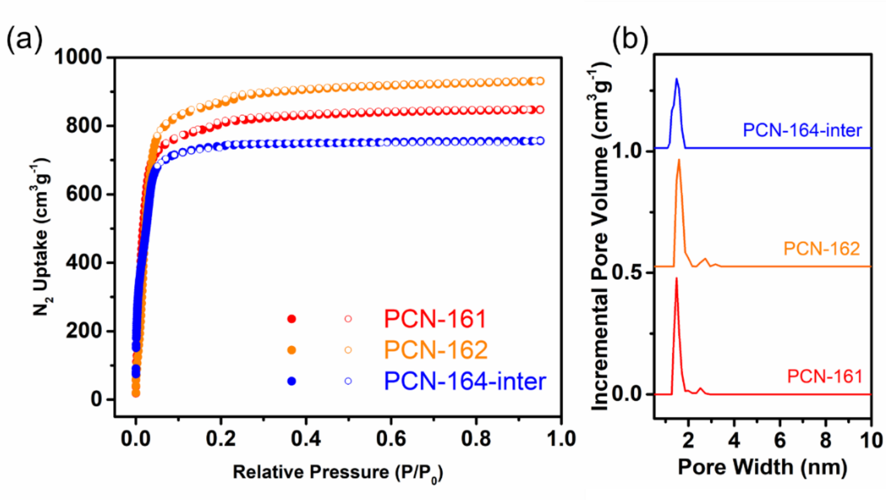

Figure 45. N$_2$ sorption isotherms and pore size distributions of PCN-161, PCN-162 and PCN-164-inter.

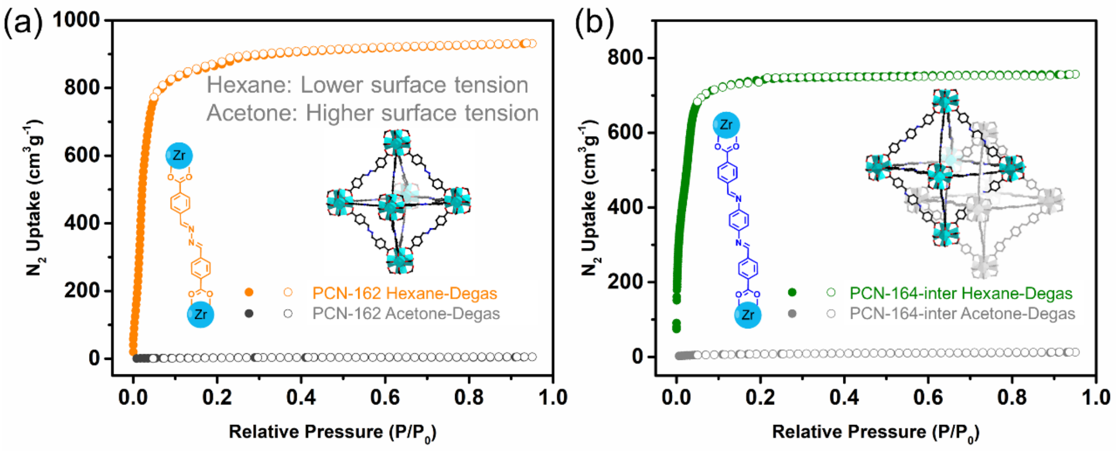

Figure 46. Successful activation of PCN-162 and PCN-164-inter through hexane with low surface tension.

Table 7. Pore features of UiO-6X materials prepared by linker reinstallation.

Entry	Samples	$S_{BET}{}^{a}$ (m^2g^{-1})	$V_t{}^{b}$ (cm^3g^{-1})
1	**UiO-67**	2245	0.86
2	**UiO-67.5**	2759	1.21
3	**UiO-68**	3301	1.45
4	**UiO-69**	3809	1.63
5	**UiO-69-inter**	2831	1.23

$S_{BET}{}^{a}$: Brunauer-Emmett-Teller (BET) specific surface area; $V_t{}^{b}$: total specific pore volume determined by using the adsorption branch of the N_2 isotherm at $P/P_0 = 0.95$.

4.4 Conclusion

In conclusion, we report the sequential linker labilization and reinstallation as a powerful tool to tailor pore environments and control interpenetration of isoreticular MOFs. Continuous expansion (or contraction) of unit cell dimensions of Zr-MOFs was realized by installing progressively longer (or shorter) linkers into the labilized parent framework. This method not only allows the construction of non-interpenetrated Zr-MOFs with large pore size, but also facilities the functionalization of pore environments by modifying the imine-bonds. Furthermore, the idea of utilizing dynamic covalent chemistry to manipulate the properties of MOFs shall lead to new discoveries in the field of MOFs and beyond.

CHAPTER V

ENGINEERING HIERARCHY AND HETERARCHY IN MOF@MOF COMPOSITES*

5.1 Introduction

The precise location engineering of building units in proteins and nucleic acids is essential for chemical processes in cells such as recognition, bio-catalysis, and information storage. These well-defined sequences and distributions have inspired researchers to develop tailored architectures with controllable heterogeneity in polymers, nanomaterials and porous materials.[106-108] For example, recent work on bimetallic nanoparticles synthesized through surface inorganometallic chemistry demonstrated enhanced catalytic performance due to the synergistic effect between constituent metals.[109] Precise molecular encoding on multi-component polymers has also made a substantial influence on their macroscopic properties.[5, 110-111]

MTV-MOFs constructed from multiple metal clusters and linkers promise fascinating advances in fields such as gas separation, size-selective catalysis, and controlled drug delivery.[7-9, 11, 14-16, 112-114] Among these MOFs, MTV-MOF-5, developed by Yaghi and coworkers, contains up to eight different functionalities in a disordered arrangement in an overall ordered backbone framework.[32] Furthermore, we have

---

* This chapter is reproduced with permission from Feng, L.; Yuan, S.; Li, J.-L.; Wang, K.-Y.; Gregory, D.; Zhang, P.; Wang, Y.; Zhou, H.-C., Uncovering Two Principles of Multivariate Hierarchical Metal-Organic Framework Synthesis via Retrosynthetic Design, *ACS Cent. Sci.* **2018**, 4, 12, 1719-1726, Copyright 2018, The Authors; published by the American Chemical Society.

demonstrated that the installation of linear linkers and inorganic clusters in coordinatively unsaturated MOFs can post-synthetically arrange functionalities into predicted positions.[28-29, 115] Alternatively, the construction of hierarchical MTV-MOFs from multiple components is considered a viable pathway for achieving advanced applications that require sophisticated architectures.[33, 103, 116-120] However, the growing gap between the design and synthesis of hierarchical MOFs has become a critical limitation mainly because lattice matching (similar crystallographic parameters) has typically been required for the epitaxial growth method (EGM) necessary to achieve hierarchical MOF-on-MOF hybrids growth. Yet, as most MOFs have distinct crystallographic parameters, EGM has been severely limited in applicability. A recently developed method by Kitagawa and coworkers involves the introduction of a polymer to connect the two different MOF phases with varying crystallographic parameters into one unified composite.[121] However, this method cannot achieve full coverage of the core-MOFs with the shell-MOFs necessary for size selective applications. Besides, the introduction of the polymer into the interface between the lattice mismatched core and shell-MOFs can potentially undermine the intricate MOF-MOF interface, which often includes defect sites and coordinatively unsaturated metal sites. Recently, our group reported a one-step synthesis of hybrid core–shell MOFs with mismatched lattices under the guidance of nucleation kinetic analysis.[122] Yet, the versatility of this one-pot nucleation kinetic control strategy is limited because it is challenging to generate clusters with different metal species under one-pot synthetic conditions. Thus, the development of a novel and facile method for the rational design and synthesis of hierarchical MOFs without additives, while still being able to overcome the restrictions of the lattice matching rule, is quite urgent.

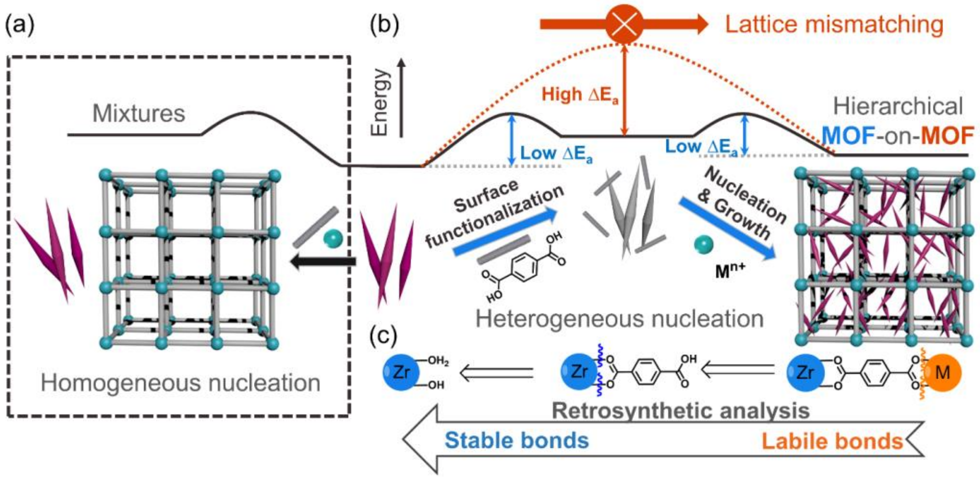

Scheme 14. Preparation of multivariate hierarchical metal-organic frameworks through retrosynthetic design.

In this work, we report two principles for preparing hierarchical MOFs with mismatched lattices through retrosynthetic design: surface functionalization and retrosynthetic stability considerations[115, 123]. Retrosynthetic analysis has been mainly utilized in the synthesis of organic molecules based on covalent bonds by transformation of a target molecule into simpler precursors and sequential assembly through a set of known chemical reactions. We believe that the conceptual scope of retrosynthetic analysis can be extended to coordination bond based complicate systems, for example, MTV hierarchical MOFs (Scheme 14). Retrosynthetically assembled metal precursors and ligands, placed inside the designed MOF structures with intrinsic defects, can lead to sophisticated structures by utilizing kinetic control and post-synthetic modifications. [124-125] Similarly, the kinetically controlled synthesis of hierarchical MOFs is designed to proceed in the presence of the coordination processes occurring during surface functionalization. The hierarchical structure forms after the self-assembly of the shell MOF outside the core MOFs. The whole process is controlled by kinetics so that different components can be precisely placed outside the original core MOF crystal lattice while maintaining the structural integrity of the core MOF.

5.2 Experimental Section

General synthetic condition for hierarchical MOFs. Relative stable core MOFs were placed in the precursor solution containing linkers of shell MOFs. After the linker preloading and surface functionalization, solution containing metals of shell MOFs was added into the mixtures, allowing the formation of shell MOFs outside core MOFs.

Synthesis of MOF-5. MOF-5 was synthesized on the basis of previous reports with slight modifications.[13] $Zn(NO_3)_2 \cdot 6H_2O$ (41.6 mg), BDC (8.8 mg) and DEF (2 mL) were charged in a Pyrex vial. The mixture was heated in an 85 ºC oven for 24 h to generate the cubic crystals of MOF-5. The crystals of MOF-5 were collected by centrifugation and washed with fresh DMF for 3 times (Figure 47-48). Synthesis of MOF-5 under 100 ºC also generates similar cubic crystals.

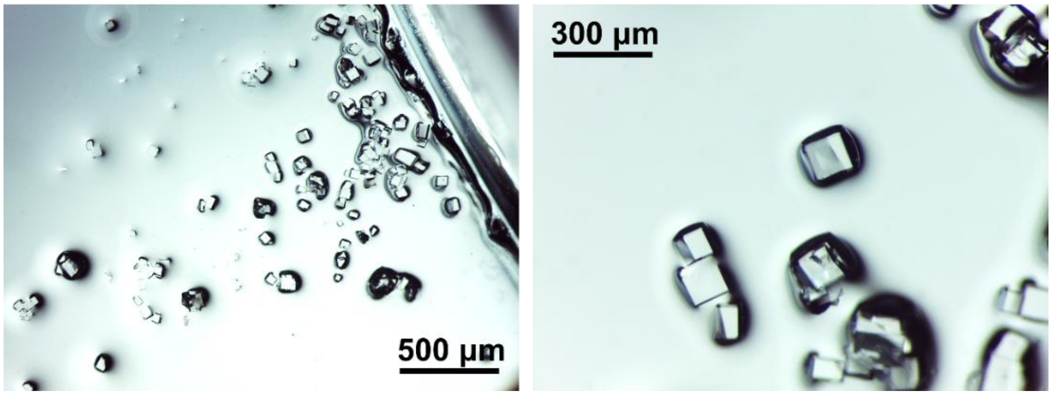

Figure 47. Microscopic images of MOF-5 crystals.

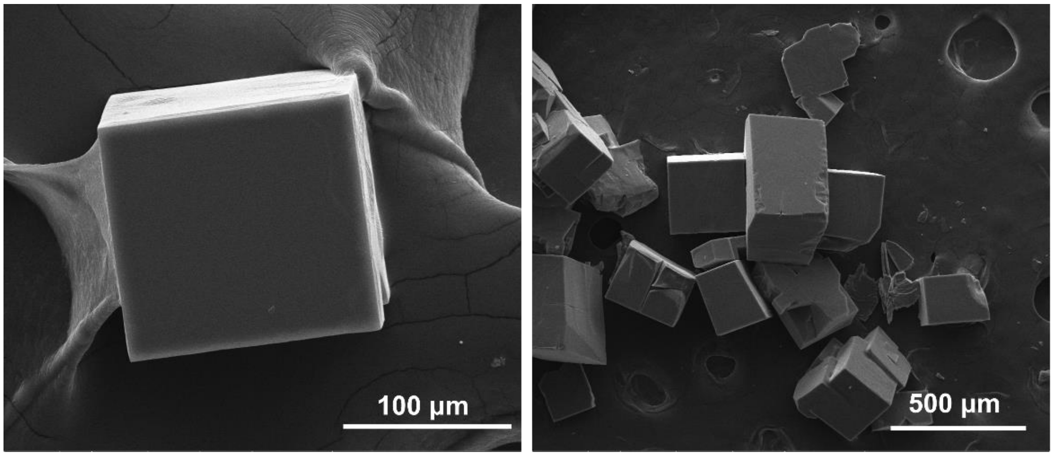

Figure 48. SEM images of MOF-5.

Synthesis of PCN-222. PCN-222(No Metal) was synthesized on the basis of previous reports with slight modifications.[52] $ZrCl_4$ (70 mg), TCPP (50 mg) and benzoic acid (2700 mg) in *N*,*N*-diethylformamide (8 mL) were ultrasonically dissolved in a 20 mL Pyrex vial. The mixture was heated at 120 °C in an oven for 48 h. After cooling down to room temperature, needle-shaped crystals were harvested by filtration (Figure 49).

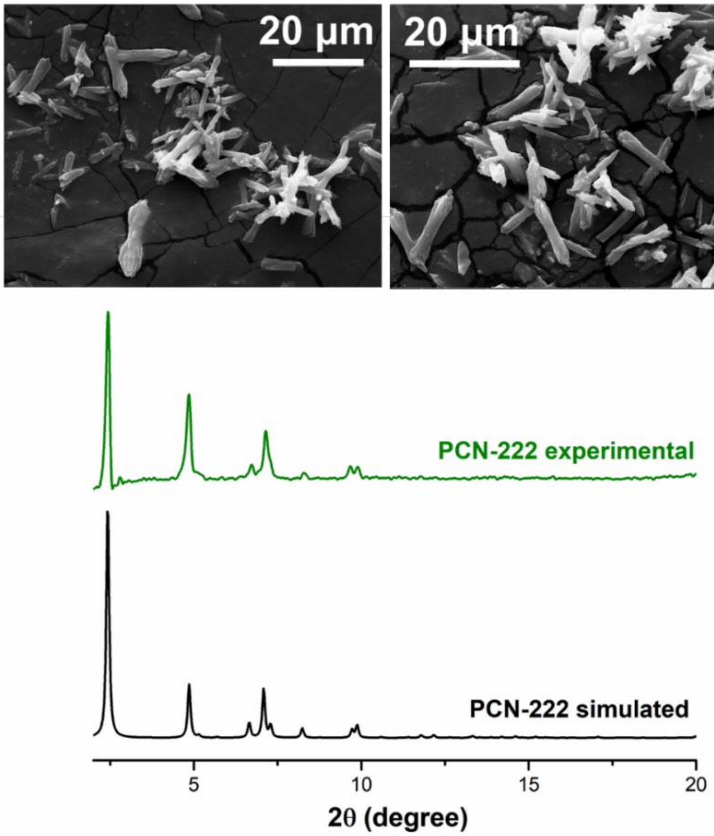

Figure 49. SEM images and PXRD patterns of PCN-222.

Synthesis of PCN-222(Zn)@MOF-5. Activated PCN-222 (12 mg), BDC (8.8 mg) and DEF (1 mL) were charged in a Pyrex vial. The mixture was heated in an 85 ºC oven for 24 h. $Zn(NO_3)_2{\cdot}6H_2O$ (41.6 mg) and DEF (1 mL) were further added into the vial.

The mixture was heated in an 85 ºC oven for 24 h to generate the crystals of PCN-222(Zn)@MOF-5. The crystals were collected by centrifugation and washed with fresh DMF for 3 times (Figure 50-51, Table 8).

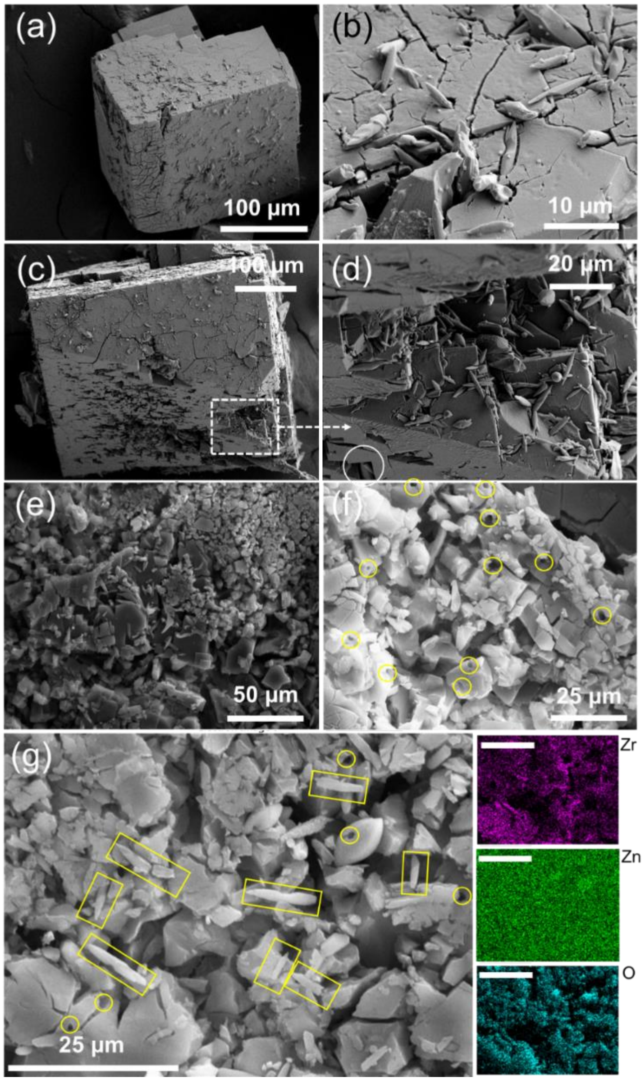

Figure 50. SEM images and corresponding SEM-EDS mapping of hierarchical PCN-222@MOF-5-(8%).

Table 8. Approximate composition of PCN-222@MOF-5.

Sample Name	Average Composition
PCN-222	$Zr_6(\mu_3\text{-}O)_4(\mu_3\text{-}OH)_4(OH)_4(H_2O)_4(ZnTCPP)_2$
MOF-5	$Zn_4O(BDC)_3$
PCN-222@MOF-5-(14%)	$[Zr_6(\mu_3\text{-}O)_4(\mu_3\text{-}OH)_4(OH)_4(H_2O)_4(ZnTCPP)_2]_1\ [Zn_4O(BDC)_3]_{5.9}$
PCN-222@MOF-5-(8%)	$[Zr_6(\mu_3\text{-}O)_4(\mu_3\text{-}OH)_4(OH)_4(H_2O)_4(ZnTCPP)_2]_1\ [Zn_4O(BDC)_3]_{11.5}$
PCN-222@MOF-5-(1%)	$[Zr_6(\mu_3\text{-}O)_4(\mu_3\text{-}OH)_4(OH)_4(H_2O)_4(ZnTCPP)_2]_1\ [Zn_4O(BDC)_3]_{86.5}$

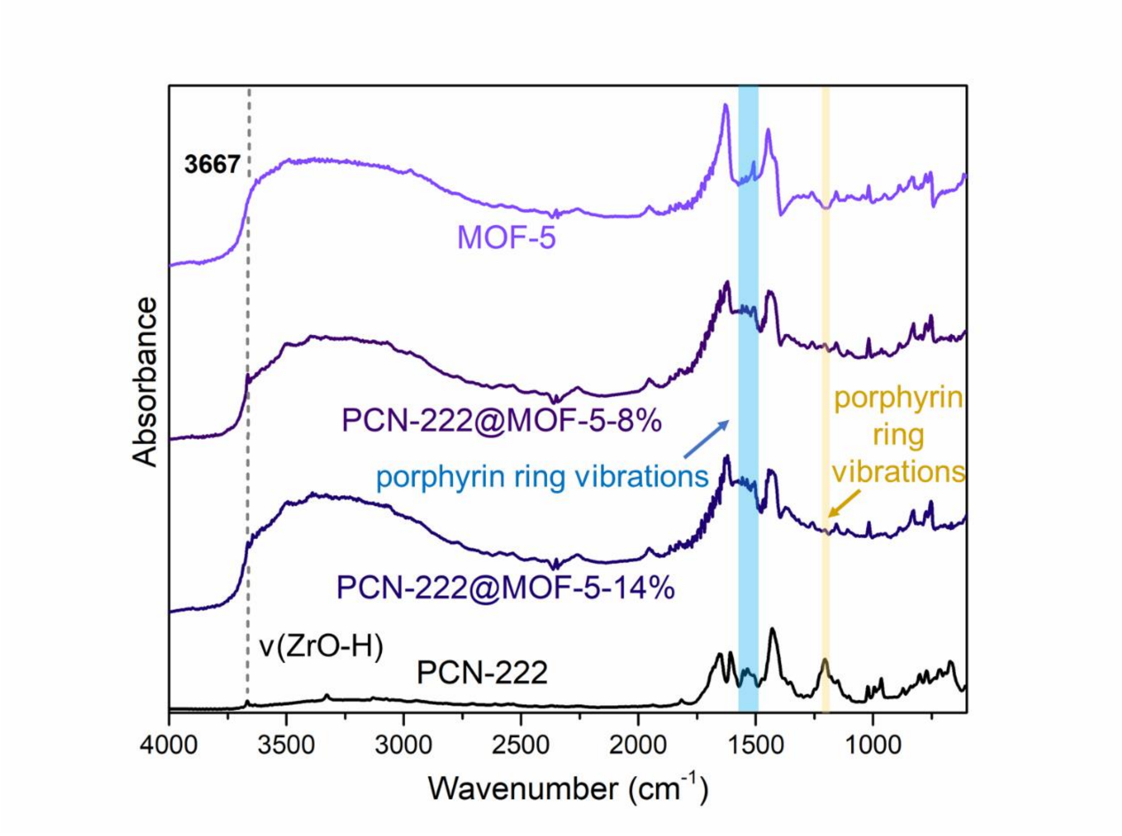

Figure 51. The full DRIFTS spectra of MOF-5, PCN-222@MOF-5-8%, PCN-222@MOF-5-14% and PCN-222.

5.3 Results and Discussion

A zirconium-MOF, PCN-222 (also known as MOF-545),[52, 126] was used as a core scaffold for the growth of a MOF shell because the high chemical stability of PCN-222 ensures its structural integrity under post-synthetic modification conditions. Based on Pearson's hard/soft acid/base (HSAB) principle, MOFs based on different metal clusters should have distinct stabilities determined by the M—O bond strength.[122] Generally, the harsh solvothermal synthetic conditions of Zr-MOFs are not suitable for Zn-MOFs. Zhong and coworkers reported that Zn-MOFs gradually dissolve and become metal-linker complexes under the synthetic condition of UiO-66 (Zr).[127] In contrast, Zr-MOFs are robust frameworks that should be able to survive under the synthetic conditions of Zn-MOFs. However, due to the increased energy barrier caused by the mismatched lattice parameters, MOF-5[12] tends to grow separately when its precursor components are directly mixed with PCN-222. The heterogeneous nucleation of the Zn-MOF is not favored, leading to the formation of Zn- and Zr- MOF mixtures (Scheme 14).

To lower the energy barrier of heterogeneous nucleation during hierarchical MOF formation, the surfaces of the core MOFs were functionalized by pretreating with excess linker under solvothermal conditions (Scheme 14). This allowed for the coordination of the linkers on the surface of the core MOFs, and also resulted in the capture of preloaded linkers inside the MOF pores. Further addition of metal precursors to the system allowed for the gradual formation of shell MOFs on the surface of the core MOFs. The crystals of PCN-222 were further treated with an excess of benzene-1,4-dicarboxylic acid (BDC) as a dimethylformamide (DEF) solution for 24 h, followed by a DEF solution of

$Zn(NO_3)_2$ for another 24 h. As a result, a hierarchical MOF-on-MOF composite, PCN-222@MOF-5, was obtained.

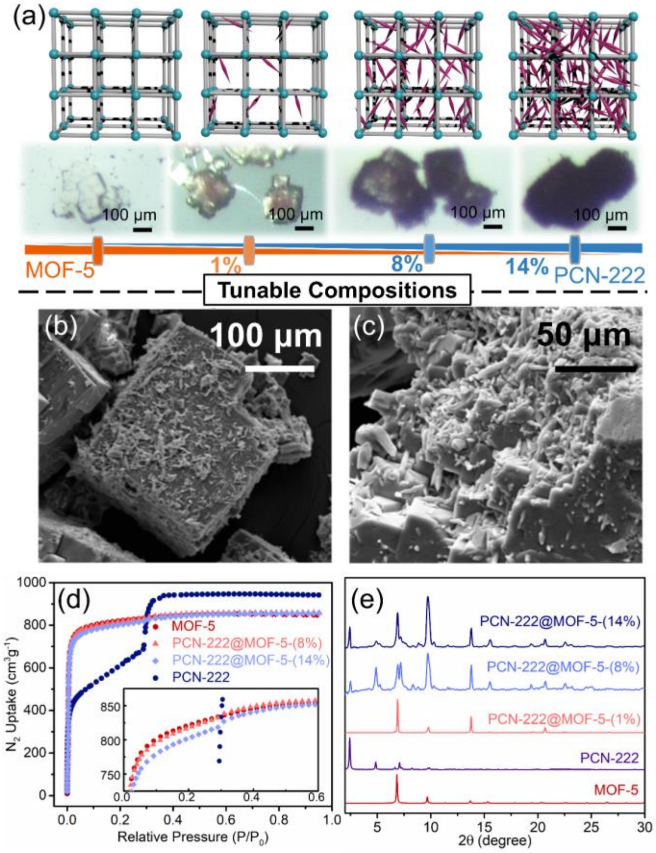

Figure 52. Tunable compositions in hierarchical PCN-222@MOF-5. (a) Models and optical images showing controlled incorporation of PCN-222 inside MOF-5, from 0% to 14%. (b-c) SEM images of the surface (b) and interior (c) of PCN-222@MOF-5-(8%). The internal areas of PCN-222@MOF-5-(8%) was accessed by physically crushing samples. (d-e) N_2 sorption isotherms and PXRD patterns of PCN-222@MOF-5-(R%, R = 1, 8 and 14).

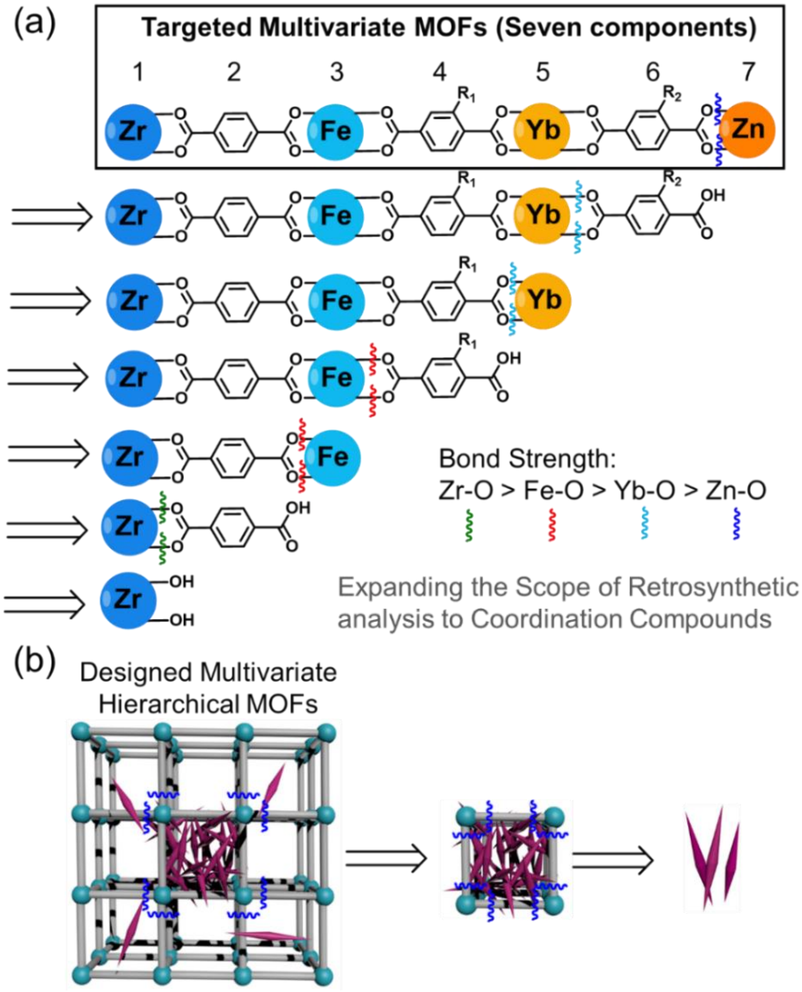

Scheme 15. Conceptual illustration of stepwise construction of multivariate hierarchical MTV-MOFs under the guidance of retrosynthetic design.

The formation of hierarchical MOFs could be clearly distinguished from optical microscopy images of the respective crystals (Figure 52). The core MOF, porphyrinic PCN-222 constructed from the four connected linker tetrakis(4-carboxyphenyl)porphyrin (TCPP), exhibited a purple color and a needle-like shape, whereas the shell MOF-5 exhibited colorless cubic features. Scanning electron microscopy (SEM) revealed that the needle-like PCN-222 crystals were well dispersed both inside and outside MOF-5. The morphology of PCN-222 was well maintained in the hierarchical structure. Powder X-ray diffraction (PXRD) patterns of the hierarchical MOFs demonstrated the well-maintained crystallinity of both core and shell MOFs.

Scanning electron microscopy/energy dispersive X-ray spectroscopy (SEM-EDS) and confocal laser scanning microscopy indicated that Zr was well dispersed in the lattice of the Zn-MOFs. The Zr/Zn ratio of both the internal and external structures of PCN-222@MOF-5 calculated from EDS mapping were consistent with the results from ICP-MS data of the digested MOF samples.

The PCN-222 to MOF-5 ratio could be well tuned in the hierarchical PCN-222@MOF-5 composites by adjusting the feed ratios, producing PCN-222@MOF-5-(R%), where R% is the mole percentage of PCN-222 as determined by ^{1}H-NMR (Table 8). The N_2 adsorption isotherms of the hierarchical PCN-222@MOF-5 were measured, showing hierarchical porosity as expected (Figure 52). The total N_2 uptakes were close to those of the shell MOFs, while a noticeable hysteresis loop near $P/P_0 = 0.3$ confirmed the presence of the core MOFs. The pore size distributions of hierarchical MOFs were calculated from the N_2 adsorption isotherms using a DFT model, showing the characteristic 32 Å peak of PCN-222. In contrast to our previously reported top-down approaches for hierarchical structures, linker labilization[46] and thermolysis[33], this retrosynthetic design showcases an alternative bottom-up approach for the design of sophisticated hierarchical structures.

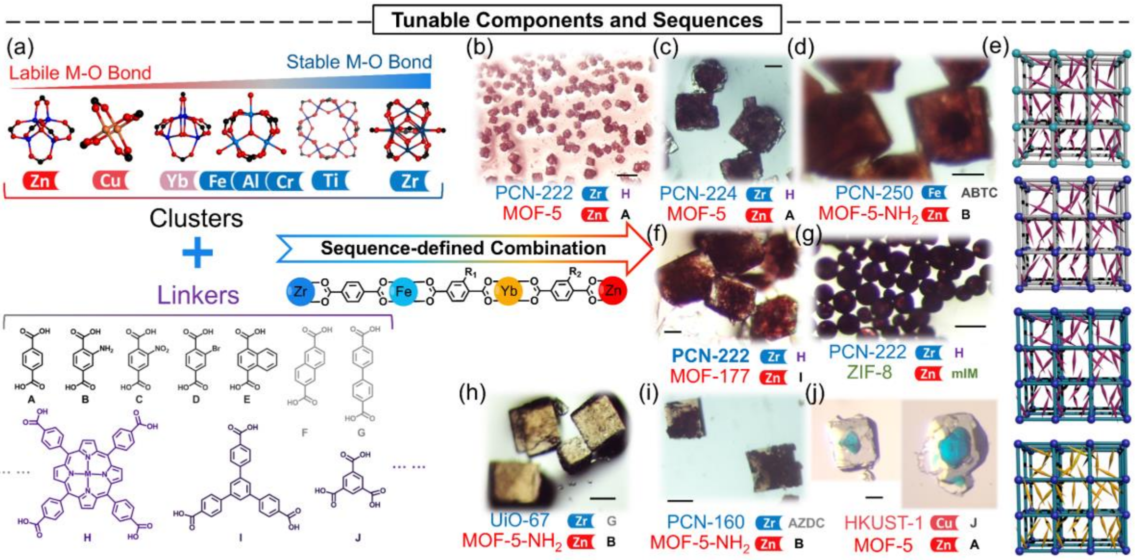

Figure 53. Versatility of kinetically guided retrosynthesis of hierarchical MOFs. (a) Sequence-defined combinations of clusters and linkers into hierarchical MOFs with controllable compositions and distributions. (b-d, f-j) Optical images of hierarchical MOFs with sequence-defined combinations guided by retrosynthetic stability consideration. Scale bar is 100 μm in all optical images. (e) Unlimited combination of multivariate hierarchical MOFs that can be synthesized under the guidance of the two principles.

To examine whether kinetically guided synthesis could function as a general strategy, we extended this approach to other common MOF systems to develop sophisticated hierarchical MOF composites (Scheme 15, Figure 53). We chose M(II) based carboxylate MOFs as the shell MOFs, for example, the MOF-5 (Zn) series, MOF-

177 (Zn), HKUST-1 (Cu), and MOF-1114 (Yb) due to their mild synthetic conditions, relative poor stability in acidic environments, and relatively large crystal sizes. Meanwhile, stable MOFs, including UiO-66 (Zr), UiO-67 (Zr), PCN-160 (Zr), MOF-808 (Zr), PCN-222 (Zr), PCN-250 (Fe), and MIL-125 (Ti) were selected as core MOFs because of their high chemical stability. Based on the principles discussed above, we were able to construct multi-component hierarchical MOFs with in a large number of combinations. The presence of both core MOFs and shell MOFs was confirmed by optical imaging and PXRD patterns. Our retrosynthetic design exhibits a general and powerful tool to control the distribution inside multivariate hierarchical MOFs.

Interestingly, by controlling the apportionment of core MOFs dispersed in shell MOFs, we were able to get three types of hierarchical MOF-on-MOF structures: well-mixed, center-concentrated, and half-half asymmetric distribution (Figure 54). Through centrifugal precipitation, core MOF (PCN-222) powders could be well stabilized at the bottom of the reaction vessels, allowing for the subsequent anisotropic growth of MOF-5. After the heterogenous nucleation and growth, asymmetric apportionment (similar to Janus particles) were generated as a result. In contrast, dispersing PCN-222 nanocrystals in a MOF-5 precursor solution through ultrasonic mixing followed by the crystallization process could lead to the formation of well-mixed “solid solutions” (PCN-222@MOF-5). Applying higher concentrations of MOF-5 precursors to the synthesis of hierarchical PCN-222@MOF-5 would further promote the formation of center-concentrated core-shell structures, as indicated by optical imaging. In this case, the cubic core was observed as the well mixed PCN-222@MOF-5, which facilitated the further growth of lattice matched shell MOF-5. Additionally, if both the core and shell MOFs have comparable sizes, core-shell structures, instead of solid solutions, would form directly.

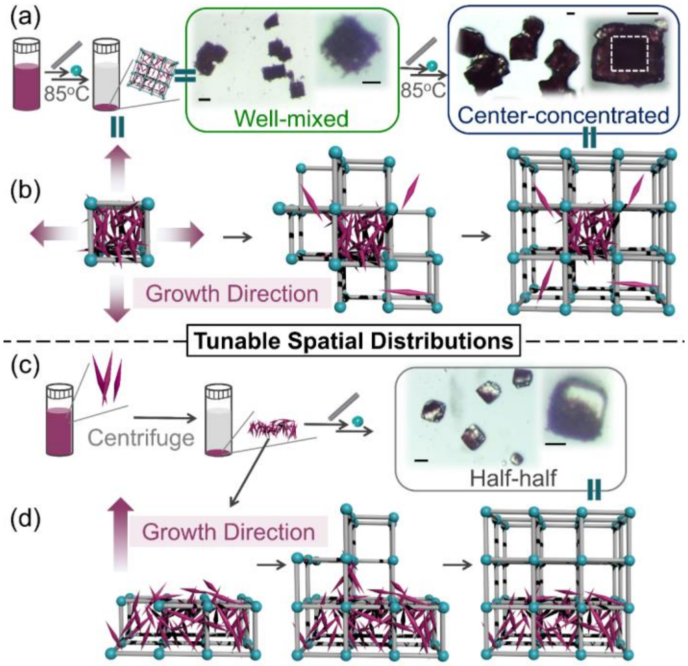

Figure 54. Tuning spatial distributions in hierarchical PCN-222@MOF-5. (a-b) Evolution of well-mixed and center-concertrated PCN-222@MOF-5 hierarchical MOFs. (c-d) Preparation of an asymmetric dispersion of PCN-222 in MOF-5 shell (similar to Janus particles). Scale bar is 100 μm in inserted images.

By utilizing the two principles described herein, numerous hierarchical MTV-MOFs could be designed and synthesized, with even multi-layer MTV MOFs being formed, expanding the scope of traditional MTV strategy for multi-component materials. Among the prepared hierarchical MOFs, PCN-222@ZIF-8 shows extraordinary stability in water, maintaining structural integrity in boiling water for more than 24 h. Compared with the traditional one-pot introduction of functionality inside of MOFs, this retrosynthetic synthesis of PCN-222@ZIF-8 provides a method for introducing linkers with various functional groups and connectivities without interfering with the growth process. This heterogenous growth (without TCPP competition) helped us obtain highly crystalline MOFs and overcome the impurity problems associated with the homogenous nucleation process (resulting from TCPP competition). Porphyrins or metalloporphyrins show wide applications in areas such as catalysis, photo-chemistry, and biological applications; therefore, the efficient immobilization of porphyrins in porous supports with controllable pore environment is highly desired for targeted applications. In contrast, we have shown that TCPP@ZIF-8, synthesized by a one-pot solvothermal reaction between TCPP, Zn^{2+}, 2-methylimidazole (mIM) and DMF, shows a relative low level of crystallinity for ZIF-8, possibly due to the competitive coordination between TCPP and mIM under homogenous conditions. However, the introduction of heterogenous PCN-222 as seeds can effectively avoid the competition, generating highly crystalline ZIF-8 with porphyrin units well dispersed inside of ZIF-8. In addition, TCPP is more firmly immobilized in PCN-222@ZIF-8 than in TCPP@ZIF-8 when exposed to harsh conditions due to the presence of the more robust coordination bonds between TCPP and Zr clusters.

5.4 Conclusion

Altogether, these results exemplify the capability of retrosynthetically guided preparation of multivariate hierarchical systems with tailored pore environment and cooperative behaviors, giving an unparalleled level of control over guest storage and transportation. This kinetically guided synthesis of hierarchical MOFs offers an ideal platform for the systematic tuning of pore environments and guest penetration behavior by the judicious choosing of clusters and linkers on core and shell MOFs. The current results already show the benefit of systems such as these for substrate selectivity processes. The incorporation of size selective components as a shell over a catalytically active porphyrinic MOF core has already shown applicability for the size selective oxidation of organic substrates. These results show the possibility of these core shell structures and provide a general method that should allow for the controlled growth of tailored catalytic and capture materials. Potential applications include using a core MOF designed as a mesoporous MOF with preloaded drugs, while the shell MOF could be constructed with multiply functional groups that engage in favorable interactions with either the guest molecules or particular cell environments. This would allow for the controlled release of drug molecules to areas of interest in the body. In addition, the heterogeneous nucleation of the shell MOF on the core MOF can allow for the controlled growth of materials that would be incompatible in a one-pot systems, such as growing an acidic MOF onto the surface of a basic MOF.

CHAPTER VI

ENGINEERING HIERARCHY AND HETERARCHY IN MOF@POLYMER COMPOSITES*

6.1 Introduction

The concept that complex systems have a hierarchical, or multi-level, organization has been widely observed at various scales, from the atomic to astronomical level, and from cells to society.[128-129] For example, the well-defined hierarchical modules and their sequences in human brain networks have enabled our ability to perform complicated functions and engage in well-controlled behaviors.[130] These features have inspired chemists to design tailored architectures with controllable hierarchy and heterogeneity in a wide range of materials including polymers, porous materials, and nanomaterials.[5, 32, 131-132] For example, recent works on hierarchical metal-organic frameworks (MOFs) have demonstrated unusual properties and behaviors which are accomplished through the precise placement of functionalities that can complete tandem chemical processes.[8, 18, 24, 121, 133]

MTV polymer/MOF composites have also been regarded as promising hierarchical systems due to their combination of a soft system with high processability and a robust system with well-controlled pore environments, which has shown wide

---

[*] This chapter is reproduced with permission from Feng, L.; Lv, X.-L; Yan, T.-H.; Zhou, H.-C., Modular Programming of Hierarchy and Diversity in Multivariate Polymer/Metal−Organic Framework Hybrid Composites, *J. Am. Chem. Soc.* **2019**, 141 (26), 10342-10349, Copyright 2019 by American Chemical Society.

applications in adsorption, separation, and catalysis.[134-141] One effective way to prepare the polymer/MOF composites is through post-synthetic polymerization.[137, 142] For example, Wang and coworkers demonstrate the initiator functionalization of UiO-66-NH_2 with a methacrylate monomer.[143] Matzger and coworkers studied the formation of MOF-5-polystyrene via a controlled styrene polymerization process that resulted in the polystyrene being uniformly distributed throughout the cubic MOF-5 crystals.[144] However, in these examples, the internal porosity is partially blocked by the polymers, leading to decreased surface areas and accessible pore volumes. In order to selectively functionalize the MOF surfaces, Kokado and Sada et al. chose poly(N-isopropylacrylamide) (PNIPAM), a polymer whose monomer is significantly larger than the pore sizes of UiO-66-NH_2, to modify the MOF surfaces while preserving the bulk porosity.[145] In addition, a preformed polymer backbone can also be utilized to construct polymer/MOF composites according to reports by Cohen group.[146] In this case, the linkers are incorporated into a polymer backbone and subsequently coordinated with metal clusters to form "polyMOFs". The covalent immobilization of polymer chains onto MOF surfaces can be achieved without disturbing the majority of the framework structure. However, the precise hierarchical engineering of modular compositions, the controlling of the ratios and distributions of polymer and MOF within the composites, has not been reached. The controlled developed of these designer materials has become a persistant challenge mainly due to the incompatibilities of the two parent materials.

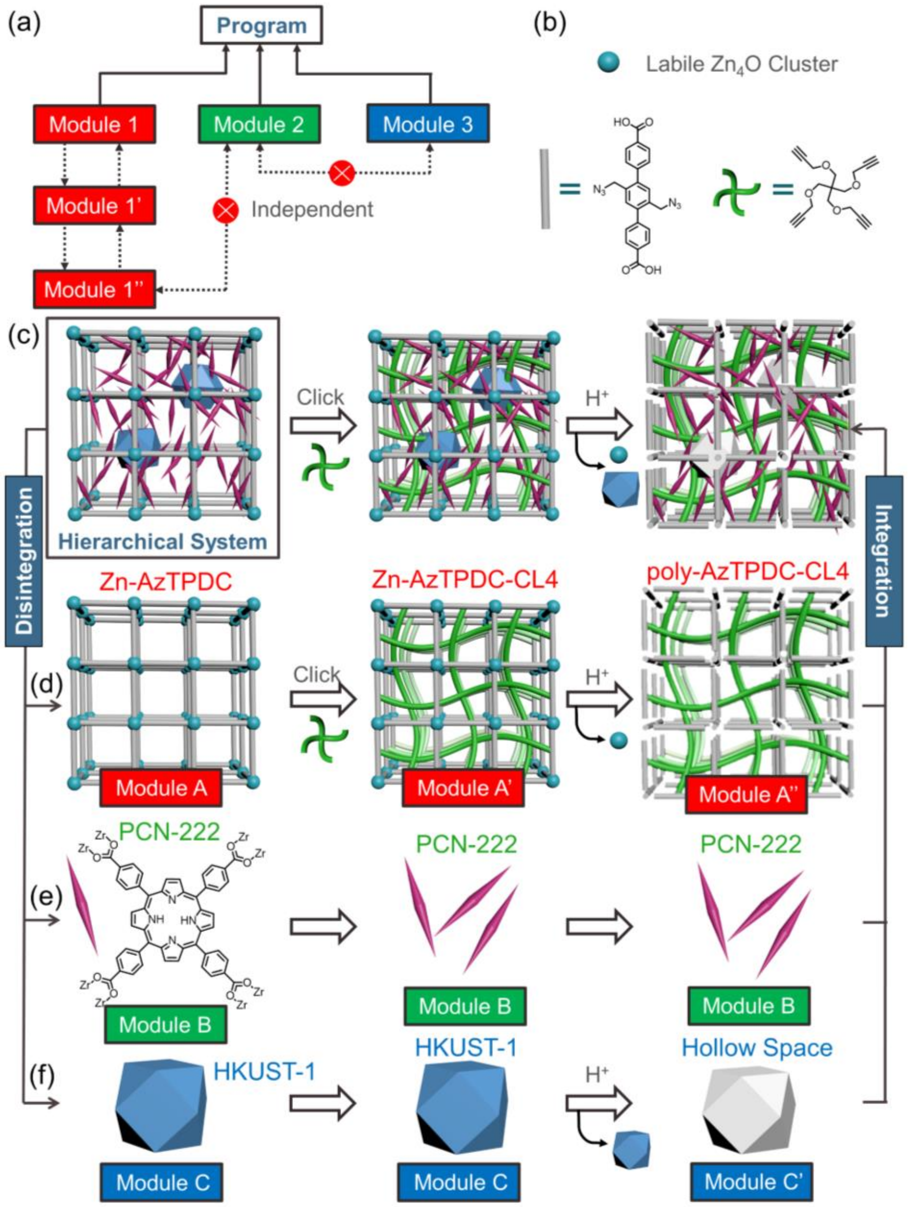

Scheme 16. Illustration of the concept of modular programming on the synthesis of multivariate (MTV) hierarchical polymer/metal-organic framework (MOF) composites.

In this work, we introduce the concept of modular programming to tailor the hierarchy and diversity in MTV polymer/MOF hybrid composites (Scheme 16). The idea of modular programming, inspired by C++ software design principles, emphasizes isolating the functionalities of a system into independent, interchangeable modules. Each module contains all the information necessary to execute only one desired functionality without interrupting the other modules. Guided by modular programming, a system with multiple compatible components including modules A, B, C, etc. can be constructed initially. Subsequently modification of each module into modules A’, B’, C’, etc. can be conducted independently without affecting the behaviors of the other modules. As a proof of concept, a series of MTV hierarchical MOFs with various compositions, ratios, and distributions can be prepared to showcase the compatibility of the modular approach. Sequential click reactions and acid treatments can be utilized to selectively modify a certain modular MOF into a polymer, while other modular MOFs either remain in their original states or dissolve upon treatment. As a result, a series of polymer/MOF composites with tailored properties and behaviors that would be traditionally viewed as incompatible can be prepared. The programmed hierarchy and diversity enable the possibility of biomimic cascade and cooperative processes commonly observed in cells, which typically require multiple components working coordinately. We envision that future materials should behave like a multi-functional living organism that aims to solve extremely complex and diverse tasks, including those related to transportation, movement, catalysis, detoxification, and response. All these functions are carried out by specialized modules, such as the individual flexible polymers and multivariate MOFs, while the cooperation of several modules with various functions acting in a coordinated way is needed.

6.2 Experimental Section

Synthesis of Zn-AzTPDC. Zn-AzTPDC was synthesized on the basis of previous reports with slight modifications.[147] AzTPDC (28 mg, 0.065 mmol) and $Zn(NO_3)_2·6H_2O$ (57 mg, 0.19 mmol) were dissolved in 5 mL of N,N-diethylformamide (DEF) in a screw top vial. The vial was kept standing at 80 °C for 3 days. The solution was decanted, and yellow cubic crystals were repeatedly washed with DMF.

Synthesis of PCN-222. PCN-222(No Metal) was synthesized on the basis of previous reports with slight modifications. $ZrCl_4$ (70 mg), TCPP (50 mg) and benzoic acid (2700 mg) in *N*,*N*-diethylformamide (8 mL) were ultrasonically dissolved in a 20 mL Pyrex vial. The mixture was heated at 120 °C in an oven for 48 h. After cooling down to room temperature, needle-shaped crystals were harvested by filtration.

Synthesis of PCN-222@Zn-AzTPDC. Activated PCN-222 (3 mg), AzTPDC (28 mg) and DEF (2.5 mL) were charged in a Pyrex vial. The mixture was heated in an 80 ºC oven for 24 h. $Zn(NO_3)_2·6H_2O$ (57 mg) and DEF (2.5 mL) were further added into the vial. The mixture was heated in an 80 ºC oven for 3 days to generate the crystals of PCN-222@Zn-AzTPDC-(3%). The solution was decanted, and the crystals were repeatedly washed with DMF.

Synthesis of Janus PCN-222@Zn-AzTPDC. Activated PCN-222 (12 mg), AzTPDC (28 mg) and DEF (2.5 mL) were charged in a Pyrex vial. The mixture was heated in an 80 ºC oven for 24 h. The solid was further precipitated at the bottom of the vial by centrifugation for 10 min. $Zn(NO_3)_2·6H_2O$ (57 mg) and DEF (2.5 mL) were further added into the vial slowly. The mixture was heated in an 80 ºC oven for 3 days to generate the crystals. The solution was decanted, and the crystals were repeatedly washed with DMF.

Polymerization of hierarchical MOFs (PCN-222@Zn-AzTPDC-CL4). The polymerization was conducted on the basis of previous reports with slight modifications.[147] PCN-222@Zn-AzTPDC was immersed in 5 mL of 0.1 M CL4 solution (DMF) in a screw top vial, and 250 µL of saturated CuBr solution (DMF) was added to the mixture. The vial was kept standing at 80 °C for 3 days. The supernatant was decanted, and the cubic crystals, PCN-222@Zn-AzTPDC-CL4, were repeatedly washed with DMF.

Synthesis of hierarchical polymer/MOFs (PCN-222@poly-AzTPDC-CL4). The hydrolysis was conducted on the basis of previous reports with slight modifications.[147] PCN-222@Zn-AzTPDC was immersed in a mixed solvent of HCl/DMF (1:5, v/v) in a screw top vial. The vial was kept standing at room temperature for 3 h. The supernatant was decanted, and cubic crystals were repeatedly washed with DMF.

Synthesis of HKUST-1@(PCN-222@Zn-AzTPDC). 0.49 g $Cu(NO_3)_2·3H_2O$ was dissolved in 3 mL of deionized water. 0.24 g H_3BTC was dissolved in 3 mL of ethanol. The $Cu(NO_3)_2$ solution was first mixed with 3 mL of DMF in a 20 mL scintillation vial. The H_3BTC solution and 12 mL of glacial acetic acid were subsequently added to the mixed solution. The mixture was heated in a 55 ºC oven for 72 h to generate the crystals of HKUST-1. Activated HKUST-1 (5 mg), PCN-222 (5 mg), AzTPDC (28 mg) and DEF (2.5 mL) were charged in a Pyrex vial. The mixture was heated in an 80 ºC oven for 24 h. $Zn(NO_3)_2 \cdot 6H_2O$ (57 mg) and DEF (2.5 mL) were further added into the vial. The mixture was heated in an 80 ºC oven for 3 days to generate crystals of HKUST-1@(PCN-222@Zn-AzTPDC). The solution was decanted, and the crystals were repeatedly washed with DMF.

Synthesis of (PCN-222@HKUST-1)@Zn-AzTPDC. PCN-222@HKUST-1 was first synthesized as the core MOF. PCN-222 (5 mg), H_3BTC (24 mg), EtOH (0.3 mL) and DMF (0.3 mL) were charged in a 4 mL Pyrex vial. The mixture was heated in a 55ºC oven for 24 h resulting in the surface coordination of BTC to PCN-222. $Cu(NO_3)_2 \cdot 3H_2O$ (49 mg), H_2O (0.3 mL) and HAc (1.2 mL) were further added into the vial. The mixture was heated in a 55 ºC oven for 3 d to generate the crystals of PCN-222@HKUST-1. The crystals were collected by centrifugation and washed with fresh DMF for 3 times. Activated PCN-222@HKUST-1 (5 mg), AzTPDC (28 mg) and DEF (2.5 mL) were charged in a Pyrex vial. The mixture was heated in an 80 ºC oven for 24 h. $Zn(NO_3)_2 \cdot 6H_2O$ (57 mg) and DEF (2.5 mL) were further added into the vial. The mixture was heated in an 80 ºC oven for 3 days to generate the crystals of (HKUST-1@PCN-222)@Zn-AzTPDC. The solution was decanted, and the crystals were repeatedly washed with DMF.

Synthesis of hierarchical polymer/MOF Composites. The polymerization and hydrolysis were conducted on the basis of previous reports with slight modifications.[147] Generally, the MOF-on-MOF composites were immersed in 5 mL of a 0.1 M CL4 solution (DMF) in a screw top vial, and 250 μL of saturated CuBr solution (DMF) was added to the mixture. The vial was kept standing at 80 °C for 3 days. The supernatant was decanted, and the cubic crystals were repeatedly washed with DMF. Subsequently, the MOF-on-MOF composites were immersed in a mixed solvent of HCl/DMF (1:5, v/v) in a screw top vial. The vial was kept standing at room temperature for 3 h. The supernatant was decanted, and cubic crystals were repeatedly washed with DMF (Figure 55-56).

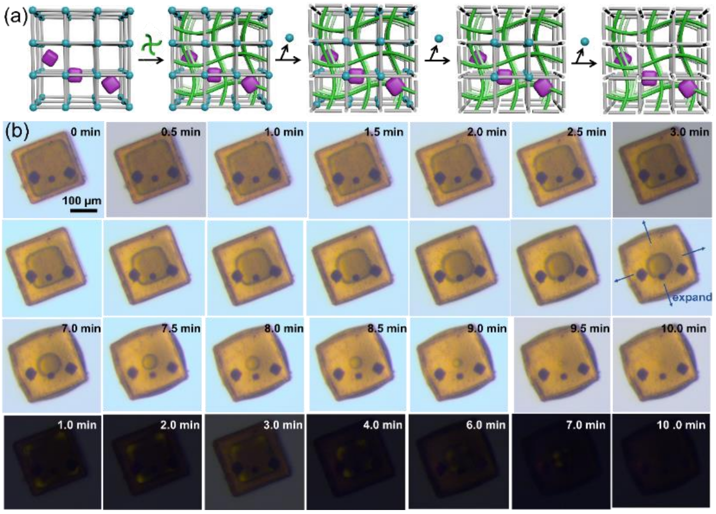

Figure 55. (a) Sequential polymerization and hydrolysis from PCN-224@Zn-AzTPDC to PCN-224@poly-AzTPDC-CL4. (b) Optical images of the stepwise removal of Zn_4O clusters in hierarchical PCN-224@Zn-AzTPDC-CL4 during treatment with acid solutions, and polarized optical images of crystals placed in between crossed polarizers during the transformation from PCN-224@Zn-AzTPDC-CL4 to PCN-224@poly-AzTPDC-CL4.

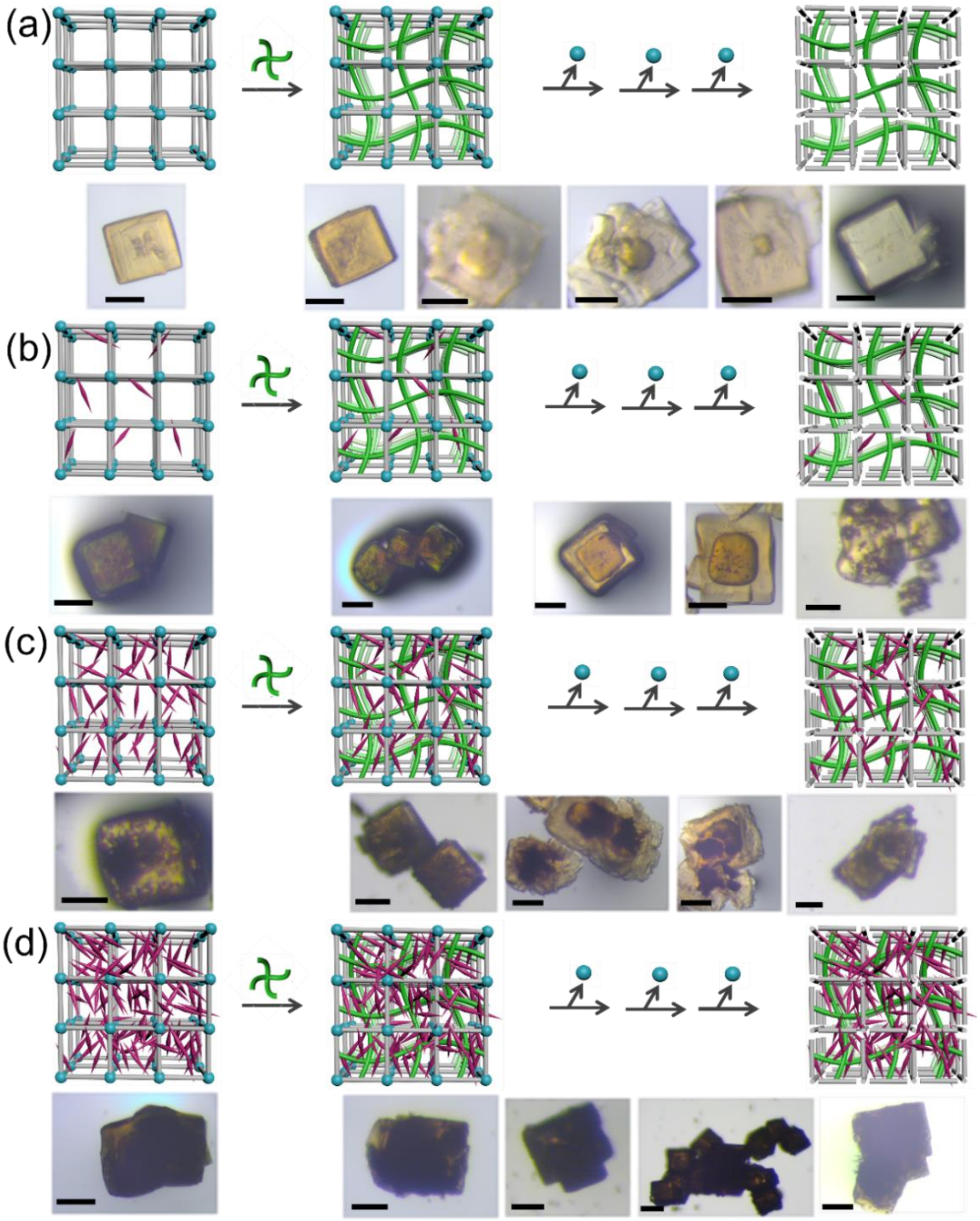

Figure 56. Optical images of the stepwise polymerization and hydrolysis in hierarchical PCN-222@Zn-AzTPDC-R% (R% is the mole percentage of PCN-222 in the hierarchical MOFs determined by ^{1}H-NMR of digested samples). (a) R = 0; (b) R = 3; (c) R = 7; (d) R = 12.

6.3 Results and Discussion

We first investigated module-independent behaviors in a simple two-module system. An MTV hierarchical PCN-222@Zn-AzTPDC was used as a scaffold for the preparation of polymer/MOF composites because of the significant difference in the chemical stability of the Zr-based PCN-222 and the Zn-based Zn-AzTPDC (PCN stands for porous coordination network, AzTPDC stands for diazide-triphenyldicarboxylate, **Scheme 16**). PCN-222 has been reported to be remarkably stable in an 8 M HCl solution as indicated by a well-maintained PXRD pattern and N_2 uptake. Zn-AzTPDC is isoreticular to the interwoven IRMOF-16[148] and shows limited chemical stability only when in common organic solvents. When exposed to water or acidic solutions, the Zn-AzTPDC framework quickly degrades and dissolves. In terms of mechanical stability, the framework of Zn-AzTPDC is not robust after the removal of guest solvents, leading to framework collapse as observed by PXRD and the corresponding N_2 sorption isotherm. We hypothesized that the stability contrast should enable the modular programming: when exposed to stimuli, specific modules will respond independently without affecting the behavior of the other modules.

Guided by a retrosynthetic design, the surface of chemical stable PCN-222 crystals were functionalized initially, allowing for the further growth of the relatively labile Zn-AzTPDC as a shell MOF.[24] The crystals of PCN-222 were treated with an excess of AzTPDC diethylformamide (DEF) solution for 24 h at 80 ^{o}C, followed by a DEF solution of $Zn(NO_3)_2$ for another 24 h at 80 ^{o}C. As expected, a MTV hierarchical PCN-222@Zn-AzTPDC, was obtained. The hierarchical PCN-222@Zn-AzTPDC MOF crystals could be clearly distinguished via optical micrsocopy (Figure 56). The core PCN-222, constructed from porphyrinic linkers, exhibited purple needle-like crystals, whereas the shell Zn-AzTPDC exhibited a colorless cubic morphology. The well-maintained crystallinity of both core PCN-222 and shell Zn-AzTPDC has been demonstrated by the PXRD patterns of the hierarchical MOFs.

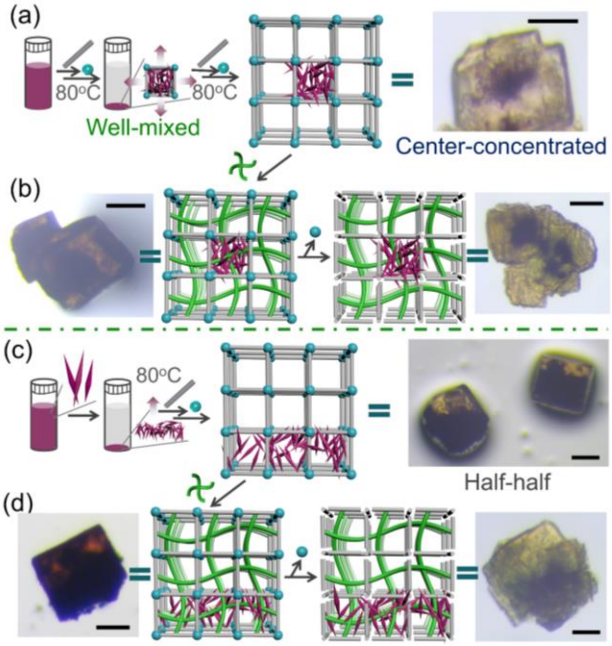

Figure 57. Tuning spatial distributions of PCN-222 in MTV hierarchical PCN-222@poly-AzTPDC-CL4 composites. (a) Preparation of center-concertrated PCN-222@Zn-AzTPDC. (b) Models and optical images of PCN-222@poly-AzTPDC-CL4. (c) Preparation of an asymmetric dispersion of PCN-222 in Zn-AzTPDC shell. (d) Models and optical images of Janus PCN-222@poly-AzTPDC-CL4. Scale bar is 100 μm in (a-d).

Next, we demonstrated that the PCN-222 to Zn-AzTPDC ratio could be adjusted in the hierarchical PCN-222@Zn-AzTPDC composites by simply tuning the feed ratios of the two MOF precursors. The optical images of the resulting PCN-222@Zn-AzTPDC-(R%) are shown in Figure 56, where R% is the mole percentage of PCN-222 as determined by the ^{1}H-NMR of the digested samples. The N_2 sorption isotherm of the hierarchical PCN-222@Zn-AzTPDC-(12%) was measured, showing a much lower N_2 uptake as compared to pure PCN-222, due to the presence of nonporous Zn-AzTPDC as the dominated shell MOF in the hierarchical composite.

The independent module behavior was further utilized to prepare MTV polymer/MOF hybrid composites via polymerization and hydrolysis. The preformed hierarchical PCN-222@Zn-AzTPDC templates were reacted with a tetra-acetylene cross-linker (CL4, Scheme 16b) through a copper-catalyzed azide–alkyne cycloaddition (CuAAC) click reaction that has a well-established procedure.[147, 149-151] After three days, the product crystals, PCN-222@Zn-AzTPDC-CL4, were washed repeatedly with fresh DMF. As a result, tunable ratios of PCN-222 crystals inside click-formed Zn-AzTPDC-CL4 were obtained (Figure 56). The polymerized PCN-222@Zn-AzTPDC-CL4 was subsequently treated with a HCl/dimethylformamide (DMF) (1/5, v/v) solution to selectively remove the Zn clusters in the hierarchical structures while maintaining the stable Zr-based PCN-222. The ratio and apportionment of the core PCN-222 remains in the resulting PCN-222@poly-AzTPDC-CL4 as indicated by the optical images (Figure 56).

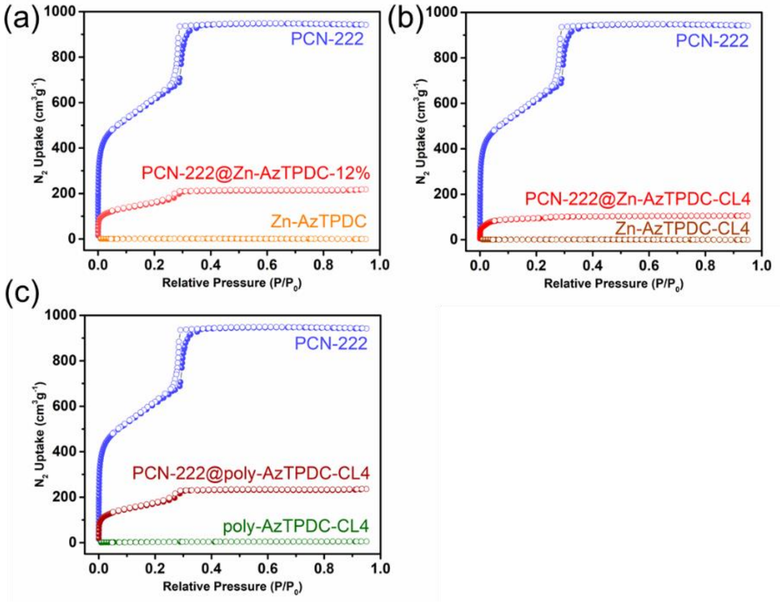

Figure 58. N_2 sorption isotherms of (a) PCN-222, Zn-AzTPDC, and PCN-222@Zn-AzTPDC-12%; (b) PCN-222, Zn-AzTPDC-CL4, and PCN-222@Zn-AzTPDC-CL4; (c) PCN-222, poly-AzTPDC-CL4, and PCN-222@poly-AzTPDC-CL4.

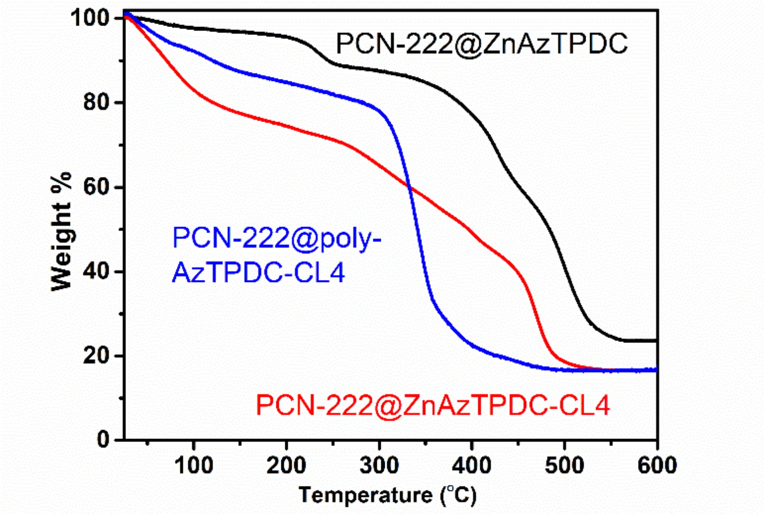

Figure 59. Thermogravimetric analysis of PCN-222@Zn-AzTPDC, PCN-222@Zn-AzTPDC-CL4, and PCN-222@poly-AzTPDC-CL4.

As indicated by optical images (Figure 55), the hierarchical MOF composite gradually expands in volume. Due to the limited acid diffusion rate, an interface between the edge polymer (poly-AzTPDC-CL4) and the center cubic MOF (Zn-AzTPDC-CL4) could be easily distinguished. Within 10 min, the hierarchical MOFs can be transformed into hierarchical polymer/MOF composites without a noticeable change in the apportionment and cubic morphology. It should be noted that without polymerization, PCN-222@Zn-AzTPDC could not maintain its morphology after hydrolysis. The Zn-AzTPDC shell MOFs tended to gradually dissolve and the immobilized PCN-222 were gradually released from the hierarchical structures, which emphasizes the importance of polymerization during the modular programming process. Similar decomposition of hierarchical MOFs, for example PCN-224@MOF-5, have also been recorded in previous reports.[24]

The transformation process was monitored by FT-IR spectroscopy and PXRD analysis. An azide stretching band at 2095 cm^{-1} was observed in the spectra of PCN-222@Zn-AzTPDC, while that same peak disappears in the spectra of the clicked PCN-222@Zn-AzTPDC-CL4 and PCN-222@poly-AzTPDC-CL4. This feature indicates that all the azide groups in PCN-222@Zn-AzTPDC have clicked with acetylene groups of the cross-linker. The peak at 1405 cm^{-1} of PCN-222@Zn-AzTPDC, associated with the carboxylate C=O symmetric vibration band, is well-maintained after the click reaction, demonstrating that the click reaction did not influence the Zn-carboxylate bonds under the mild conditions. After the hydrolysis of PCN-222@Zn-AzTPDC-CL4, the intensity of the carboxylate C=O peak at 1405 cm^{-1} decreases significantly, while a new peak at

1706 cm^{-1}, associated with carboxylic acid appears. This indicated the successful acidification of the carboxylate groups into carboxylic acids after the hydrolysis. The PCN-222@poly-AzTPDC-CL4 functionalized with carboxylic acid groups can be further modified with Zn ions, allowing for the coordination of Zn ions and the transformation from carboxylic acid to carboxylate groups again. In addition, the PXRD patterns show the well-maintained crystallinity of both the core PCN-222 and the shell Zn-AzTPDC after the click reaction, with the characteristic peaks of Zn-AzTPDC disappearing and the PCN-222 peaks remaining after acid treatment. This result supports the proposed modular programming of hierarchical two-module MOF structures.

Porosity and stability analysis of the resulting MTV hierarchical polymer/MOF composites were further conducted. It should be noted that the mechanical stability of Zn-AzTPDC is very poor. Thus, after activation, Zn-AzTPDC, its clicked, and acidified versions are nonporous (Figure 58). Notably, after the click reaction, the total N_2 uptake of PCN-222@Zn-AzTPDC-CL4 decreased slightly, possibly due to the trapped species inside the PCN-222 channels. These trapped molecules can be further removed alongside the labile Zn_4O clusters upon treatment with a HCl/DMF solution. The resulting composites also shown excellent chemical stability in various solvents with reversible flexible behaviors. Interestingly, the polymer network can undergo an adaptive guest inclusion: selective adsorption of a cationic dye (methylene blue) into the polymer network can be achieved while the anionic dye (methyl orange) cannot. Therefore, the polymer shell can function as a door to control the size and charge selectivity of guests. In terms of thermal stability, PCN-222@poly-AzTPDC-CL4 is stable up to around 300 ^{o}C (Figure 59). The weight loss at around 200 ^{o}C, associated with the azide group decomposition, in the TGA curve of PCN-222@Zn-AzTPDC is absent in the TGA curve of PCN-222@Zn-AzTPDC-CL4 and PCN-222@poly-AzTPDC-CL4, which also supports the completion of the CuAAC reaction between Zn-AzTPDC and CL4.

The manipulating MOF ratios, apportionment, and compositions in MTV polymer/MOF composites, usually deemed difficult or impossible to accomplish due to their incompatibility, has been achieved by the modular programming guided synthesis. Remarkably, half-half Janus-like and center-concentrated hierarchical PCN-222-on-Zn-AzTPDC structures can be fabricated by tuning the distribution of core MOFs within shell MOFs. After centrifugal precipitation, core PCN-222 powders stabilized at the bottom of the vials allows for the heterogenous nucleation and anisotropic growth of Zn-AzTPDC. This diffusion-limited solvothermal envioronment enables the formation of Janus-like PCN-222@Zn-AzTPDC crystals. The Janus-like PCN-222@Zn-AzTPDC crystals used as templates can further enable the sequential transformation into Janus PCN-222@poly-AzTPDC-CL4 with an asymmetric dispersion of PCN-222 in the polymer phase through the facile polymerization and hydrolysis treatment.

Additionally, increasing the concentration of Zn-AzTPDC precursors in the hierarchical MOF synthesis promotes the evolution of center-concentrated core-shell PCN-222@Zn-AzTPDC structures, as indicated by optical imaging (Figure 57), whereas well-mixed PCN-222@Zn-AzTPDC seeds facilitated the further growth of shell Zn-AzTPDC. Modular treatments on the stable PCN-222 phase and labile Zn-AzTPDC phase produce the correpounding polymer/MOF composites with controllable distributions. Thus, the positions of PCN-222 crystals inside polymer netwrok can be easily predetermined.

To examine whether modular programming could function as a general synthetic strategy, we extended this approach to various representative MOF systems and studied the related formation of sophisticated hierarchical polymer/MOF composites (Figure 55). For example, we chose a chemically stable cubic MOF, PCN-224, as the core MOF, and stepwise installed organic linkers and Zn_4O clusters outside the Zr-based PCN-224, leading to the formation of a PCN-224@Zn-AzTPDC structure. A time-resolved optical record, from the polymerized hierarchical MOFs to the hydrolyzed hierarchical polymer/MOF composites, were obtained within 10 min. The slight expansion of the cubic gels and the well-maintained PCN-224 crystals were observed. Microscopic images of the corresponding samples between crossed polarizers also indicated that the crystalline features of the core Zn-AzTPDC MOF and the amorphous feature of the shell polymer during the transformation. The PXRD patterns also support the independent modular modification during the polymerization and acidification process. Meanwhile, other stable MOFs, including MOF-801(Zr), UiO-66(Zr), UiO-67(Zr), PCN-160(Zr) and PCN-250 (Fe) were also selected as core MOF variants to enhance the diversity of the MTV hierarchical polymer/MOF composites.[122] Based on the underlying principles explored above, we were capable to construct MTV polymer/MOF composites with a large number of combinations. The pairing of stable MOF modules with labile while clickable Zn-MOF modules enables the programming of both hierarchy and diversity in the polymer/MOF composites. The formation of various composites including PCN-224@poly-AzTPDC-CL4, MOF-801@poly-AzTPDC-CL4, UiO-66@poly-AzTPDC-CL4, UiO-67@poly-AzTPDC-CL4, PCN-160@poly-AzTPDC-CL4 and PCN-250@poly-AzTPDC-CL4 were confirmed by optical images and PXRD patterns. Therefore, our modular programming here exhibits a general and powerful tool to manipulate hierarchy and diversity in MTV polymer/MOF hybrid composites.

To further enhance the complexity of the hierarchical systems, we introduce the concept of modularization into an integrated three-module system. Aiming to endow the third module with different stimulus-responsive behaviors from the other two modules, we chose HKUST-1 as the compatible component to tailor the diversity and hierarchy in the resulting composites. Unlike the non-responsive behavior of PCN-222 and the polymerization behavior of clickable Zn-AzTPDC, HKUST-1 can be selectively hollowed out after sequential click and acid treatments.

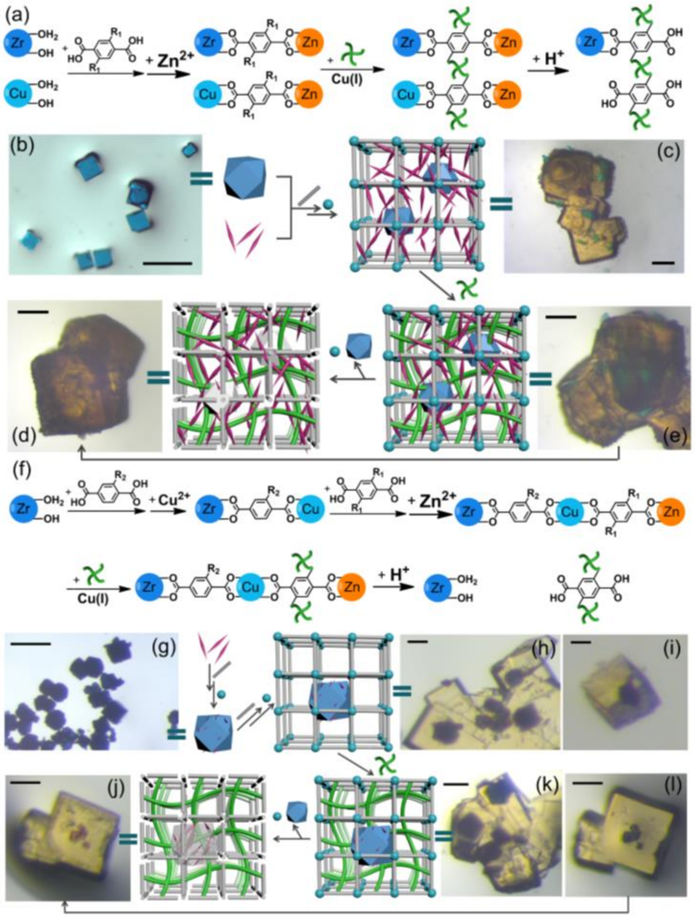

Figure 60. Modular programming on MTV hierarchical polymer/MOF composites. (a) Scheme illustration of the evolution of hollow@(PCN-222@poly-AzTPDC-CL4). (b) Optical images of HKUST-1 single crystals. (c) Optical images of HKUST-1@(PCN-222@Zn-AzTPDC) crystals. (d) Optical images of hollow@(PCN-222@poly-AzTPDC-CL4). (e) Optical images of HKUST-1@(PCN-222@Zn-AzTPDC-CL4) crystals. (f) Scheme illustration of the evolution of (PCN-222@hollow)@poly-AzTPDC-CL4. (g) Optical images of PCN-222@HKUST-1 crystals. (h-i) Optical images of (PCN-222@HKUST-1)@Zn-AzTPDC crystals. (j) Optical images of (PCN-

222@hollow)@poly-AzTPDC-CL4. (k-l) Optical images of (PCN-222@HKUST-1)@Zn-AzTPDC-CL4 crystals. Scale bar is 100 μm in (b-l).

When considering the retrosynthetic design principles of hierarchical MOFs, the synthesis sequences should be conducted in the order of decreasing bond strengths of these three modules (Zr-O > Cu-O > Zn-O).[122, 151] In other words, Zr-MOFs that require harsh synthetic conditions should be prepared first, and then installed with Cu-based and Zn-based coordination compounds sequentially (Figure 60). The multiple post-synthetic steps were achieved from Zr-based PCN-222 to PCN-222-BTC, PCN-222@HKUST-1, and PCN-222@HKUST-1-AzTPDC resulting in the final three-module hierarchical MOF (PCN-222@HKUST-1)@Zn-AzTPDC. The immobilization of PCN-222 insides the single crystals of HKUST-1 leads to the formation of purple cubes, while pure HKUST-1 possesses blue cubic features. The successful fabrication of the three-module core-shell MOF (PCN-222@HKUST-1)@Zn-AzTPDC with the PCN-222@HKUST-1 functioning as a seed for the epitaxial growth of Zn-AzTPDC. In this case, the apportionment of PCN-222 was strongly confined within the lattice of HKUST-1. After click modification, the morphology and color of the resulting (PCN-222@HKUST-1)@Zn-AzTPDC-CL4 remained. After acid exposure, the three modules displayed three totally different and independent behaviors: module A (Zn-AzTPDC) was transformed into an amorphous polymer while the cubic morphology was maintained; module B (PCN-222) was well preserved throughout all treatment; and module C (HKUST-1) was gradually dissolved and a hollow void was generated insides the composites. After selectively removing labile deep blue HKUST-1 crystals, the original dark PCN-222@HKUST-1 cores were turned into purple PCN-222@hollow cores. Overall, the integration of these individual modules together enables the successful fabrication of (PCN-222@hollow)@poly-AzTPDC-CL4 hierarchical structure.

Alternatively, the Zr-based PCN-222 and Cu-based HKUST-1 can both act as seeds for the epitaxial growth of a Zn-AzTPDC shell, resulting in the formation of HKUST-1@(PCN-222@Zn-AzTPDC). Different from the confined apportionment of PCN-222 in the previous (PCN-222@HKUST-1)@Zn-AzTPDC-CL4, PCN-222 is well dispersed in the hierarchical HKUST-1@(PCN-222@Zn-AzTPDC) structure. By sequential polymerization and acidification, HKUST-1 was selectively hollowed out while PCN-222 and Zn-AzTPDC were transformed into their desired forms. Eventually, a hollow@(PCN-222@poly-AzTPDC-CL4) with controlled hierarchy and diversity can be obtained. It should be noted that other synthetic sequences in the three-module system are impossible or extremely difficult to achieve due to the required retrosynthetic principles.

6.4 Conclusions

Overall, our results here exemplify the idea of modular programming on the hierarchy and diversity in MTV polymer/MOF composites. The engineering of the component ratio, spatial apportionment, and modular composition in polymer/MOF composites was achieved, giving an unparalleled level of control over guest transportation and recognition. The approach here utilizes the instability of modular

MOFs, a generally unwanted feature, to transform a certain module A into A', resulting in the construction of polymer/MOF composites that are traditionally viewed as incompatible. These results show the possibility of the tailored fabrication of multivariate materials with hierarchical structures. This general synthetic approach guided by modular programming also enables investigations into hierarchy and its structured control flow, which is a critical design feature of future materials for their fast adaptivity and responses to variable environmental conditions. Potential applications involving the cooperative effects between the multiple modules could be further developed.

CHAPTER VII

SUMMARY[*]

With increasing requirements for multifunctionalities and hierarchical structures in various applications, the study of multi-component hierarchical MOFs have prospered in recent years. Extensive efforts have been made to develop synthetic strategies for multi-component hierarchical MOFs with tunable linker or metal compositions and distributions, to decrypt the apportionment of these building blocks insides functional materials, and to utilize the cooperative effects among the multiple components and domains for specific applications. The one-pot or post-synthetic preparation of multi-component MOFs with tunable apportionment can be achieved, which allows us to fabricate sophisticated structures with synergic effects. Investigating the local pore environments insides multi-component hierarchical MOFs is critical to enhancing our understanding of the "structure-property-application" relationship, which shall guide the state-of-art design and synthesis of well-controlled porous materials. However, current characterization methods are still limited, lagging far behind the level of characterization seen in the biological systems, such as protein and DNA, that MTV-MOFs are attempting to imitate. In this respect, more systematic and precise characterization procedures are required to obtain more information in the local pore environment of multi-component hierarchical framework compounds. Based on currently utilized

---

[*] Reproduced with permission from: Feng, L.; Wang, K.-Y.; Gregory, D.; Zhou, H.-C. The Chemistry of Multi-component and Hierarchical Framework Compounds, *Chem. Soc. Rev.* **2019,** 48, 4823-4853. Copyright 2019 by The Royal Society of Chemistry.

techniques discussed above, the current batch of MTV-MOFs have shown wide applications including gas storage, separation, heterogeneous catalysis, guest delivery and luminescence behavior, exhibiting unexpected advantages over conventional single-component materials. MTV-MOFs can also serve as precursors for the preparation of other advanced functional materials including hierarchically porous structures, which also provides new routes to tune the porosity and functions of the resulting materials.

Programable pore environments have made major progress in the past decade. With growing research interests in multi-component hierarchical materials, an increasing number of related compounds have been reported, which show great applications in the area of selective binding and cooperative processes. However, the diversity and hierarchy of these materials have yet to reach the level of similarly complex biomaterials such as proteins and DNAs. From a synthetic perspective, future investigations should involve the "total synthesis" of complex frameworks from simple, basic building units through sequential chemical steps. The synthetic methodology in inorganic chemistry based on coordination bonds should be systematically designed and developed in the future. Additionally, the detailed characterization on the local porous environment, as well as their broader commercial and industrial scale applicability still need to be addressed. Despite the existing challenges in the development of both multi-component and hierarchical materials, advances in both new synthetic methodologies and characterization methods will continue to accelerate the discovery of multi-component hierarchical porous materials. When considering the high designability and diversity of these structures, it is promising to imagine a coming era filled by smart materials with unlimited tunability, synergism, and precision.

REFERENCES

1. Allen, M. J.; Tung, V. C.; Kaner, R. B., *Chem. Rev.* **2010,** *110* (1), 132-145.

2. Li, Z. X.; Barnes, J. C.; Bosoy, A.; Stoddart, J. F.; Zink, J. I., *Chem. Soc. Rev.* **2012,** *41* (7), 2590-2605.

3. Manners, I., *Angew. Chem. Int. Ed.* **1996,** *35* (15), 1602-1621.

4. Perez-Ramirez, J.; Christensen, C. H.; Egeblad, K.; Christensen, C. H.; Groen, J. C., *Chem. Soc. Rev.* **2008,** *37* (11), 2530-2542.

5. Lutz, J. F.; Ouchi, M.; Liu, D. R.; Sawamoto, M., *Science* **2013,** *341* (6146), 1238149.

6. Yuan, S.; Feng, L.; Wang, K.; Pang, J.; Bosch, M.; Lollar, C.; Sun, Y.; Qin, J.; Yang, X.; Zhang, P.; Wang, Q.; Zou, L.; Zhang, Y.; Zhang, L.; Fang, Y.; Li, J.; Zhou, H. C., *Adv. Mater.* **2018**, 1704303.

7. Li, J. R.; Sculley, J.; Zhou, H. C., *Chem. Rev.* **2012,** *112* (2), 869-932.

8. Zhou, H. C.; Long, J. R.; Yaghi, O. M., *Chem. Rev.* **2012,** *112* (2), 673-674.

9. Lee, J.; Farha, O. K.; Roberts, J.; Scheidt, K. A.; Nguyen, S. T.; Hupp, J. T., *Chem. Soc. Rev.* **2009,** *38* (5), 1450-1459.

10. Lu, W. G.; Wei, Z. W.; Gu, Z. Y.; Liu, T. F.; Park, J.; Park, J.; Tian, J.; Zhang, M. W.; Zhang, Q.; Gentle, T.; Bosch, M.; Zhou, H. C., *Chem. Soc. Rev.* **2014,** *43* (16), 5561-5593.

11. Zhou, H. C.; Kitagawa, S., *Chem. Soc. Rev.* **2014,** *43* (16), 5415-5418.

12. Li, H.; Eddaoudi, M.; O'Keeffe, M.; Yaghi, O. M., *Nature* **1999,** *402* (6759), 276-279.

13. Eddaoudi, M.; Kim, J.; Rosi, N.; Vodak, D.; Wachter, J.; O'Keeffe, M.; Yaghi, O. M., *Science* **2002,** *295* (5554), 469-472.

14. Popp, T. M. O.; Yaghi, O. M., *Acc. Chem. Res.* **2017,** *50* (3), 532-534.

15. Helal, A.; Yamani, Z. H.; Cordova, K. E.; Yaghi, O. M., *Natl. Sci. Rev.* **2017,** *4* (3), 296-298.

16. Furukawa, H.; Muller, U.; Yaghi, O. M., *Angew. Chem. Int. Ed.* **2015,** *54* (11), 3417-3430.

17. Meyers, M. A.; McKittrick, J.; Chen, P. Y., *Science* **2013,** *339* (6121), 773-779.

18. Kirchon, A.; Feng, L.; Drake, H. F.; Joseph, E. A.; Zhou, H. C., *Chem. Soc. Rev.* **2018,** *47* (23), 8611-8638.

19. Bates, F. S.; Hillmyer, M. A.; Lodge, T. P.; Bates, C. M.; Delaney, K. T.; Fredrickson, G. H., *Science* **2012,** *336* (6080), 434-440.

20. Marcos, V.; Stephens, A. J.; Jaramillo-Garcia, J.; Nussbaumer, A. L.; Woltering, S. L.; Valero, A.; Lemonnier, J. F.; Vitorica-Yrezabal, I. J.; Leigh, D. A., *Science* **2016,** *352* (6293), 1555-1559.

21. Matyjaszewski, K., *Science* **2011,** *333* (6046), 1104-1105.

22. Kametani, Y.; Sawamoto, M.; Ouchi, M., *Angew. Chem. Int. Ed.* **2018,** *57* (34), 10905-10909.

23. Kong, X. Q.; Deng, H. X.; Yan, F. Y.; Kim, J.; Swisher, J. A.; Smit, B.; Yaghi, O. M.; Reimer, J. A., *Science* **2013,** *341* (6148), 882-885.

24. Feng, L.; Yuan, S.; Li, J. L.; Wang, K. Y.; Day, G. S.; Zhang, P.; Wang, Y.; Zhou, H. C., *ACS Cent. Sci.* **2018,** *4* (12), 1719-1726.

25. Feng, L.; Li, J.-L.; Day, G. S.; Lv, X.-L.; Zhou, H.-C., *Chem* **2019,** *5*, 1265–1274.

26. Cornelio, J.; Zhou, T.-Y.; Alkaş, A.; Telfer, S. G., *J. Am. Chem. Soc.* **2018,** *140* (45), 15470-15476.

27. Zhou, T.-Y.; Auer, B.; Lee, S. J.; Telfer, S. G., *J. Am. Chem. Soc.* **2019,** *141* (4), 1577-1582.

28. Yuan, S.; Chen, Y.-P.; Qin, J.-S.; Lu, W.; Zou, L.; Zhang, Q.; Wang, X.; Sun, X.; Zhou, H.-C., *J. Am. Chem. Soc.* **2016,** *138* (28), 8912-8919.

29. Yuan, S.; Lu, W.; Chen, Y.-P.; Zhang, Q.; Liu, T.-F.; Feng, D.; Wang, X.; Qin, J.; Zhou, H.-C., *J. Am. Chem. Soc.* **2015,** *137* (9), 3177-3180.

30. Liu, L.; Konstas, K.; Hill, M. R.; Telfer, S. G., *J. Am. Chem. Soc.* **2013,** *135* (47), 17731-17734.

31. Liu, L.; Telfer, S. G., *J. Am. Chem. Soc.* **2015,** *137* (11), 3901-3909.

32. Deng, H. X.; Doonan, C. J.; Furukawa, H.; Ferreira, R. B.; Towne, J.; Knobler, C. B.; Wang, B.; Yaghi, O. M., *Science* **2010,** *327* (5967), 846-850.

33. Feng, L.; Yuan, S.; Zhang, L. L.; Tan, K.; Li, J. L.; Kirchon, A.; Liu, L. M.; Zhang, P.; Han, Y.; Chabal, Y. J.; Zhou, H. C., *J. Am. Chem. Soc.* **2018,** *140* (6), 2363-2372.

34. Boissonnault, J. A.; Wong-Foy, A. G.; Matzger, A. J., *J. Am. Chem. Soc.* **2017,** *139* (42), 14841-14844.

35. Fluch, U.; Paneta, V.; Primetzhofer, D.; Ott, S., *Chem. Commun.* **2017,** *53* (48), 6516-6519.

36. Gallego, E. M.; Portilla, M. T.; Paris, C.; Leon-Escamilla, A.; Boronat, M.; Moliner, M.; Corma, A., *Science* **2017,** *355* (6329).

37. Allen, C. A.; Boissonnault, J. A.; Cirera, J.; Gulland, R.; Paesani, F.; Cohen, S. M., *Chem. Commun.* **2013,** *49* (31), 3200-3202.

38. Allen, C. A.; Cohen, S. M., *Inorg. Chem.* **2014,** *53* (13), 7014-7019.

39. Park, K. S.; Ni, Z.; Cote, A. P.; Choi, J. Y.; Huang, R. D.; Uribe-Romo, F. J.; Chae, H. K.; O'Keeffe, M.; Yaghi, O. M., *P. Natl. Acad. Sci. USA* **2006,** *103* (27), 10186-10191.

40. Jayachandrababu, K. C.; Sholl, D. S.; Nair, S., *J. Am. Chem. Soc.* **2017,** *139* (16), 5906-5915.

41. Perdew, J. P.; Burke, K.; Ernzerhof, M., *Phys. Rev. Lett.* **1996,** *77* (18), 3865-3868.

42. Grimme, S., *J. Comp. Chem.* **2006,** *27* (15), 1787-1799.

43. Delley, B., *J. Chem. Phys.* **1990,** *92* (1), 508-517.

44. Liu, C. Y.; Liu, Q.; Huang, A. S., *Chem. Commun.* **2016,** *52* (16), 3400-3402.

45. Park, K. S.; Ni, Z.; Cote, A. P.; Choi, J. Y.; Huang, R. D.; Uribe-Romo, F. J.; Chae, H. K.; O'Keeffe, M.; Yaghi, O. M., *Proc. Natl. Acad. Sci. USA* **2006,** *103* (27), 10186-10191.

46. Yuan, S. A.; Zou, L. F.; Qin, J. S.; Li, J. L.; Huang, L.; Feng, L. A.; Wang, X. A.; Bosch, M.; Alsalme, A.; Cagin, T.; Zhou, H. C., *Nat. Comm.* **2017,** *8*, 15356.

47. Feng, L.; Yuan, S.; Qin, J.-S.; Wang, Y.; Kirchon, A.; Qiu, D.; Cheng, L.; Madrahimov, S. T.; Zhou, H.-C., *Matter* **2019,** *1*, 156-167.

48. Cohen, S. M., *Chem. Rev.* **2012,** *112* (2), 970-1000.

49. Delley, B., *J. Chem. Phys.* **2000,** *113* (18), 7756-7764.

50. Howarth, A. J.; Liu, Y. Y.; Li, P.; Li, Z. Y.; Wang, T. C.; Hupp, J.; Farha, O. K., *Nat. Rev. Mater.* **2016,** *1* (3), 15018.

51. Li, P.; Modica, J. A.; Howarth, A. J.; Vargas, E. L.; Moghadam, P. Z.; Snurr, R. Q.; Mrksich, M.; Hupp, J. T.; Farha, O. K., *Chem* **2016,** *1* (1), 154-169.

52. Feng, D. W.; Gu, Z. Y.; Li, J. R.; Jiang, H. L.; Wei, Z. W.; Zhou, H. C., *Angew. Chem. Int. Ed.* **2012,** *51* (41), 10307-10310.

53. Feng, D. W.; Liu, T. F.; Su, J.; Bosch, M.; Wei, Z. W.; Wan, W.; Yuan, D. Q.; Chen, Y. P.; Wang, X.; Wang, K. C.; Lian, X. Z.; Gu, Z. Y.; Park, J.; Zou, X. D.; Zhou, H. C., *Nat. Commun.* **2015,** *6*, 5979.

54. Mondloch, J. E.; Bury, W.; Fairen-Jimenez, D.; Kwon, S.; DeMarco, E. J.; Weston, M. H.; Sarjeant, A. A.; Nguyen, S. T.; Stair, P. C.; Snurr, R. Q.; Farha, O. K.; Hupp, J. T., *J. Am. Chem. Soc.* **2013,** *135* (28), 10294-10297.

55. Sun, L.-B.; Li, J.-R.; Park, J.; Zhou, H.-C., *J. Am. Chem. Soc.* **2012,** *134* (1), 126-129.

56. Qiu, L.-G.; Xu, T.; Li, Z.-Q.; Wang, W.; Wu, Y.; Jiang, X.; Tian, X.-Y.; Zhang, L.-D., *Angew. Chem. Int. Ed.* **2008,** *47* (49), 9487-9491.

57. Zhao, Y.; Zhang, J.; Han, B.; Song, J.; Li, J.; Wang, Q., *Angew. Chem. Int. Ed.* **2011,** *50* (3), 636-639.

58. Cao, S.; Gody, G.; Zhao, W.; Perrier, S.; Peng, X.; Ducati, C.; Zhao, D.; Cheetham, A. K., *Chem. Sci.* **2013,** *4* (9), 3573-3577.

59. Cai, G. R.; Jiang, H. L., *Angew. Chem. Int. Ed.* **2017,** *56* (2), 563-567.

60. Huang, H. L.; Li, J. R.; Wang, K. K.; Han, T. T.; Tong, M. M.; Li, L. S.; Xie, Y. B.; Yang, Q. Y.; Liu, D. H.; Zhong, C. L., *Nat. Commun.* **2015,** *6,* 8847.

61. Wee, L. H.; Wiktor, C.; Turner, S.; Vanderlinden, W.; Janssens, N.; Bajpe, S. R.; Houthoofd, K.; Van Tendeloo, G.; De Feyter, S.; Kirschhock, C. E. A.; Martens, J. A., *J. Am. Chem. Soc.* **2012,** *134* (26), 10911-10919.

62. Morris, R. E.; Cejka, J., *Nat. Chem.* **2015,** *7* (5), 381-388.

63. Wheatley, P. S.; Chlubna-Eliasova, P.; Greer, H.; Zhou, W. Z.; Seymour, V. R.; Dawson, D. M.; Ashbrook, S. E.; Pinar, A. B.; McCusker, L. B.; Opanasenko, M.; Cejka, J.; Morris, R. E., *Angew. Chem. Int. Ed.* **2014,** *53* (48), 13210-13214.

64. Kim, Y.; Yang, T.; Yun, G.; Ghasemian, M. B.; Koo, J.; Lee, E.; Cho, S. J.; Kim, K., *Angew. Chem. Int. Ed.* **2015,** *54* (45), 13273-13278.

65. Deria, P.; Mondloch, J. E.; Tylianakis, E.; Ghosh, P.; Bury, W.; Snurr, R. Q.; Hupp, J. T.; Farha, O. K., *J. Am. Chem. Soc.* **2013,** *135* (45), 16801-16804.

66. Vermoortele, F.; Bueken, B.; Le Bars, G.; Van de Voorde, B.; Vandichel, M.; Houthoofd, K.; Vimont, A.; Daturi, M.; Waroquier, M.; Van Speybroeck, V.; Kirschhock, C.; De Vos, D. E., *J. Am. Chem. Soc.* **2013,** *135* (31), 11465-11468.

67. Guillerm, V.; Ragon, F.; Dan-Hardi, M.; Devic, T.; Vishnuvarthan, M.; Campo, B.; Vimont, A.; Clet, G.; Yang, Q.; Maurin, G.; Ferey, G.; Vittadini, A.; Gross, S.; Serre, C., *Angew. Chem. Int. Ed.* **2012,** *51* (37), 9267-9271.

68. Garibay, S. J.; Cohen, S. M., *Chem. Commun.* **2010,** *46* (41), 7700-7702.

69. Kandiah, M.; Nilsen, M. H.; Usseglio, S.; Jakobsen, S.; Olsbye, U.; Tilset, M.; Larabi, C.; Quadrelli, E. A.; Bonino, F.; Lillerud, K. P., *Chem. Mater.* **2010,** *22* (24), 6632-6640.

70. Ingleson, M. J.; Barrio, J. P.; Guilbaud, J. B.; Khimyak, Y. Z.; Rosseinsky, M. J., *Chem. Commun.* **2008,** (23), 2680-2682.

71. Cavka, J. H.; Jakobsen, S.; Olsbye, U.; Guillou, N.; Lamberti, C.; Bordiga, S.; Lillerud, K. P., *J. Am. Chem. Soc.* **2008,** *130* (42), 13850-13851.

72. Shearer, G. C.; Chavan, S.; Ethiraj, J.; Vitillo, J. G.; Svelle, S.; Olsbye, U.; Lamberti, C.; Bordiga, S.; Lillerud, K. P., *Chem. Mater.* **2014,** *26* (14), 4068-4071.

73. Gutov, O. V.; Hevia, M. G.; Escudero-Adán, E. C.; Shafir, A., *Inorg. Chem.* **2015,** *54* (17), 8396-8400.

74. Wu, H.; Chua, Y. S.; Krungleviciute, V.; Tyagi, M.; Chen, P.; Yildirim, T.; Zhou, W., *J. Am. Chem. Soc.* **2013,** *135* (28), 10525-10532.

75. Cliffe, M. J.; Wan, W.; Zou, X. D.; Chater, P. A.; Kleppe, A. K.; Tucker, M. G.; Wilhelm, H.; Funnell, N. P.; Coudert, F. X.; Goodwin, A. L., *Nat. Commun.* **2014,** *5*, 4176.

76. Ambrosi, M.; Fratini, E. L.; Canton, P.; Dankesreiter, S.; Baglioni, P., *J. Mater. Chem.* **2012,** *22* (44), 23497-23505.

77. Padovini, D. S. S.; Pontes, D. S. L.; Dalmaschio, C. J.; Pontes, F. M.; Longo, E., *RSC Adv.* **2014,** *4* (73), 38484-38490.

78. Lemaire, P. C.; Lee, D. T.; Zhao, J. J.; Parsons, G. N., *ACS Appl. Mater. Inter.* **2017,** *9* (26), 22042-22054.

79. Valenzano, L.; Civalleri, B.; Chavan, S.; Bordiga, S.; Nilsen, M. H.; Jakobsen, S.; Lillerud, K. P.; Lamberti, C., *Chem. Mater.* **2011,** *23* (7), 1700-1718.

80. Gadipelli, S.; Guo, Z. X., *Chem. Mater.* **2014,** *26* (22), 6333-6338.

81. Yuan, S. A.; Zou, L. F.; Qin, J. S.; Li, J. L.; Huang, L.; Feng, L. A.; Wang, X. A.; Bosch, M.; Alsalme, A.; Cagin, T.; Zhou, H. C., *Nat. Commun.* **2017,** *8,* 15356.

82. Sun, Y. J.; Sun, L. X.; Feng, D. W.; Zhou, H. C., *Angew. Chem. Int. Ed.* **2016,** *55* (22), 6471-6475.

83. Li, J. R.; Kuppler, R. J.; Zhou, H. C., *Chem. Soc. Rev.* **2009,** *38* (5), 1477-1504.

84. Lian, X. Z.; Fang, Y.; Joseph, E.; Wang, Q.; Li, J. L.; Banerjee, S.; Lollar, C.; Wang, X.; Zhou, H. C., *Chem. Soc. Rev.* **2017,** *46* (11), 3386-3401.

85. Deng, H. X.; Grunder, S.; Cordova, K. E.; Valente, C.; Furukawa, H.; Hmadeh, M.; Gandara, F.; Whalley, A. C.; Liu, Z.; Asahina, S.; Kazumori, H.; O'Keeffe, M.; Terasaki, O.; Stoddart, J. F.; Yaghi, O. M., *Science* **2012,** *336* (6084), 1018-1023.

86. Shekhah, O.; Wang, H.; Paradinas, M.; Ocal, C.; Schupbach, B.; Terfort, A.; Zacher, D.; Fischer, R. A.; Woll, C., *Nat. Mater.* **2009,** *8* (6), 481-484.

87. Li, T.; Kozlowski, M. T.; Doud, E. A.; Blakely, M. N.; Rosi, N. L., *J. Am. Chem. Soc.* **2013,** *135* (32), 11688-11691.

88. Karagiaridi, O.; Bury, W.; Tylianakis, E.; Sarjeant, A. A.; Hupp, J. T.; Farha, O. K., *Chem. Mater.* **2013,** *25* (17), 3499-3503.

89. Liu, C.; Zeng, C. J.; Luo, T. Y.; Merg, A. D.; Jin, R. C.; Rosi, N. L., *J. Am. Chem. Soc.* **2016,** *138* (37), 12045-12048.

90. Lippke, J.; Brosent, B.; von Zons, T.; Virmani, E.; Lilienthal, S.; Preusse, T.; Hulsmann, M.; Schneider, A. M.; Wuttke, S.; Behrens, P.; Godt, A., *Inorg. Chem.* **2017,** *56* (2), 748-761.

91. Schaate, A.; Roy, P.; Preusse, T.; Lohmeier, S. J.; Godt, A.; Behrens, P., *Chem.-Eur. J.* **2011,** *17* (34), 9320-9325.

92. Bai, Y.; Dou, Y. B.; Xie, L. H.; Rutledge, W.; Li, J. R.; Zhou, H. C., *Chem. Soc. Rev.* **2016,** *45* (8), 2327-2367.

93. Ma, J.; Kalenak, A. P.; Wong-Foy, A. G.; Matzger, A. J., *Angew. Chem. Int. Ed.* **2017,** *56* (46), 14618-14621.

94. Yang, Q.; Guillerm, V.; Ragon, F.; Wiersum, A. D.; Llewellyn, P. L.; Zhong, C.; Devic, T.; Serre, C.; Maurin, G., *Chem. Commun.* **2012,** *48* (79), 9831-9833.

95. Hoang, L. T. M.; Ngo, L. H.; Nguyen, H. L.; Nguyen, H. T. H.; Nguyen, C. K.; Nguyen, B. T.; Ton, Q. T.; Nguyen, H. K. D.; Cordova, K. E.; Truong, T., *Chem. Commun.* **2015,** *51* (96), 17132-17135.

96. Marshall, R. J.; Hobday, C. L.; Murphie, C. F.; Griffin, S. L.; Morrison, C. A.; Moggach, S. A.; Forgan, R. S., *J. Mater. Chem. A* **2016,** *4* (18), 6955-6963.

97. Gao, W.-Y.; Thiounn, T.; Wojtas, L.; Chen, Y.-S.; Ma, S., *Sci. China Chem.* **2016,** *59* (8), 980-983.

98. Epley, C. C.; Love, M. D.; Morris, A. J., *Inorg. Chem.* **2017,** *56* (22), 13777-13784.

99. Yuan, S.; Zou, L. F.; Li, H. X.; Chen, Y. P.; Qin, J. S.; Zhang, Q.; Lu, W. G.; Hall, M. B.; Zhou, H. C., *Angew. Chem. Int. Ed.* **2016,** *55* (36), 10776-10780.

100. Rowan, S. J.; Cantrill, S. J.; Cousins, G. R. L.; Sanders, J. K. M.; Stoddart, J. F., *Angew. Chem. Int. Ed.* **2002,** *41* (6), 898-952.

101. Jin, Y. H.; Yu, C.; Denman, R. J.; Zhang, W., *Chem. Soc. Rev.* **2013,** *42* (16), 6634-6654.

102. Zhang, G.; Tsujimoto, M.; Packwood, D.; Duong, N. T.; Nishiyama, Y.; Kadota, K.; Kitagawa, S.; Horike, S., *J. Am. Chem. Soc.* **2018,** *140* (7), 2602-2609.

103. Shen, K.; Zhang, L.; Chen, X. D.; Liu, L. M.; Zhang, D. L.; Han, Y.; Chen, J. Y.; Long, J. L.; Luque, R.; Li, Y. W.; Chen, B. L., *Science* **2018,** *359* (6372), 206-210.

104. Dhakshinamoorthy, A.; Heidenreich, N.; Lenzen, D.; Stock, N., *Crystengcomm* **2017,** *19* (29), 4187-4193.

105. Fang, Q. R.; Gu, S.; Zheng, J.; Zhuang, Z. B.; Qiu, S. L.; Yan, Y. S., *Angew. Chem. Int. Ed.* **2014,** *53* (11), 2878-2882.

106. Ida, S.; Ouchi, M.; Sawamoto, M., *J. Am. Chem. Soc.* **2010,** *132* (42), 14748-14750.

107. Kametani, Y.; Sawamoto, M.; Ouchi, M., *Angew. Chem. Int. Ed.* **2018,** *57* (34), 10905-10909.

108. Khaletskaya, K.; Reboul, J.; Meilikhov, M.; Nakahama, M.; Diring, S.; Tsujimoto, M.; Isoda, S.; Kim, F.; Kamei, K. I.; Fischer, R. A.; Kitagawa, S.; Furukawa, S., *J. Am. Chem. Soc.* **2013,** *135* (30), 10998-11005.

109. Ding, K.; Cullen, D. A.; Zhang, L.; Cao, Z.; Roy, A. D.; Ivanov, I. N.; Cao, D., *Science* **2018,** *362*, 560-564.

110. Gutekunst, W. R.; Hawker, C. J., *J. Am. Chem. Soc.* **2015,** *137* (25), 8038-8041.

111. Pfeifer, S.; Lutz, J. F., *J. Am. Chem. Soc.* **2007,** *129* (31), 9542-9543.

112. Dong, Z. Y.; Sun, Y. Z. S.; Chu, J.; Zhang, X. Z.; Deng, H. X., *J. Am. Chem. Soc.* **2017,** *139* (40), 14209-14216.

113. Kirchon, A.; Feng, L.; Drake, H. F.; Joseph, E. A.; Zhou, H. C., *Chem. Soc. Rev.* **2018**, *47,* 8611-8638.

114. Qin, J. S.; Yuan, S.; Wang, Q.; Alsalme, A.; Zhou, H. C., *J. Mater. Chem. A* **2017,** *5* (9), 4280-4291.

115. Yuan, S.; Qin, J. S.; Li, J. L.; Huang, L.; Feng, L.; Fang, Y.; Lollar, C.; Pang, J. D.; Zhang, L. L.; Sun, D.; Alsalme, A.; Cagin, T.; Zhou, H. C., *Nat. Comm.* **2018,** *9,* 808.

116. Furukawa, S.; Hirai, K.; Nakagawa, K.; Takashima, Y.; Matsuda, R.; Tsuruoka, T.; Kondo, M.; Haruki, R.; Tanaka, D.; Sakamoto, H.; Shimomura, S.; Sakata, O.; Kitagawa, S., *Angew. Chem. Int. Ed.* **2009,** *48* (10), 1766-1770.

117. Li, T.; Sullivan, J. E.; Rosi, N. L., *J. Am. Chem. Soc.* **2013,** *135* (27), 9984-9987.

118. Choi, S.; Kim, T.; Ji, H.; Lee, H. J.; Oh, M., *J. Am. Chem. Soc.* **2016,** *138* (43), 14434-14440.

119. Zhao, M. T.; Yuan, K.; Wang, Y.; Li, G. D.; Guo, J.; Gu, L.; Hu, W. P.; Zhao, H. J.; Tang, Z. Y., *Nature* **2016,** *539* (7627), 76-80.

120. Hirai, K.; Furukawa, S.; Kondo, M.; Uehara, H.; Sakata, O.; Kitagawa, S., *Angew. Chem. Int. Ed.* **2011,** *50* (35), 8057-8061.

121. Gu, Y. F.; Wu, Y. N.; Li, L. C.; Chen, W.; Li, F. T.; Kitagawa, S., *Angew. Chem. Int. Ed.* **2017,** *56* (49), 15658-15662.

122. Yang, X. Y.; Yuan, S.; Zou, L. F.; Drake, H.; Zhang, Y. M.; Qin, J. S.; Alsalme, A.; Zhou, H. C., *Angew. Chem. Int. Ed.* **2018,** *57* (15), 3927-3932.

123. Corey, E. J., *Angew. Chem. Int. Ed.* **1991,** *30* (5), 455-465.

124. Evans, J. D.; Sumby, C. J.; Doonan, C. J., *Chem. Soc. Rev.* **2014,** *43* (16), 5933-5951.

125. Cohen, S. M., *Chem. Rev.* **2012,** *112* (2), 970-1000.

126. Morris, W.; Volosskiy, B.; Demir, S.; Gandara, F.; McGrier, P. L.; Furukawa, H.; Cascio, D.; Stoddart, J. F.; Yaghi, O. M., *Inorg. Chem.* **2012,** *51* (12), 6443-6445.

127. Huang, H. L.; Li, J. R.; Wang, K. K.; Han, T. T.; Tong, M. M.; Li, L. S.; Xie, Y. B.; Yang, Q. Y.; Liu, D. H.; Zhong, C. L., *Nat. Comm.* **2015,** *6*, 8847.

128. Martin-Martinez, F. J.; Jin, K.; Barreiro, D. L.; Buehler, M. J., *ACS Nano* **2018,** *12* (8), 7425-7433.

129. Fratzl, P.; Weinkamer, R., *Progress in Materials Science* **2007,** *52* (8), 1263-1334.

130. Fox, M. D.; Snyder, A. Z.; Vincent, J. L.; Corbetta, M.; Van Essen, D. C.; Raichle, M. E., *P. Natl. Acad. Sci. USA* **2005,** *102* (27), 9673-9678.

131. Huang, N.; Zhai, L. P.; Coupry, D. E.; Addicoat, M. A.; Okushita, K.; Nishimura, K.; Heine, T.; Jiang, D. L., *Nat. Comm.* **2016,** *7,* 12325.

132. Furukawa, H.; Muller, U.; Yaghi, O. M., *Angew. Chem. Int. Ed.* **2015,** *54* (11), 3417-3430.

133. Wang, Z. Q.; Cohen, S. M., *Chem. Soc. Rev.* **2009,** *38* (5), 1315-1329.

134. Zhou, W. C.; Begum, S.; Wang, Z. B.; Krolla, P.; Wagner, D.; Brase, S.; Woll, C.; Tsotsalas, M., *ACS Appl. Mater. Inter.* **2018,** *10* (2), 1528-1533.

135. Peng, Y. W.; Zhao, M. T.; Chen, B.; Zhang, Z. C.; Huang, Y.; Dai, F. N.; Lai, Z. C.; Cui, X. Y.; Tan, C. L.; Zhang, H., *Adv. Mater.* **2018,** *30* (3), 1705454.

136. Zhang, F. M.; Sheng, J. L.; Yang, Z. D.; Sun, X. J.; Tang, H. L.; Lu, M.; Dong, H.; Shen, F. C.; Liu, J.; Lan, Y. Q., *Angew. Chem. Int. Ed.* **2018,** *57* (37), 12106-12110.

137. Kitao, T.; Zhang, Y. Y.; Kitagawa, S.; Wang, B.; Uemura, T., *Chem. Soc. Rev.* **2017,** *46* (11), 3108-3133.

138. Pastore, V. J.; Cook, T. R.; Rzayev, J., *Chem. Mater.* **2018,** *30* (23), 8639-8649.

139. Zhang, Y. Y.; Feng, X.; Yuan, S.; Zhou, J. W.; Wang, B., *Inorg. Chem. Front.* **2016,** *3* (7), 896-909.

140. Fujiwara, Y.; Kadota, K.; Nagarkar, S. S.; Tobori, N.; Kitagawa, S.; Horike, S., *J. Am. Chem. Soc.* **2017,** *139* (39), 13876-13881.

141. Rodenas, T.; Luz, I.; Prieto, G.; Seoane, B.; Miro, H.; Corma, A.; Kapteijn, F.; Xamena, F. X. L. I.; Gascon, J., *Nat. Mater.* **2015,** *14* (1), 48-55.

142. Cohen, S. M., *J. Am. Chem. Soc.* **2017,** *139* (8), 2855-2863.

143. Zhang, Y. Y.; Feng, X.; Li, H. W.; Chen, Y. F.; Zhao, J. S.; Wang, S.; Wang, L.; Wang, B., *Angew. Chem. Int. Ed.* **2015,** *54* (14), 4259-4263.

144. Gamage, N. D. H.; McDonald, K. A.; Matzger, A. J., *Angew. Chem. Int. Ed.* **2016,** *55* (39), 12099-12103.

145. Nagata, S.; Kokado, K.; Sada, K., *Chem. Commun.* **2015,** *51* (41), 8614-8617.

146. Zhang, Z. J.; Nguyen, H. T. H.; Miller, S. A.; Cohen, S. M., *Angew. Chem. Int. Ed.* **2015,** *54* (21), 6152-6157.

147. Ishiwata, T.; Furukawa, Y.; Sugikawa, K.; Kokado, K.; Sada, K., *J. Am. Chem. Soc.* **2013,** *135* (14), 5427-5432.

148. Bae, Y. S.; Dubbeldam, D.; Nelson, A.; Walton, K. S.; Hupp, J. T.; Snurr, R. Q., *Chem. Mater.* **2009,** *21* (20), 4768-4777.

149. Ishiwata, T.; Michibata, A.; Kokado, K.; Ferlay, S.; Hosseini, M. W.; Sada, K., *Chem. Commun.* **2018,** *54* (12), 1437-1440.

150. Schmitt, S.; Diring, S.; Weidler, P. G.; Begum, S.; Heissler, S.; Kitagawa, S.; Woll, C.; Furukawa, S.; Tsotsalas, M., *Chem. Mater.* **2017,** *29* (14), 5982-5989.

151. Li, P. Z.; Wang, X. J.; Zhao, Y. L., *Coordin. Chem. Rev.* **2019,** *380*, 484-518.

APPENDIX

This dissertation included published papers shown below:

1. **<u>Feng, L.</u>**; Yuan, S.; Zhang, L.-L.; Tan, K.; Li, J.-L.; Kirchon, A.; Liu, L.-M., Zhang, P.; Han, Y.; Chabal, Y. J.; Zhou, H.-C., Creating Hierarchical Pores by Controlled Linker Thermolysis in Multivariate Metal-Organic Frameworks, ***J. Am. Chem. Soc.*** **2018**, *140* (6), 2363-2372.
2. **<u>Feng, L.</u>**; Yuan, S.; Li, J.-L.; Wang, K.-Y.; Gregory, D.; Zhang, P.; Wang, Y.; Zhou, H.-C., Uncovering Two Principles of Multivariate Hierarchical Metal-Organic Framework Synthesis via Retrosynthetic Design, ***ACS Cent. Sci*.** **2018**, 4, 12, 1719-1726 (***Front Cover***, Rank 6 of most downloaded articles in Dec. 2018).
3. **<u>Feng, L.</u>**; Yuan, S.; Qin, J.-S.; Wang, Y.; Kirchon, A.; Qiu, D.; Cheng, L.; Madrahimov, S.; Zhou, H.-C., Lattice Expansion and Contraction in Metal-Organic Frameworks by Sequential Linker Reinstallation, ***Matter***, **2019**, 1, 156-167.
4. **<u>Feng, L.</u>**[‡]; Wang, K.-Y.[‡]; Gregory, D.; Zhou, H.-C., The Chemistry of Multi-component and Hierarchical Framework Compounds, ***Chem. Soc. Rev.*** **2019,** 48, 4823-4853.
5. **<u>Feng, L.</u>**; Lv, X.-L; Yan, T.-H.; Zhou, H.-C., Modular Programming of Hierarchy and Diversity in Multivariate Polymer/Metal−Organic Framework Hybrid Composites, ***J. Am. Chem. Soc.*** 2019, *141* (26), 10342-10349.
6. **<u>Feng, L.</u>**; Wang, K.; Lv, X.-L; Powell, J.; Yan, T.; Willman, J.; Zhou, H.-C., Imprinted Apportionment of Functional Groups in Multivariate Metal-Organic Frameworks, ***J. Am. Chem. Soc.*** **2019,** 141, 37, 14524-14529.